**Master Thesis, Department of Geosciences**

# The Characterization of The Cementing Materials in The Ultramafic Tillites from Feragen and Leka, Norway

-aiming to find a good type of cement for Green Concrete

**Depan Hu**

**UNIVERSITY OF OSLO**

**FACULTY OF MATHEMATICS AND NATURAL SCIENCES**

# The Characterization of The Cementing Materials in The Ultramafic Tillites from Feragen and Leka, Norway

aiming to find a good type of cement for Green Concrete

**Depan Hu**


**Supervisors: Professor Håkon Olav Austrheim**

**Professor Dag Kristian Dysthe**

Master Thesis in Geosciences

Discipline: Environmental Geology and Geohazards

Department of Geosciences

Faculty of Mathematics and Natural Sciences

University of Oslo

01/09/2015

## Abstract:

Tillite rich in ultramafic material mixed with quartz and feldspar is present both at Leka and Feragen ultramafic complexes. The relative fast lithification (in ca 10000years) of this Mg rich system makes it interesting as a proxy for a new and more environmental (green) cement. Field work demonstrates that the studied tillite at Leka is ca 1 m thick, outcrop over an 10 × 10 m and is deposited on partly serpentinsed ultramafites. The tillite at Feragen is found in two settings: as meter thick bodies at the entrance to old chromite mines and as blocks up to 0.5 $m^3$ in a peaty area where the small creeks drain the mine tailings. The cement is classified as three main types, Leka Type A, Leka Type B and Feragen Type.Type A is containing MgO-$SiO_2$-$H_2O$ as the main oxide components , and Type B is in mainly in the system of MgO-$SiO_2$-$Al_2O_3$-$H_2O$. Feragen Type cement contains MgO, $SiO_2$ and $H_2O$ with minor content (up to 3%) of $Al_2O_3$. The average oxide ratio MgO : $SiO_2$ : $Al_2O_3$ : $H_2O$ in Type A is 1 : 1.63 : 0.00 : 5.02, and 1 : 0.43 : 0.14 : 1.94 in Type B, while it's 1 : 0.89 :0.01 : 1.11 for Feragen Type. In both cases the cement may consists of amorphous magnesium-silicate material with or without Al. This kind of cement in the tillites is different to the cementing material in most sedimentary rocks. Quartz and feldspar are strongly dissolved and provides the Si and Al to the cement respectively during its formation process in the tillites. The partly serpentinnized ultramafic clasts display weathering rinds where brucite is dissolved providing the Mg for the cement and leading to a high pH environment. This is consistent with the modeling results in PHREEQC for ultramafic weathering. Assuming an age for the tillite of 10000 years, the dissolution rate of quartz from Leka tillite is estimated to about $2.4 \times 10^{-19}$mol/s. This is lower than its theoretical dissolution rate (around $1.6 \times 10^{-15.3}$mol/s) in super-unsaturated solution with a pH of 10. This difference implies that the pore fluids in Leka tillite is probably saturated with respect quartz. In comparison experimentally determined dissolution rates of quartz determined at high pH (pH=13) ranges from $4.6 \times 10^{-13}$mol/s to $1.8 \times 10^{-12}$mol/s. Formation of cement like material in this unique composition represented by the tillite at such special environmental conditions is interesting, but more work is needed to bring the principles learned from this study into a new industrial cement product.

# chapter 1 *Introduction*

## 1.1Background about Portland cement

The cement industry has developed and grown for more than 175 years and it is used widely as construction material for building project in human society. Portland is the most commonly used cement and can be found widely in commercial cement production. It has various advantages, which are its durability, economic and convenience of getting raw materials, with annual production is about 3 Gt in the whole world (U.S. Geological Survey, 2009). However, the huge demand for Portland cement has lead to various issues, such as a vast energy cost and large green-house gas emission ($CO_2$ emission). Every year as the carbon dioxide issue becomes increasingly serious, which is resulting in more and more attention from governments, organizations of environment protection and some firms on this issue. Therefore, Portland cement is not an appropriate building material, which can meet new requirements for producing construction material in the future. Consequently, under this pressure, some researching institutes, universities and cement corporations have worked to establish many projects aiming to find out an alternative for Portland cement (Gartner, 2011). In addition, there are also some natural cementitious materials occurring on earth, which is usually the main factor for keeping some particular rocks together. By creating research that helps our understanding about the basic mechanisms in man-made cement hydration and hardening, we may be able to provide some good ideas or inspirations for this task.

### 1.1.1 General specification for Portland cement

Portland cement is the most widely used CaO-based cement. The raw material for Portland cement contains limestone, clay (shale),iron oxide and silica sand. The raw materials are placed into a kiln and with a temperature of about 1450 ℃ to form kiln clinker that have 4 different main phases: $3CaO \cdot SiO_2$ (main component for the Portland cement), $2CaO \cdot SiO_2$, $3CaO \cdot Al_2O_3$ and $4CaO \cdot Al_2O_3 \cdot Fe_2O_3$ (Kurtis, 2007). In addition, gypsum needs to be added, in order to get the resulted cement. And the setting time for the cement can be appropriately divided into several periods.

## A Initial and slow reaction periods

During the setting time, those compounds discussed in the last chapter react with solution to generate hydrates that contribute to the cement strength. Tricalcium silicate $3CaO \cdot SiO_2$ can hydrate in solution and will harden in a short time. In fact, immediately after wetting. The resulting product from the Tricalcium silicate is a calcium silicate hydrate phase, usually denoted as C-S-H ($CaO \cdot SiO \cdot H_2O$). The total hydration process of $3CaO \cdot SiO_2$ can be divided into 4 different periods: (1) initial reaction, (2) period of slow reaction, (3) acceleration period and (4) deceleration period based on the calorimetry data for hydration rate versus time (Schweitzer et al., 2007). During the hydration process of $3CaO \cdot SiO_2$, its dissolution rate varies with time. Firstly, $3CaO \cdot SiO_2$ dissolves quickly in the initial reaction period in a measured dissolution rate of at least 10 $umol \cdot m^{-2} \cdot s^{-1}$ in dilute suspensions (Garrault and Nonat, 2001). However, the dissolution rate drops rapidly after it enters the second period of slow reaction. The reason for the drop of dissolution rate of $3CaO \cdot SiO_2$ is still unconfirmed. There is one popular hypothesis proposed to explain it as good as possible, which suggests that a rapid formation of a calcium silicate hydrate phase as a thin and continuous metastable layer growing on the surface of $3CaO \cdot SiO_2$ grains. This passivates the activity of $3CaO \cdot SiO_2$ by isolating it from being contact with water, and becomes equilibrium with underlying $3CaO \cdot SiO_2$ at the same time. As a result, the dissolution state of $3CaO \cdot SiO_2$ are changed into the slow reaction period (Stein and Stevels, 1964; Jennings and Pratt, 1979). The trend of heat output representing the dissolution rate of $3CaO \cdot SiO_2$ versus time is displayed in the Fig 1.1 below:

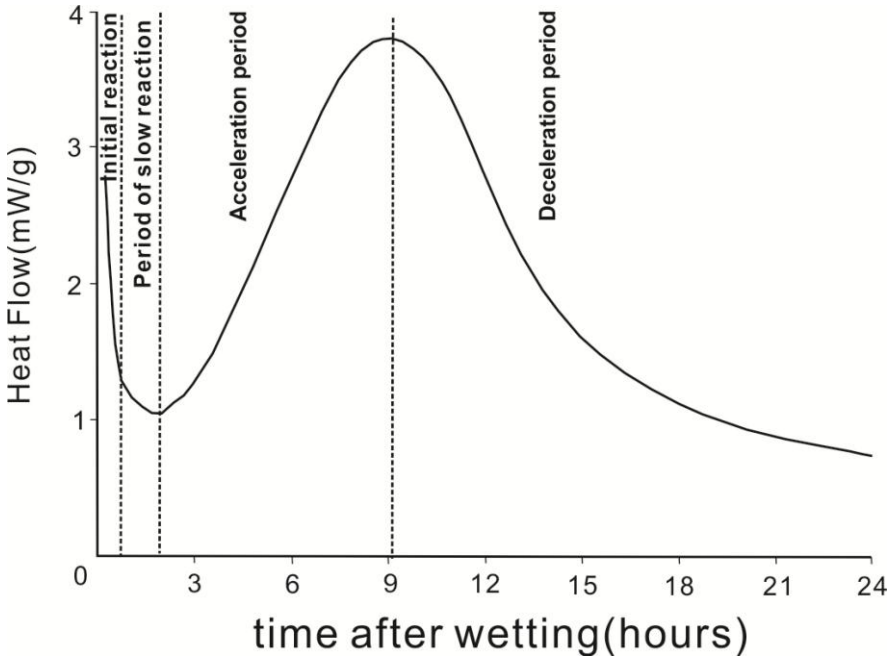


**Fig 1.1 The heat flow during the hydration of $3CaO \cdot SiO_2$ versus setting time, modified from Bullard et al., (2011)**

Whether or not such a thin and continuous metastable layer of calcium silicate hydrate (C-S-H) phase really appears on the surface of $3CaO \cdot SiO_2$ grains during the hydration process attracts some researchers' attentions. These researchers have utilised a variety of analyzing techniques to try to confirm the occurrence of such a barrier layer. However, only a few in-direct observations may imply that there is such a layer on the $3CaO \cdot SiO_2$ surface during slow reaction period. For instance, through examining pastes and dilute suspensions of $3CaO \cdot SiO_2$ nanoparticles in water with $^{29}Si$ NMR (Bellmann et al., 2010), there is an observation that an intermediate calcium silicate phase containing hydrated silicate monomer forms very early during hydration. The result from examining the pastes show that the hydration of $3CaO \cdot SiO_2$ develops in two stages: firstly, the formation of an intermediate silicate hydrate phase; secondly, this phase is converted into calcium silicate hydrate phase (C-S-H) if the aqueous concentration of calcium in solution is sufficiently. However, whether or not this intermediate calcium silicate phase is equal to that metastable barrier functionally is still unknown. This means that it needs more progress in this research field.

Besides the metastable barrier hypothesis, Barret and Ménétrier proposed another hypothesis, which is that a "superficially hydroxylated layer" forms on $3CaO \cdot SiO_2$ surface in contact with water (Barret and Ménétrier, 1980; Barret et al., 1983), and the

dissociation of ions from this layer is much more slowly than that directly from $3CaO \cdot SiO_2$ surface in highly undersaturated solutions. There have been a mechanistic explanation for the initial reactions in $3CaO \cdot SiO_2$ hydration, which is based on a steady state balance between slow dissolution of $3CaO \cdot SiO_2$ and the initially slow growth of calcium silicate hydrate (C-S-H) (Damidot et al., 1990; Garrault-Gauffinet and Nonat, 1999; Garrault and Nonat, 2001; Garrault, 2005; D.Damidot, 2007; Bellmann et al., 2010). Specifically, mineral dissolution rate depends on the saturation state of the solution (Lasaga and Luttge, 2001; Arvidson et al., 2003). If the solution is far from the equilibrium, then the driving force to open etch pits at surface defects of $3CaO \cdot SiO_2$ is large enough to enable a high dissolution rate. The dissolution rate will become slower when the solution is approaching equilibrium. In relation to the relevant phase the driving force becomes smaller, to keep such etch pits open at $3CaO \cdot SiO_2$ surface. Furthermore, SEM observations for $3CaO \cdot SiO_2$ specimens, which are not ground in different solutions with various dilution degrees, have confirmed the existence of the influence from solution saturation state on the relevant mineral dissolution rate(Damidot et al., 1990; Garrault-Gauffinet and Nonat, 1999; Garrault and Nonat, 2001; D.Damidot, 2007). Similarly, $3CaO \cdot SiO_2$ specimens in de-ionised water showed more apparent corrosion of their surfaces with some small etch pits in comparison to those showing results of smooth planar surfaces in saturated lime solution (Juilland et al., 2010). Maycock and Skalny (1974) or Odler and Schüppstuhl (1981) found that the quenched alite ($3CaO \cdot SiO_2$) has a shorter induction period than that without been quenched, as the quenching process probably can make more crystal defects (J.N.Maycock and J.P.Skalny, 1974; I.Odler, 1981).

**B. Acceleration period**

After the slow reaction period, the state of $3CaO \cdot SiO_2$ hydration enters the acceleration period and begins the nucleation and the growth of the calcium silicate hydrate phase, as the main characteristic for this period. During this period, experimental or modeling evidences have demonstrated that the rate of alite ($3CaO \cdot SiO_2$) hydration is related to the nucleation and growth of calcium silicate hydrate (C-S-H) on alite surface or other mineral's surface in solution (Barret and Ménétrier, 1980; Ings et al., 1983; Garrault and Nonat, 2001; J.F.Young, 2002; Garrault, 2005; Bishnoi and Scrivener, 2009; Thomas et al., 2009; Bullard and Flatt, 2010;

J.Thomas, 2013). Zajac reported that this hydration rate is proportional to the surface area of C-S-H as measured with nuclear magnetic resonance spectroscopy (ZAJAC, 2007). Thomas and Jennings (2009) conducted an experiment where $3CaO \cdot SiO_2$ pastes with additions of reactive calcium silicate hydrate (C-S-H) have no induction period and enter the acceleration period immediately, while those without such additions show an apparent induction period and a slower dissolution rate. The reason for the appearance of the acceleration period for $3CaO \cdot SiO_2$ hydration is also related to the nucleation and growth of calcium silicate hydrate(Wu and Young, 1984). However, the actual triggers for the onset of the nucleation and growth of calcium silicate hydrate are still a debate.

**C. Deceleration period**

There is an increasing number of hydration products appearing in the cement pastes. However, the total volume of such products is less than the sum volume of reacting water plus cement , so the total volume will decrease and results in some porous space filled by gas as the hydration process goes, which can decrease the hydration rate (Bullard et al., 2011).

## 1.2 Research on alternatives for Portland cement

### 1.2.1 Other man-made CaO-based cements

In addition to the Portland cement, there are some other kinds of cements used in construction industry occasionally, which are divided into 4 groups: calcium aluminate cements (CACs), calcium sulfoaluminate cements (CSA), alkali-activated binder and supersulfated cement.

Calcium aluminate cements was invented by Jules Bied of the J.& A. Pavin de Lafarge company in the early 1900s (Juenger et al., 2011). It primarily contains monocalcium aluminate (CA) sometimes with $12CaO \cdot 7Al_2O_3$ (C12A7) and/or $CaO \cdot Al_2O_3$ (CA2). This type of cement has several advantages compared with Portland cement: (1)Rapid strength gain upon setting; (2) Enhanced resistance to abrasion, sulfate attack and alkali-silica reaction; (3) lower CO2 emission during production (Scrivener and Capmas, 1998). Furthermore, it is often used in refractory and building chemistry applications (Scrivener and Capmas, 1998). However, the calcium aluminate cements have two main

problems limiting its application. The first problem is with the conversion process that leads to an increase in porosity and subsequently a decrease in strength from metastable hydrates to stable hydrate. In addition, the second problem is the relatively high cost of raw material because of bauxite is the main source for the calcium aluminate cement (Juenger et al., 2011). During the hydration process, there are two kinds of metastable hydrates-$CaO \cdot Al_2O_3 \cdot 10H_2O$ (CAH10) and $2CaO \cdot 3Al_2O_3 \cdot H_2O$ (C2AH8). These two metastable hydrates will be converted into a stable hydrate- $3CaO \cdot Al_2O_3 \cdot 6H_2O$ with $Al_2O_3 \cdot H_2O$ gel. The temperature can influence the composition of these hydrates during the hydration of calcium aluminate cement. When the temperature is less than 15 Celsius degree, $CaO \cdot Al_2O_3 \cdot 10H_2O$ is the main metastable hydrate phase (Scrivener, 2001). In addition, $2CaO \cdot 3Al_2O_3 \cdot H_2O$ becomes the main metastable hydrate phase when temperature approaches 30 Celsius degree (George, 1983; Bushnell-Watson and Sharp, 1990). Furthermore, if temperature is higher than 70 Celsius degree, the stable hydrate is predominant in the cement hydration.

Calcium Sulfoaluminate Cement (CSA) is another type of cement, which is not widely used in Europe or United States. However, it has been produced, used and standardized in China. The raw materials for manufacturing calcium sulfoaluminate cement are limestone, bauxite and calcium sulfate (gypsum or anhydrite) (Muzhen et al., 1992; Su et al., 1992; Ali et al., 1994; Wang and Su, 1994; Wang and Glasser, 1996; Su et al., 1997; Zhang et al., 1999; Zhang, 2000; Glasser and Zhang, 2001). The major constituent of calcium sulfoaluminate cement is ye'elimite ($4CaO \cdot 3Al_2O_3 \cdot SO_3$), whose content is from 30% to 70%. Calcium sulfoaluminate cement has two different clinkers: (1) sulfoaluminate belite clinker that mainly contains $4CaO \cdot 3Al_2O_3 \cdot SO_3$ and belite ($2CaO \cdot SiO_2$); (2) ferrialuminate clinker with $4CaO \cdot 3Al_2O_3 \cdot SO_3$, $4CaO \cdot Al_2O_3 \cdot Fe_2O_3$ and belite ($2CaO \cdot SiO_2$). The main hydraulic phases in calcium sulfoaluminate cement are belite, calcium aluminoferrite, anhydrite or free lime, calcium aluminates, perovskite or gehlenite (Muzhen et al., 1992; Su et al., 1992; Sahu and Majling, 1993), while the main cementitious phase in CSA is ettringite. Calcium sulfoaluminate cement has advantages of low $CO_2$ emission(Gartner, 2004), low firing temperature(Juenger et al., 2011). This is typically 1250 ℃<1450 ℃ for Portland cement, more grindable clinker, high resistance to freeze-thaw and chemical attacks by seawater, sulfates, chlorides, magnesium and ammonium salts (Muzhen et al., 1992; Su et al., 1997; Zhang et al., 1999;

Zhang, 2000; Glasser and Zhang, 2001) and better protection for the steel reinforcement from corrosion (Juenger et al., 2011). However, high cost of raw material is still a main problem, which limits the manufacturing and use for calcium sulfoaluminate cement. Furthermore, faster reacting and more rapid carbonation of ettringite leading to strength loss are also limiting factors for calcium sulfoaluminate cement.

Alkali-activated binder is a kind of cementitious material produced from entirely waster-stream materials (fly ash and blast furnace slag) with alkaline activating solution (Juenger et al., 2011). It also has a lower environment impact (Duxson et al., 2007), comparable durability and strength to Portland cement. It's for this reason, alkali-activated binder is increasingly attracting attention as a potential alternative for Portland cement (Juenger et al., 2011). The reaction kinetics of alkali-activated binder is shown in the Fig 1.2.

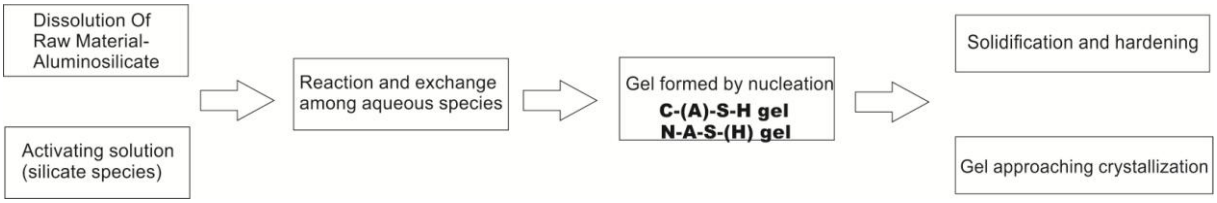


**Fig 1.2 Alkali activated binder formation mechanism. (Juenger et al., 2011)**

Supersulfated cement comprises of 70-90% ground granulated blast furnace slag, 10-20% calcium sulfate and around 5% alkaline activator, which is usually used in Portland cement (Bijen and Niël, 1981; Taha et al., 1981; Mehrotra et al., 1982; Dutta and Borthakur, 1990; Erdem and Ölmez, 1993; Singh and Garg, 2002; Bellmann et al., 2005; Mun et al., 2007; Gruskovnjak et al., 2008). The slag has high contents of CaO, MgO and $Al_2O_3$. Calcium sulfate is the addition for the slags with high $Al_2O_3$ content (Dutta and Borthakur, 1990). Generally, the hydration mechanism of the supersulfated cement is that the alkaline environment of the pore solution is favorable to dissolution of the slag. Those dissolving aluminum, calcium and silicon ions then react with the addition of calcium sulfate to produce ettringite and calcium silicate hydration phase (C-S-H phase), which make contribution to the strength development during hydration process of the cement (Juenger et al., 2011).

**Table 1.1** General comparisons between Portland cement, calcium aluminate cements calcium sulfoaluminate cements, alkali-activated binder and supersulfated cement (Juenger et al., 2011)

| | **Portland cement** | **Calcium aluminate cement** | **Calcium sulfoaluminate cement** | **Alkali-activated binder** | **Supersulfated cement** |
|---|---|---|---|---|---|
| **Main phase** | (C3S) | (CA) | ($C_4A_3\bar{S}$) | Activator NS | Slag, $C\bar{S}$/$C\bar{S}2H$ |
| **Emission CO2/Primary Phase in manufacturing (g/g)** | 0.578 | 0.279 | 0.216 | 0.361 | 0 |
| **Clinkering temperature (℃)** | ~1450 | >1450 | 1250 | 800(metakaolin) | N/A |
| **Grinding energy (kWh/t)** | 30 | >30 | ~20 | 50 for slag | 50 for slag |
| **Advantages** | Long history of being used; Standard composition | Rapid strength; Sulfate resistant; No alkali-silica reaction; Abrasion resistant | Low CO2 emission Low energy Rapid strength Shrinkage compensating | Low heat of reaction; Heat and acid resistant | Low heat of hydration; Durable in aggressive environments; |
| **Disadvantages** | High energy cost and CO2 emission; Limited early strength; Poor in aggressive environments | Strength loss on conversion of metastable to stable hydrates | Durability unproven; Sometimes expansive | Sometimes slow strength gain; Caustic activating solution; Challenging rheology; Durability unproven | Slow strength gain |

## 1.2.2 Man-made MgO-based cements

In addition to the CaO-based cements, there are also cements using MgO as the main fundamental materials, such as Sorel Cement and magnesium phosphate cement, both of which have been produced and used in construction industry. Furthermore, periclase (MgO) is the main constituent for this kind of cement, and the needed MgO is from calcination of magnesite $MgCO_3$. The calcination temperature must be high enough to induce periclase crystal to grow larger to reduce its reactivity. Because of periclase with relatively low reactivity is favorable to enable cement to have a long working time.

However, currently MgO-based cements have not yet been widely used, there are several weaknesses occurring about current industrialized MgO-based cements. Firstly, the relatively high cost of pure periclase and lack of some raw materials, such as phosphate ores, which is a preferred product used in the agriculture; Secondly calcination of magnesite is not energy efficiency and the $CO_2$ emission per unit mass from the calcinations is higher than burning limestone for Portland cement (Gartner and MacPhee, 2011).

Researchers are still trying to develop an environment-friendly type of MgO-based cement with advantages of cheap raw material, low $CO_2$ emission and energy efficiency in production. Significant progress has been made by Vlasopoulos and Cheeseman from Imperial College, London(Gartner and MacPhee, 2011). They developed a new type of magnesium oxide based cement that is named as Novacem, whose raw material source might be magnesium silicate rocks, such as peridotite, which is abundant in the earth crust and does not contain fossil $CO_2$ as limestone and magnesite. The other significant characteristic of Novacem, is that it makes use of recycled $CO_2$ during the manufacturing process of cement possible theoretically. However, this has only been explored from a theoretical position, and is yet to be applied practically (Gartner and Macphee, 2011). The detail about the production process of Novacem is shown in Fig 1.3.

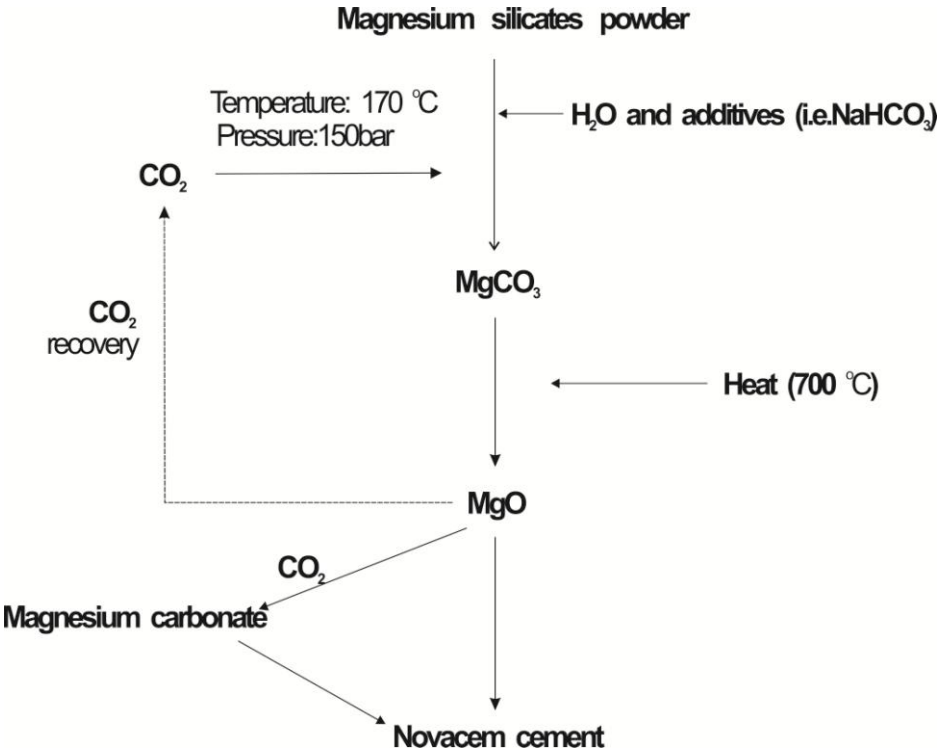


**Fig 1.3 Novacem production (modified from Gartner and Macphee, 2011)**

### 1.2.3 The Leka tillite, Feragen tillite

In the Leka and Feragen areas, one kind of consolidated agglomerate is found. Within the Leka agglomerate and the Feragen one, the serpentinized ultramafite fragments are commonly occuring. Furthermore, the two agglomerates are located on bedrocks of ultramafite and the surrounding rock bodies are also belonged to ultramafic. Thus, the Leka Ophiolite Complex and the Feragen Ultramafic Body make contribution to them respectively. However, local ultramafic rock is not only the material source, and there are some observations can explain this point. For instance, both of the two agglomerates have apparent contents for quartz mineral, which usually can not be found in ultramafic rock or mafic rock bodies. Furthermore, there is no component that obviously contains quartz within the Feragen Ultramafic Body and the Leka Ophiolite Complex. Consequently, the quartz grains in the two agglomerates are probably from outside the Feragen area and the Leka Island, respectively. Prestvik and Bøe (1974) provided two possibilities for the forming reason of the agglomerate on Leka island. They are glacial origin and mass waster, such as debris flow, after observed the Leka serpentinite conglomerate site (they named it as serpentinite conglomerate in that time). However, local debris flow rarely can have such a huge power to move materials from tens kilometers away or even outside the island to current places on the local topography conditions of the Feragen area and the Leka island. Moreover, glacial origin is indeed a reasonable explanation for the formations of the two agglomerates. In addition, tillite is a type of consolidated agglomerate made by glaciation. That's why they are named as Leka tillite and Feragen tillite respectively in the thesis.

There is no remant of local tectonic movement happening in the Tertiary found in the Leka tillite layer (Prestvik and Bøe, 1974). Therefore, it implies that the formation time of the Leka tillite is after the Tertiary period, and probably in the würm glaciations. Additionally, the Feragen tillite has the resemble lithological characteristic as the one in Leka, and they are consolidated in the similar extent. It implies that the Feragen tillilte was also formed in the same glaciation.

The cement occuring in the two tillites are classified as magnesium silicate or magnesium aluminosilicate.

### 1.2.4 Natural cements in sedimentary rock

In clastic rocks, grains usually are tightly bound together by some cementing minerals occurring in the void spaces, which are from the precipitation of related ions in pore fluids when the condition is satisfied. Generally in the sedimentary rock, the cementing minerals are classified as silica cement, carbonate cement and some others, such as clay minerals. The silica cement group mainly contains opal, chalcedony and quartz, while the calcite, dolomite and siderite are belonged to the carbonate cement group. In sandstone sedimentary rock the most common type cement is mainly silica.

However, magenesium silicate or magnesium aluminosilicate have not been found widely as cement within the sedimentary rocks. Furthermore, those common cements in the sedimentary rocks are usually formed under high pressure and temperature condition as the buried depth of its host rock is about hundreds- to thounsands of meters. Consequently, the magnesium silicate or aluminosilicate cement in the tillite was formed under a different environment that is on the earth surface with much lower pressure and colder temperature. That is the main motivation for the study on the cement in the two tillites.

# Chapter 2 *Geology Background*

## 2.1 The coordinates for the field sites

In order to better understand the influence of the weathering of minerals in ultramafic rock on naturally formed concrete, it's necessary to collect some raw samples from field works. Therefore, there were two field works for tillite within August 2014 and September 2014. The first field work data set was taken from Leka Island, which is located of the Norwegian west coast. The second field work data set, is taken from the Feragen, which is near the border between Norway and Sweden in Sør-Trøndelag in the central Norway. The proper coordination range for Leka Island is ~65°02′ N to 65°08′ N and 11°29′E to 11°49′E, while the Fegagen lake is in the area 62°33′N to 62°28′N and 11°51′E to 11°55′E, respectively.

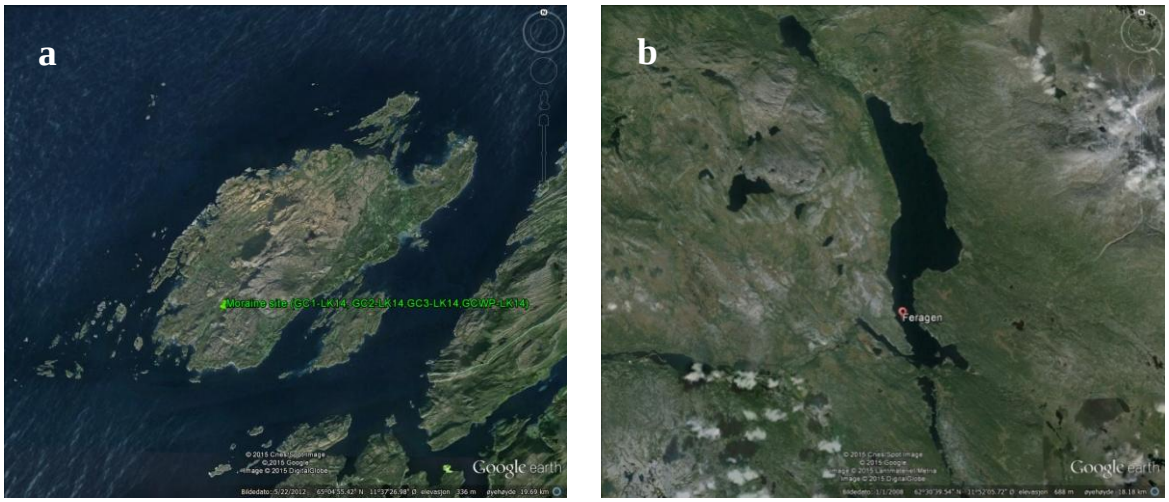


**Fig 2.1. The Satellite images for the two sites, (a)The Leka Island with tillite site marked by green tip; (b) The Feragen Area**

## 2.2 The Leka Ophiolite Complex (LOC) on Leka Island

The Leka ophiolite complex is a most complete case of ophiolite presenting within the upper Allochthon of the Scandinavian Caledonides (Furnes et al., 1988). Using the U-Pb zircon dating method, the age of the Leka ophiolite complex is estimated as 497 +/- 2Ma(Dunning and Pedersen, 1988). The Leka ophiolite complex is classfied as the Table Mountain type based on Nicolas's classification for ophiolite(Nicolas and Violette, 1982). The term ''LOC'' is the abbreviation for Leka Ophiolite Complex, which contains all the components in the magmatic development of the Leka ophiolite. Furnes et al.(1988) indicated that there are totally 7 different litho-components in the LOC: the ultramafic

rocks of mantle affinity (Harzburgite), the layered ultramafics, the layered metagabbro, the vari-textured metagabbro, the volcanic&volcaniclastic rocks and the basalt dykes.

The ultramafic rocks relating to the depleted upper mantle is a complex of harzburgite with minor dunite. The thickness of the harzburgite complex ranges from about 500~600 meters on its west side to 1500 meter on the east side. In addition, it's in transitional contact with ultramafic cumulates-layered dunites on the west side, while in tectonic contact with the metagabbro of LOC on the east side(Furnes et al., 1988). The layered ultramafic cumulates are within the Skråa block and the Steinstind block with thickness varying from a hundred to several hundred meters. Within the layered ultramafic, a few macro-rhythmic units occurs in the scale of 10 to 50 meter of thickness. Additionally, wehrlitic and pyroxenitic veins segregates the macro-rhythmic units. The outcrop of the layered metagabbro of the LOC can be observed in the area southwest to the Steinstind block. The layered metagabbro is transited into laminated and vary-textured metagabbro from the southeastern part to the northeastern part of the Leka Island, and the vary-textured metagabbro occur on the islets of Madsøya where the metabasalt dykes occur as well. Minor acid intrusions of quartz-keratophyre and plagiogranite exist within the vari-textured metagabbro and the dykes.

The Leka Island covers about 90 $km^2$ areas and on the edge of the Trøndelag platform. It has a basement of gneisses (Titus et al., 2002). Within the LOC, the ultramafic and mafic units are folded into two open synclines. In addition, there are two sets of faults dividing the Leka Island into discrete blocks. The larger faults have a NE-SW orientation and a NW-SE orientation for the smaller set.

The rodingite is found within the layered sequence of the ophiolite complex in Leka, which is an evidence for the hydration of the ultramafites. And those fractures and deformation zones cutting the lithilogical boundaries at high angles within the Leka ophiolite complex usually play as conduits for transport of element and fluids for the rodingization process. Mostly the serpentinization and chloritization of the untramafites are the Ca-source for the Rodingization. However rodingitized ultramafic rocks can also be found with formation of grossular and vesuvianite at some places(Austrheim and Prestvik, 2008).

## 2.3 The Feragen Ultramafic rock body

The Feragen ultramafic rock body is in the Røros area in the southeastern of the Sør-Trøndelag region, Norway. It covers around 15 $km^2$ area and is one of a set of ultramafic bodies in the southern part of the Trondheim basin, which has been identified as an alpine peridotite existing within Cambro-Silurian sequences (Moore and Hultin, 1980). The Feragen ultramafic rock mainly consists of serpentinized dunite and peridotite with layers of harzburgite and chromite layers(Beinlich and Austrheim, 2012). Its northern and north-eastern contacts with surrounding rocks are partly covered by the Devonian serpentinite conglomerate (Goldschmidt, 1913). Moreover, it is in contact with Røros schists in the southwest and in contact with augen-gneiss in the southeast (Moore and Hultin, 1980). Serpentinization is commonly seen in the components of dunite and peridotite within the Feragen ultramafic body where olivine, pyroxene and chromite are primary minerals. Magnesium carbonate can be found along the surfaces of fractures somewhere in the rock body. In the 19$^{th}$ century, the Feragen ultramafic rock body was the main site for chrome mining in Norway and then stopped at 1927(Beinlich and Austrheim, 2012). Consequently, there are some remants from the past mining activity left in the Feragen area, such as some mining pits and about 20 shafts with lengths ranging from tens to hundreds of meter. Furthermore, in some recent field works in the Feragen, it is shown that the surface of the shaft wall is often coated with white magnesium carbonate minerals, for instance magnesite(Beinlich and Austrheim, 2012).

It is indicated that there are two separate phases of faulting and joint development within the Feragen ultramafic rock body, which has resulted in two sets of faults and joint surfaces with mutually perpendicular directions(Hultin, 1965). Moreover, the earlier sets of surfaces have strikes of 320°~360° and dip 50° E to 60°W, while the later ones are vertical with east-west strike. The bedrock maps for the Leka Island and the Feragen area are displayed in the Fig 2.2.

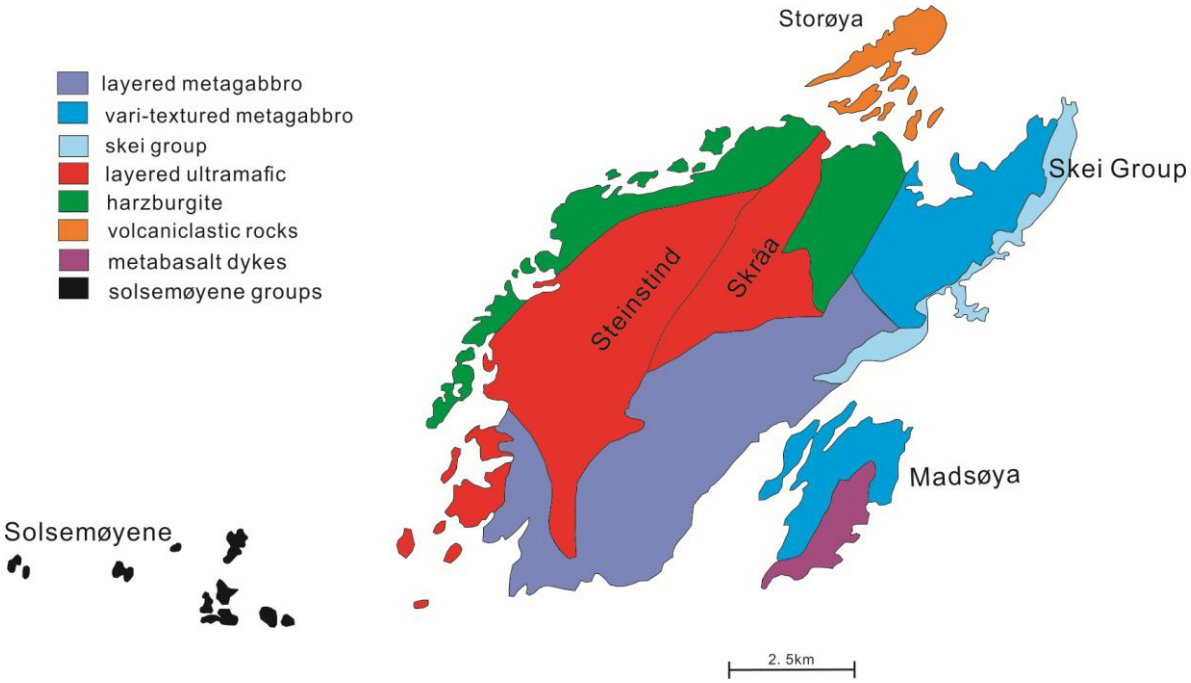


(a)

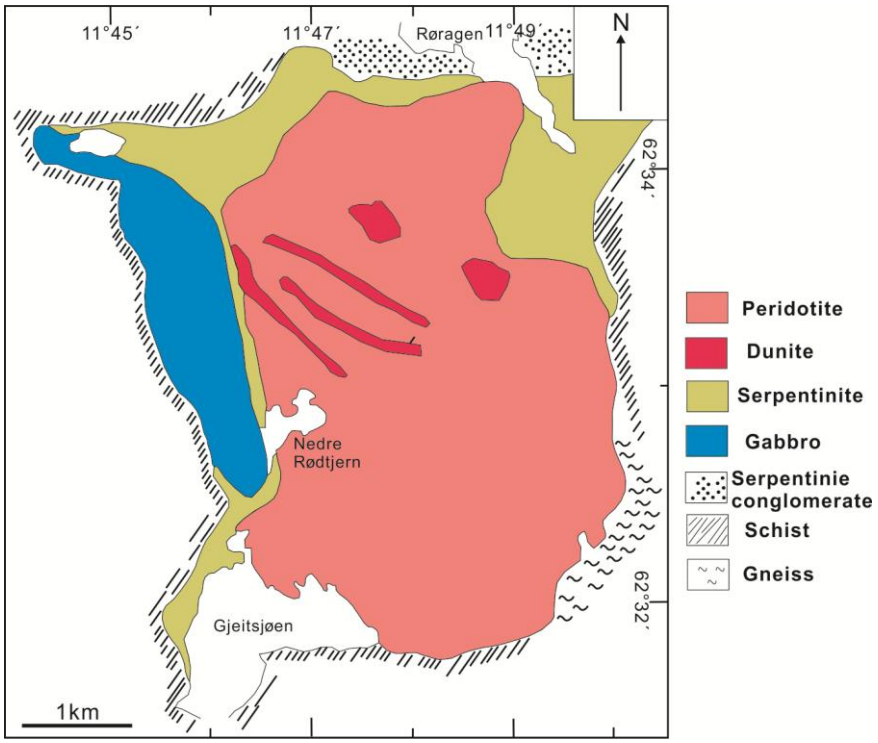


(b)

**Fig 2.2 The general geological maps about the two investigated regions. (a) Leka Ophiolite Complex ;(b) Feragen Ultramafic Complex;**

# Chapter 3 *Methods and Experiments*

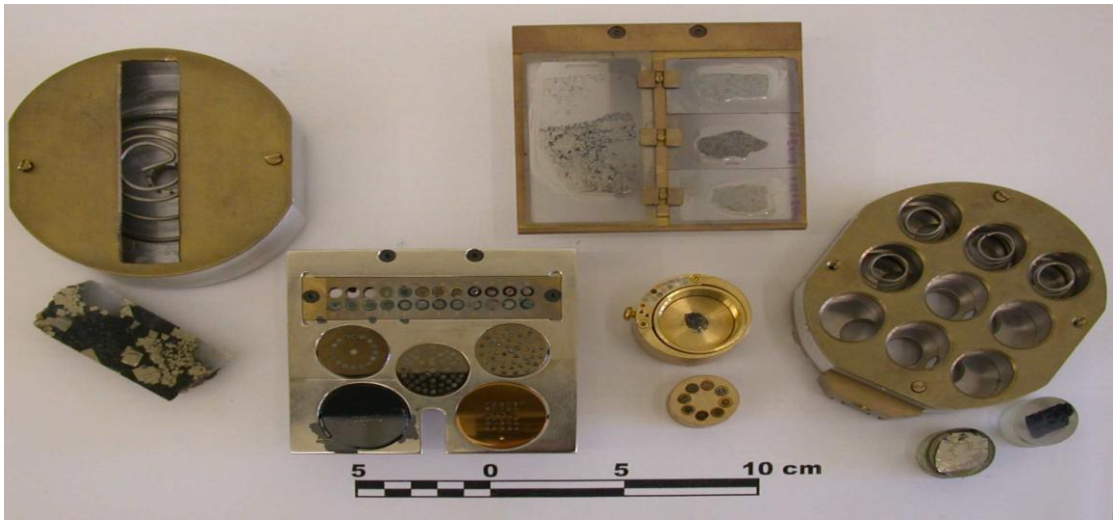

## 3.1 Field work

Direct observation in field work for geological objectives or phenomenon is the first step in the project. About the concrete site at the Leka Island, the author of the thesis spent several days searching for the outcrop, observed lithological features and stratification features, collected some samples of concrete pieces as well for coming lab analysis works with one of his supervisors in August 2014.In addition, there was a group of students from geosciences and physics departments from the University of Oslo, who had investigated the concrete sites in Feragen area in September 2013, whose data and results can be used in the thesis with the permission from them(Li et al., 2013), while the author also took another 3 days to see the geological situations about the tillite in Feragen area in September 2014 with his two departmental supervisors.

## 3.2 Polarized-light microscope

The polarized-light microscope has been used in geology as a method to observe optical characteristics of minerals and then determine their textures and phases in thin section from rock sample with utilizing transmitted light or reflected light. Using this microscope, is that is cheap, easy to operate, and can be used to observe mineral's texture in a high spatial resolution.

The basic components of a microscope are ocular lens, Bertrand lens, upper polarizer, objective lenses, specimen stage, sub-stage assembly that concludes lower polarizer, aperture diaphragm, condenser lenses and auxiliary condensing lens and an illuminator with some accessories and supporting parts(Nesse, 2003). An overview image of the polarized-light microscope is shown in the Fig 3.1.

However, as this type microscope can't quantitatively determine the chemical, elemental composition of a rock complex, distinguish very tiny mineral crystal. So it is often used with some other complementary and advanced instruments, such as scanning electron microscope and electron microprobe, to finish a special task in geological or material research.

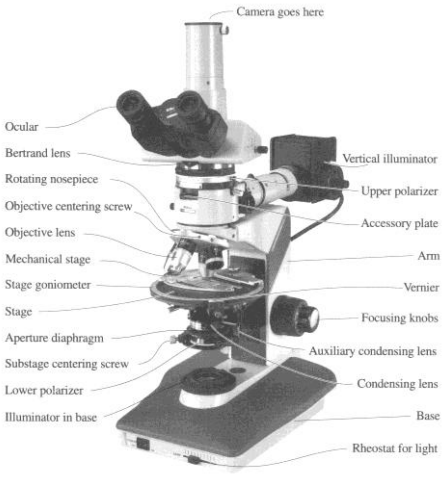


**Fig 3.1. Polarized-light microscope with components marked with their names (Nesse, 2003)**

# 3.3 Electron microprobe (EMP) and Scanning electron microscopy (SEM)

## 3.3.1 Fundamental principles

When the incident beam of electron from electron gun hits the specimen, there will be several different types of interaction between the beam and the specimen. From the surface to the inner part, the interaction type varies from auger effect, secondary electron emission, backscattered electron emission, characteristic x-rays, continuum x-rays and fluorescent. The deepest arrived place by the incident beam is about 10 micrometer below the specimen surface. Auger electron emission, secondary electron emission, characteristic x-rays, continuum x-rays and fluorescent x-rays are collectively as a group of inelastic scattering of electrons, while only the backscattered electrons belong to elastic scattering (Reed, 2005).

Secondary electrons are those initially residing in the specimen with a few nanometers depths below the surface and are ejected out by the primary electrons in the incident beam. Secondary electron's energy is very low, which is the main difference between secondary electron and backscattered electron. Backscattered electrons are from the incident beam and deflected out from the specimen surface by nuclei in the specimen through angles greater than 90°(Reed, 2005).

In addition to the electron radiations, there is another type radiation that is the x-ray production from the specimen hit by the incident electron beam, which is focused significantly in both of microprobe and scanning electron microscopy. Within the x-ray radiation, the continuum x-rays are generated by slowing the incident beam with coulombic electrical field of atoms close to the surface. This generates the backgrounds in x-ray spectrums, while the characteristic x-rays are resulted from electron transitions from higher energy levels to lower energy ones inside ionized atoms in specimen. One characteristic x-ray has its own specific energy or wavelength, and this is the fundamental theory for detecting different elements in specimen.

### 3.3.2 Introduction to scanning electron microscopy (SEM) and electron microprobe (EMP)

From the electron source to the target, the basic combinations of those functional components are almost the same in both SEM and EMP. The section from the electron source to the target is called electron column. The electron column comprises of electron gun, condenser lens, objective lens, scanning coils and specimen holder. In addition to these mentioned above, the secondary electron detector, backscattered electron detector and energy dispersive spectrometer system are equipped within both SEM and EMP. However, the most apparent difference between EMP and SEM is that there are usually 5 wavelength dispersive spectrometer systems are installed around the electron column in EMP, which are not seen in SEM. There is one WDS system displayed in the Fig 3.2 (b).

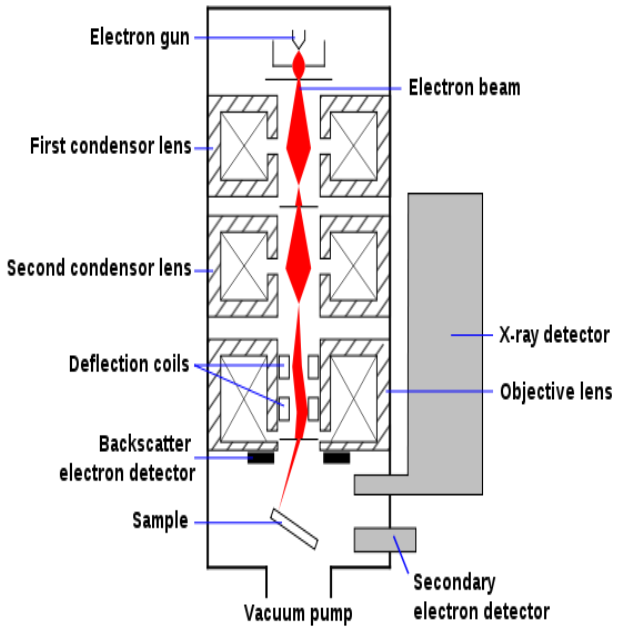


(a) SEM diagram("Schema MEB-wikimedia")

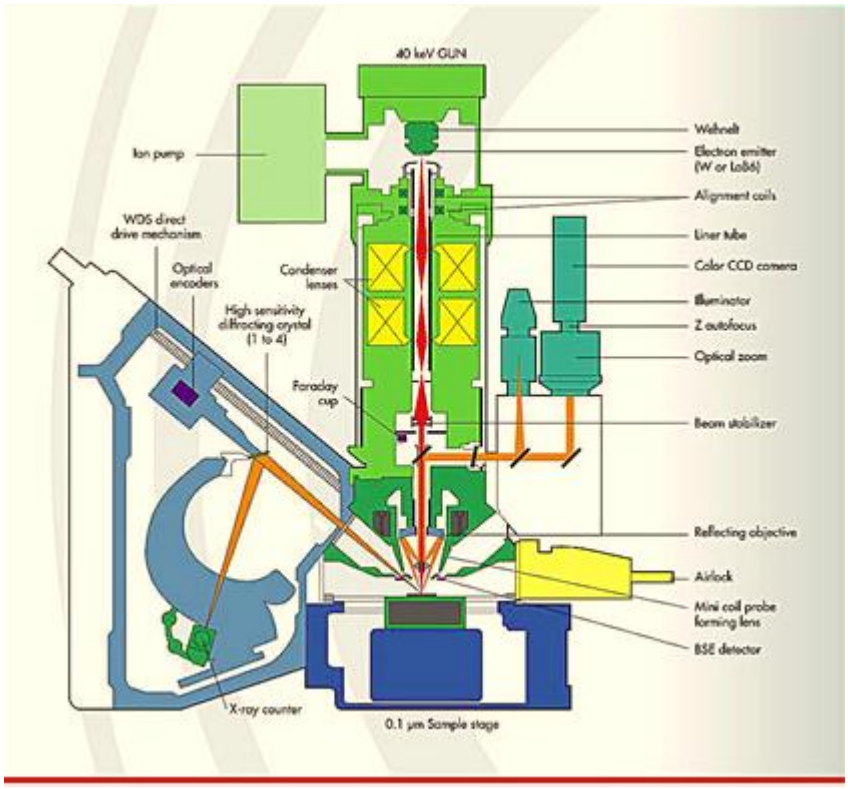


(b) A schematic diagram for EMP with wavelength dispersion spectrometer system(CAMECA SX100)

**Fig 3.2 Schematic diagrams for SEM and EMP**

### 3.3.3 Energy Dispersive Spectrometer (EDS) system assembly and Wavelength Dispersive Spectrometer (WDS) system assembly

WDS, the wavelength dispersive detection system in which x-rays from different elements are recognized and separated from one another by their wavelength using Bragg diffraction("CAMCOR at University of Oregon," 1995).

EDS, energy dispersive detection system in which x-rays from different elements are recognized and separated from one another by their characteristic energy using a solid state detector and multichannel analyzer("CAMCOR at University of Oregon," 1995).

### 3.3.4 Advantages and disadvantages of SEM and EMP

Firstly, specimen preparation is easy for SEM or EMP analysis. Secondly, analysis in SEM or EMP will not destroy or damage specimen, and the detection limits are low enough for minor and even trace element contents. In addition, their accuracy is very high, which is about $\pm 1\%$ for major element quantitative analysis, while they can finish in-situ check that usually can't be done by other instruments. SEM can provide an excellent spatial resolution for morphology study.

The electron microprobe is yet not able to detect the $H_2O$ and $CO_2$ molecules in minerals when it does WDS analysis, which should be corrected while calculating the structural formula for mineral.

## 3.4 Mineral Phase Detection Instrument - X-ray diffractometer

The X-Ray Diffractometer (XRD) is a widely used technique in mineral or crystal structure analysis. Its basic principle is also the Bragg's law and its configuration is similar to WDS system. Its function is finding out mineral phases existing in specimen by determining characteristic lattice spaces of different minerals instead of quantitatively analyzing composition of specimen. There is an x-ray tube instead of the electron gun in XRD. The general working mechanism is that the incident x-ray generated by the tube is

toward the specimen and then reflected to the detector at a certain angle when they are consistent with the requirements of Bragg's law. The angle value is measured and can be related to the lattice spacing value of specimen.

The special requirement for XRD specimen is that the sample should be grounded into powders in sizes less than 500 um.

## 3.5 Softwares

### 3.5.1 Geochemical Simulation software-PHREEQC 3

Geochemical modeling software PHREEQC 3 is a programme written in C or C++ language, which can fulfill various calculations for changes happening in different geochemical environments. Additionally, this has several databases fitting to different application fields. There are a variety of keywords employed with specified functions to be combined regularly in the input file to correctly simulate speciation of aqueous species in solution, batch-reaction, and sorption or desorption phenomenon, kinetically controlled reactions and so on. Furthermore, PHREEQC also provides charting and graphing functions to help user analyse data more efficiently and demonstrate some changing trends intuitively (Parkhurst and Appelo, 2013).

### 3.5.2 Image processing tool-matlab

Matlab is a powerful software used in data analysis, modeling and image processing. It provides various functions to convert grey scale image to binary image, segment binary image and calculate area of interested part in binary image.

## 3.6 Experiment

### 3.6.1 Experiment preparation

Quartz dissolution phenomenon is found in both of the Leka and Feragen tillites, which is probably related to the formation of cementitious material in them. In order to look further into the quartz dissolution rate that may be helpful for determining the origin time of these tillite. It is for this reason an experiment will be carried out to examine these queries.

Firstly, consolidate a small quartz piece, which is from a larger quartz crystal from the geology museum of University of Oslo, into a epoxy in cylindrical shape with diameter of 2.5 cm. The second stage will be to polish the cylinder upper surface where the quartz piece is to flat and make the surface of quartz piece almost on the same horizontal plane with the surrounding surface of epoxy. After pre-processing the sample, it will be placed in a basic 300ml solution, which is saturated with $Mg(OH)_2$.The pH is increased from around 10 to about 13 by adding some sodium hydroxide pellets. The solution will be stored in polypropene beaker with a fit cover to isolate the solution from atmospheric $CO_2$. Before this process has taken place, the topography about one selected tiny area between the quartz surface and the surrounding epoxy surface is measured and recorded by the Wyko NT 1100 optical profiler as initial reference This will then be compared with the final topography data obtained after the experiment in 1 month. Because the average temperatures in summer and winter are different. Consequently, two groups of the basic solution with cylindrical specimen are prepared and then separated in different environment, one, named as **SP4**, is in the fridge (5 ℃), while the other one **SP9** is under room temperature (20 ℃).

The NT 1100 optical profiler is a cost-effective, non-contact, and comprehensive method to measure topography of specimen's surface in 3 dimensions. The working principle for the profiler is that interference pattern resulted by recombination of two rays split from the incident light reflected by a mirror in the profiler and specimen surface respectively(Imbert et al., 2012). In addition, several objectives and 5 FOV (Field of View) multipliers occur for selecting according to actual demand for magnification. Vertical measurement range of the NT 1100 profiler is from 0.1 nm to 10 mm std. The specimen stage of the profiler is automated and can be tilt at +/-6°. Furthermore, there is a software 'Vision' to analyze interferogram captured by the profiler.

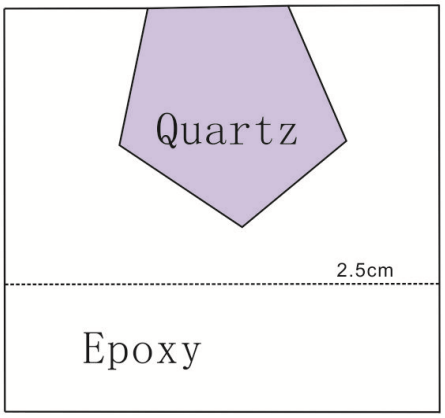


**(a)**

**(b)**

**Fig. 3.3 (a) Schematic diagram for cross section of the specimen in the experiment ; (b) Wyko NT 9100 optical profiler**(“Wyko NT9100 Optical Pro ling System”)

## 3.6.2 Mathmatics in quartz dissolution experiment

For most minerals, their dissolution rate in solution can be estimated by the equation from Palandri and Kharaka (2004) from U.S.Geological Survey. The detailed expression about such equation is demonstrated below,

$$\frac{dm}{dt} = \sum[S \cdot K^{298} \cdot e^{\frac{-E}{R}\left(\frac{1}{T}-\frac{1}{298}\right)} \cdot a_{H+}^{n} \cdot (1-\Omega^{p})^{q}]. \qquad (\textbf{eq-1})$$

Here the **eq-1** is obtained by recasting the original expression in terms of rate constant at 298 K with Arrhenius equation. The original experession of rate refers to Palandri et al., 2004. Rate dm/dt, mole/s; S represents the surface area of mineral in reaction, $m^2$; $K^{298}$ represents the rate constant for mineral in a ceratin condition at temperature of 298K, its value is $10^{-13.99}$mol/$m^2$/s for basic condition at temperature of 298 K (Palandri and Kharaka, 2004); $a_{H^+}$ is the activity of $H^+$ in solution, n is the reaction order about activity of $H^+$. The exponent n will change according to different reaction condition, which is positive for acid and negative for base; T is the temperature of reaction, in Kelvin; R is the gas constant, whose value is 8.314 J/K/mole; E is the activation energy of mineral, J/mol; Ω is saturation index of mineral in solution and equals the ratio $Q/K_e$ where Q is activity product and $K_e$ is the equilibrium constant of mineral. In addition, p and q are empirical parameters. In the full expression about dissolution rate, there is a sum symbol of "∑". This is due to that the dissolution rate is the sum of the three rates from acid mechanism, neutral mechanism and base mechanism (Palandri and Kharaka, 2004).

In addition, Palandri et al, (2004) found that the expression for each mechanism can fit well enough with experiment data of mineral dissolution rate in the same mechanism. Thus, it is appropriate to utilise the basic term to estimate quartz dissolution in the experiment. The mathematical expression about dissolution rate is simplified and normalised to 1 $m^2$, displayed as below:

$$\frac{dm}{dt} = K_{base}^{298}\, e^{\frac{-E_{base}}{R}\left(\frac{1}{T}-\frac{1}{298}\right)} a_{H^+}^{n_{base}} \cdot (1-\Omega^{p_{base}})^{q_{base}} \qquad (\textbf{eq-2})$$

# Chapter 4 *Results-Petrography and mineral chemistry*

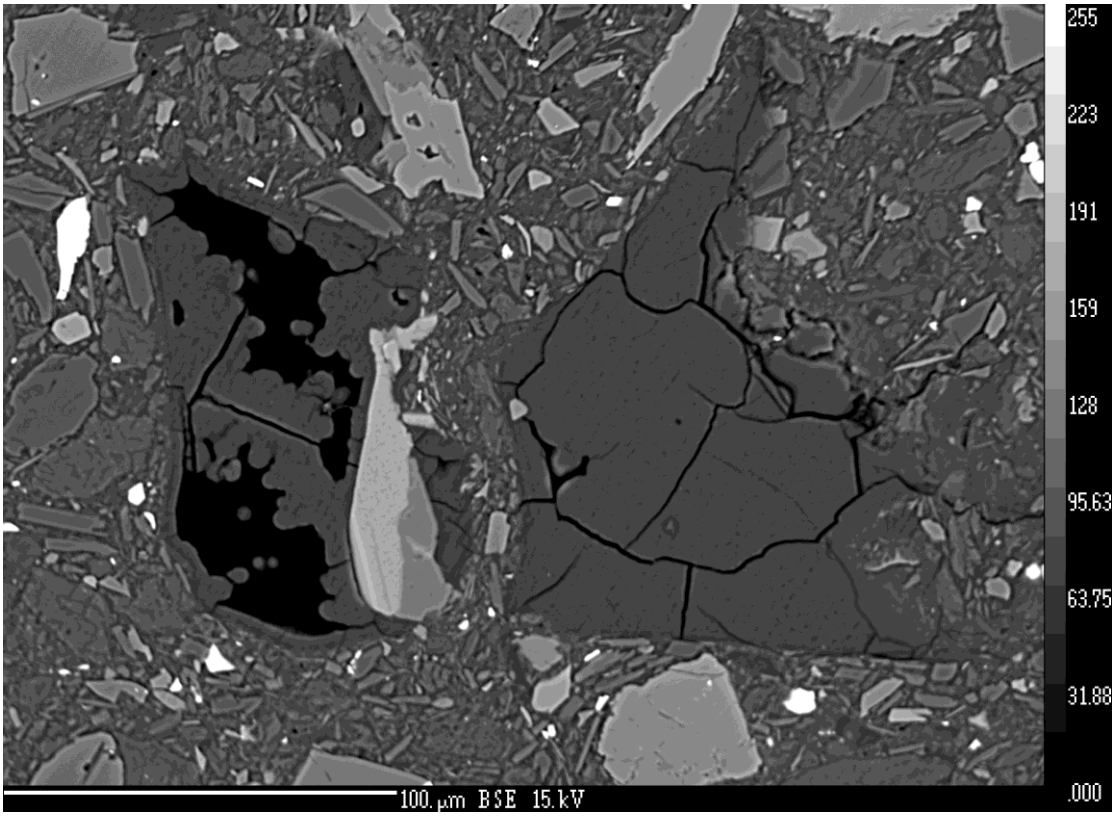


*-a hole filled up with cement near another hole partly filled by cement in Leka tillite*

## 4.1 Introduction

This chapter will present the field observations at the two tillite sites, all the analysis or calculated results about the mineral composition of the tillite, the cement material's chemical composition in it and the observation for the mineral alteration and weathering in the tillites, sone of which are obtained with some modern geochemistry methods mentioned before, such as SEM and EMP. For the Leka tillite, the analyzed minerals or materials in the WDS system of the EMP are all numbered and the relevant analyzed areas are also marked with their corresponding numbers in blue color in the BSE images displayed in the Appendix chapter.

Additionally, as both of the two tillites have apparent contents of quartz found with optical microscope, and quartz can't exist in the ultramafic rock body near the tillite sites, thus the forming reason here is mostly morainic origin instead of local debris flow.

## 4.2 Field observations

### 4.2.1 Field work on the Leka island

The Leka tillite site's coordinates are $65^{\circ}3'37''$ N,$11^{\circ}34'10''$ E , which is at Solsem on Leka Island. Within the outcrop, there are two distinctive layers observed in the site, the boundary between them is represented by a red line refer to the Fig 4.1, the upper one is the layer of the interested tillite, while the lower one is the partly carbonated serpentinized ultramafite as bedrock. The thickness of the tillite layer is up to 2 meter (the length of the hammer is about 1m refer to the Fig 4.1). There are lots of lithic clasts/fragments consolidated in the tillite, most of them are pieces or blocks of ultramafic or mafic rock, which indicates that the Leka Ophiolite Complex is one of the material sources for the formation of the tillite here. The size of the clasts ranges from around 1mm to about 0.5m. The majority of these clasts have angular shapes, rarely round or sub-round. Besides, these clasts have been bound together tightly by some kind of material that cannot be distinguished directly and could be sort of natural-formed

cement, this is quite an interesting observation as these findings coincides with the proposition of this research paper.

Near the tillite site there is a pile of clasts consisting of ultramafic rock and the tillite pieces, and it is considered that they are transported from the tillite site by some unconfirmed excavation activities.

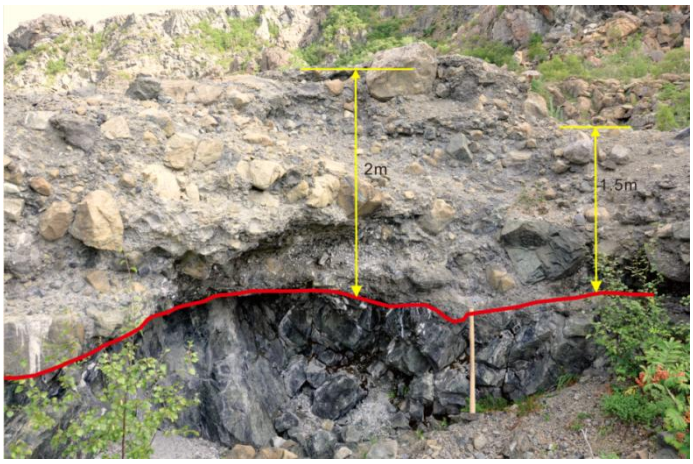


**Fig 4.1 The overview images about the Leka tillite site.**

In the layers, some kind of white material is found. but these fragments of ultramafic rock located on the boundary are seriously covered by the white material, which is distinguished as magnesium carbonate in the later analysis of XRD after collecting them. During the field observation, the author thought that the formation of the natural cementing material could possible be related to the weathering processes happening within these serpentinized ultramafic rock fragments and analyse the white powders (refer to Fig 4.3) could provide some useful information about it.

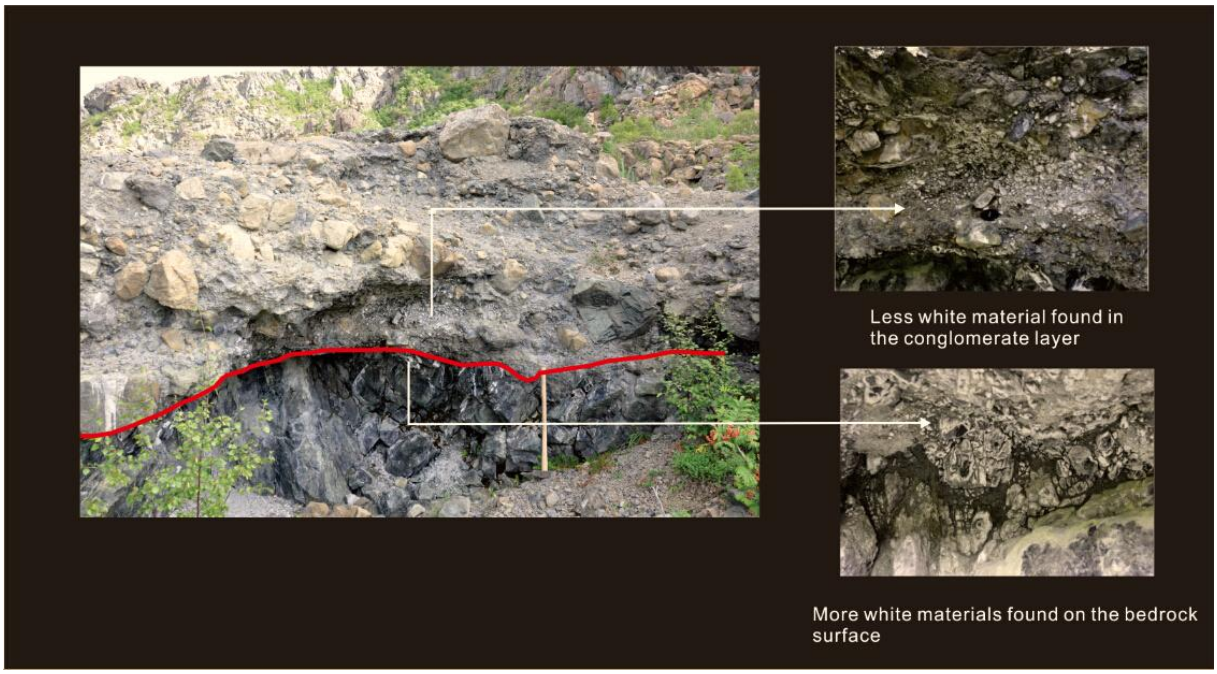


**Fig 4.2 White materials growing on fragments' surfaces**

**The Samples from the Leka tillite site**

Four rock samples were collected from the tillite locality at Leka, three of which are from the main tillite displayed in the Fig 4.4. The other sample is of those white powdery materials on ultramafic fragments, shown in Fig 4.3. The sample of such materials, the author named it as WP-2014. It will be analysed by XRD.

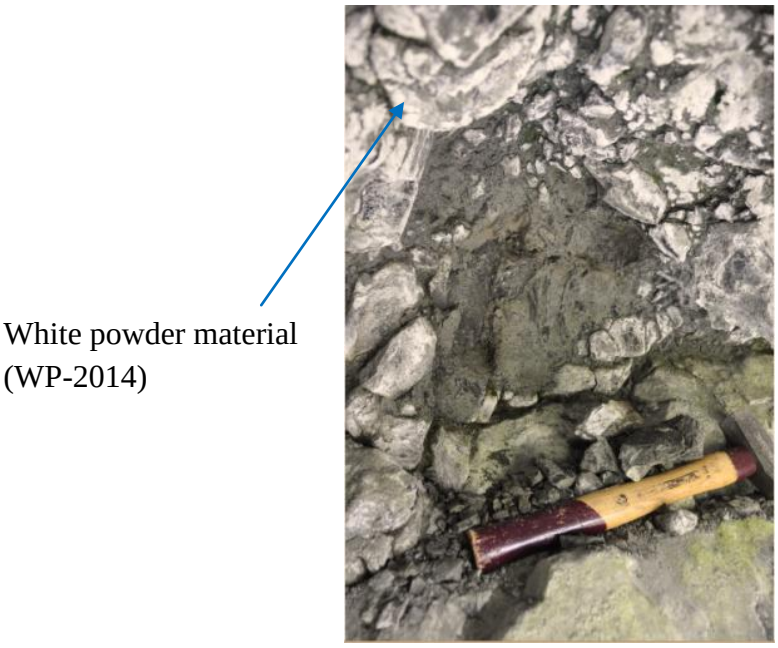


**Fig 4.3 Sample WP-2014 (Photo taken with camera upward)**

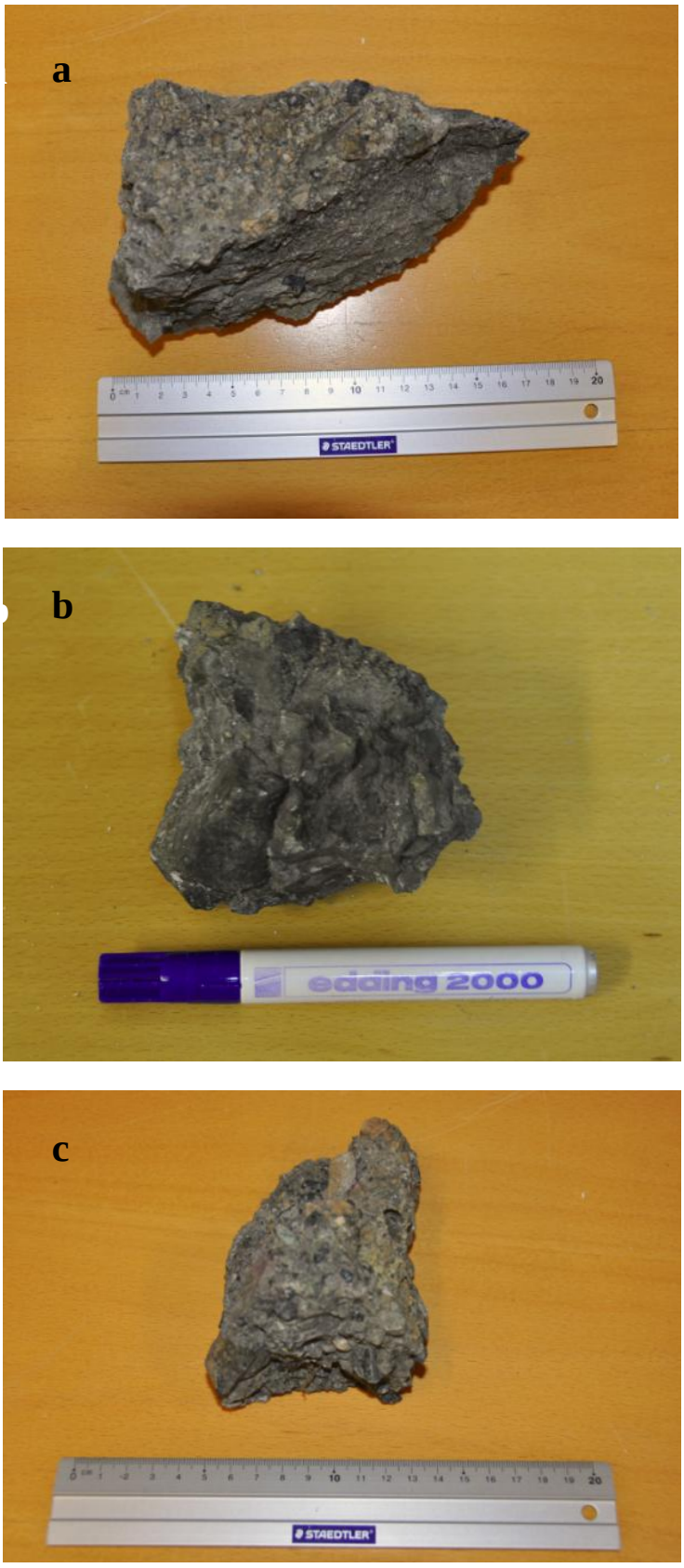


**Fig 4.4 Three concrete samples from the Leka Island; (a) Sample LK14-GC-1; (b) Sample LK14-GC-2; (c) Sample LK14-GC-3**

## 4.2.2 Field relationship of Feragen tillite

Tillite has been found at three localities at Feragen. The localities are numbered as location 1, location 2 and location 3 in Fig 4.5. The three tillite outcrops are lithified, which contains similar rock fragments and clasts that have been observed. The Feragen tillites are found in two settings : 1) the lithification of moraine is confined to 1 m of the wall of the shaft cutting (location 1, refers to Fig 4.8); 2)tillite is found in the peaty area where tillite blocks are up to 0.5 $m^3$ and they seems to be linked to the drainage of mine tailings (location 2, refers to Fig 4.9).Additionally all of the tillites are grayish, strong and sitiuated on the Feragen ultramafic body.


**Fig 4.5 The satellite image about the Feragen area and the tillite locations (Li et al., 2013)**

### Location 1

Location 1 is 700 m northwest to Stensgruva where an upper shaft and a lower mine opening are found on a north facing hillside slope. A large number of angular mine tailings in cobble- to boulder sizes are located along the slope as well, which are from a nearby shaft. These tailings are weathered, and are good examples of the carbonation phenomenon. Mine tailings can be seen by excavating them, as demonstrated in the Fig 4.7 (a). The lithfied tillite is observed within both walls of a channel, which has been previously excavated, to the lower mine opening at the location 1. However, the lithification is constrained to 1 meter of the channel wall (Fig 4.7 b & Fig 4.8 b). Loose

soil is found after excavating over the lithification part inward the channel wall. There are two stratigraphic logs finished about the walls of the channel at different places, which are profile I and profile II displayed in the Fig 4.8. From the two profiles, it is obvious that the tillite is covered by some soil and mine tailings, consisting of poorly sorted angular to subrounded clasts ranging from gravel- to cobble sizes. These are supported by brownish silty and sandy materials. The clasts are from slightly and moderately weathered serpentinized ultramafic rock fragments, which is similar as the tillite found on Leka Island. Nevertheless, the cobbles to boulders are only found in the upper part of the tillite deposit at Location 1 demonstrated by the profile I in Fig 4.8 (a). Similarly, the cobbles or boulders are partly coated with the white materials, which is confirmed as some hydrated magnesium carbonates(Beinlich and Austrheim, 2012). The thickness of the tillite layer is from around 30 to 55 cm. Furthermore, there is no fracture pattern or any previous tectonic remants happening in this region kept by the ultramafic bedrock body, can be found in the tillite layer. The contact between the tillite layer and the bedrock dips at roughly 40° within the profile II and is consistent with the topography of the bedrock underlain.


**Fig. 4.6 The overview of the location 1**(Li et al., 2013)

(a)

(b)

**Fig.4.7 (a) The carbonation on the mine tailings; (b) Heavily weathered and loose soil observed after excavated the wall of the channel inward**(Li et al., 2013)**.**

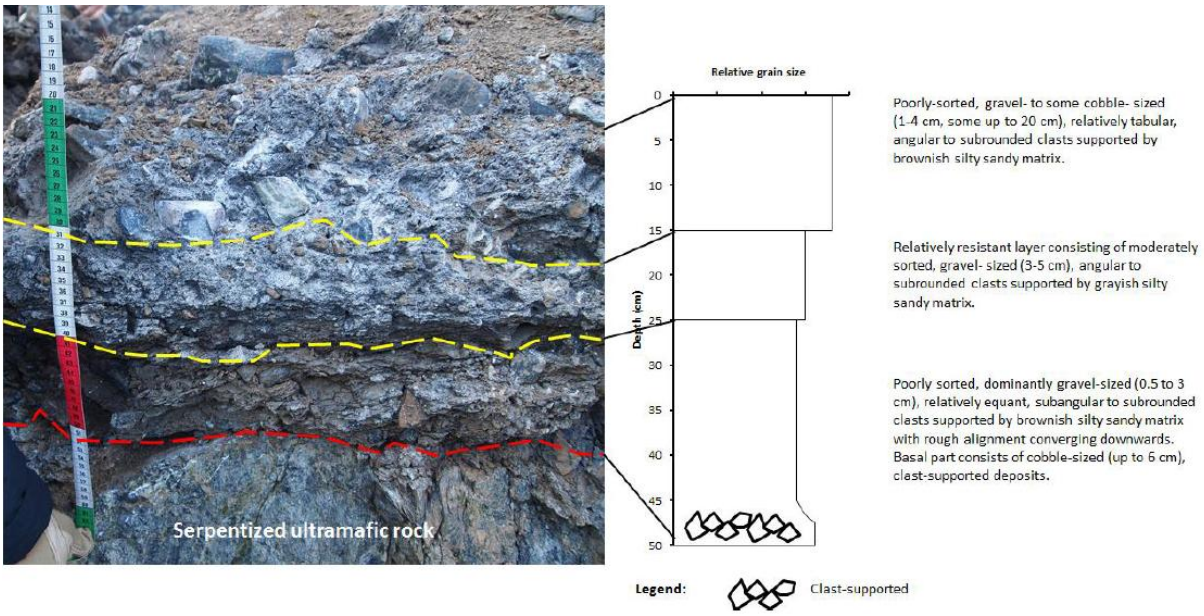


**(a)**

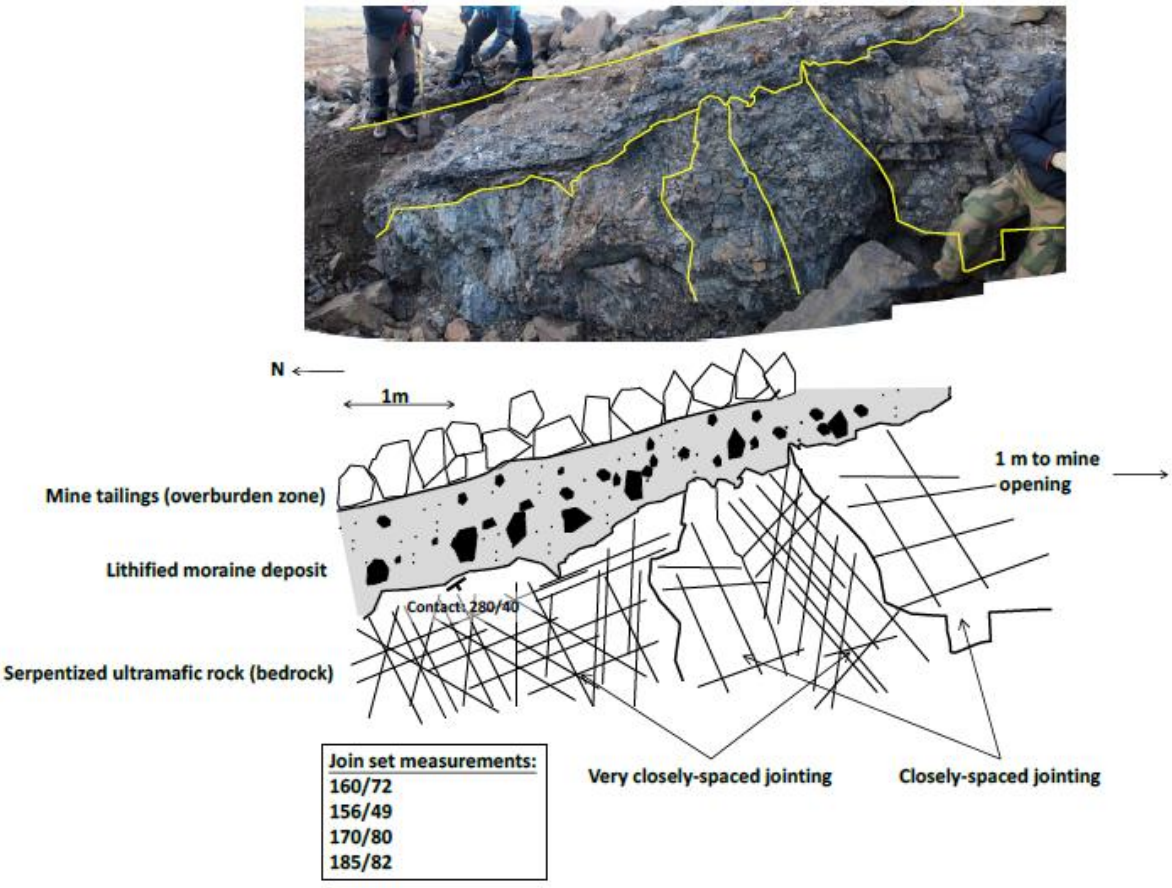


**(b)**

**Fig.4.8 (a)The profile I of the channel wall containg the tillite at location 1; (b) The profile II from a different part of the channel at location 1 with its schematical diagram**(Li et al., 2013)**.**

**Location 2**

Location 2 is a flat area 170m NE from the location 1, where several grayish consolidated tillite deposits are exposed. The tillite deposit in Fig 4.9 is near a northward running creak origining from a nearby mining site about 100m upslope, which is indicated by a small red arrow in the Fig 4.9. Within the field work for Feragen at 2013, some loose morainic deposits were observed along the creak, which have apparently been eroded by water. The fragments in the lithified tillite at location 2 are from serpentinized ultramafic rock, granite and quartzite in sizes from gravel to cobble. Similarly, it is supported by silty and sandy materials as well.

**Fig. 4.9 One exposed tillite site at location 2**(Li et al., 2013)

## Location 3

The location 3 is at the Stensgruva mine opening and there is also a channel to the mine opening. The tillite deposit observed at location 3 is within both of the channel's walls. Here the tillite deposit consists of the fragments from the same rock types as location 1, which is also supported by sandy and silty matrix and covered by top soil. However, the tillite of location 3 is found at deeper depth than the previous one at location 1, which is about 0.6 to 0.8 meters.


**Fig. 4.10 The general view for the location 3**(Li et al., 2013)

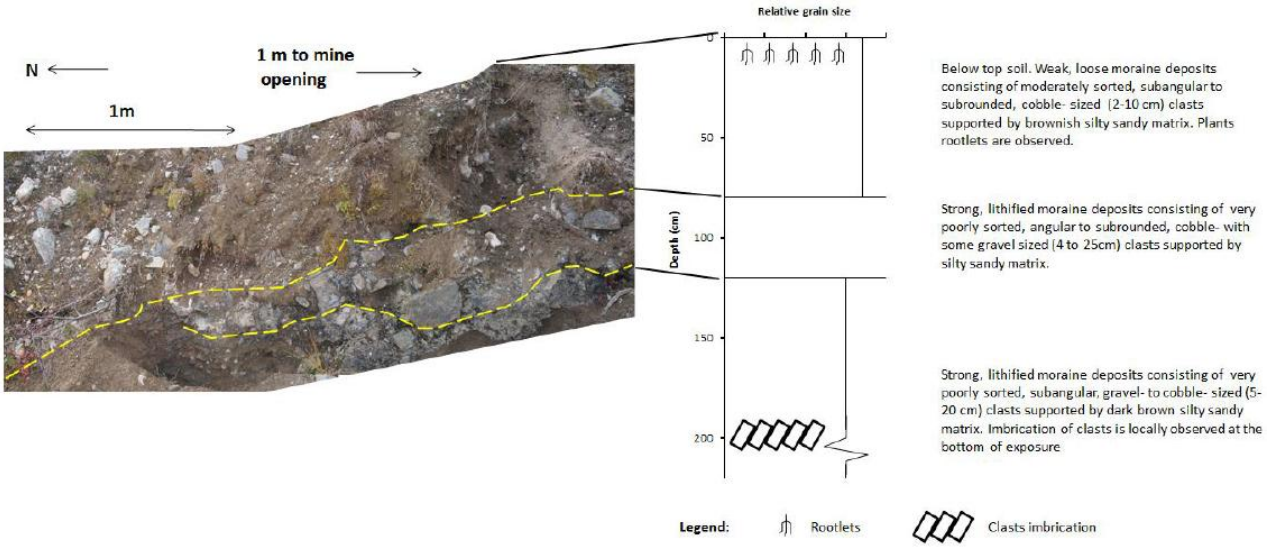


**Fig.4.11 The stratigraphic profile for one wall of the channel at location 3**(Li et al., 2013)

## pH measurements in the Feragen area in the laboratory

**Table 4.1 Measurement for pH in the Feragen area**(Li et al., 2013)

| pH data No. | Measure position | UTM Coordinates | Measured pH value |
|---|---|---|---|
| 1 | A pond | 32V 0644604 E 6940078 N | 7.3 |
| 2 | A creak | 32V 0644379 E 6940250 N | 7.65 |
| 3 | The mine site 100m upslope to the location 2 | 32V 0643719 E 6940293 N | 9.1 |
| 4 | The mine site at location 1 | 32 V 0643616 E 6940334 N | 9.34 |
| 5 | The creak running through the location 2 | 32 V 0643752 E 6940426 N | 8.0 |
| 6 | Another creak 200m NE to location 3 | 32 V 0644168 E 6940348 N | 7.63 |

In total, there are six measurements for pH value performed in the Feragen area, which cover the three locations for the Feragen tillite. Both of the three measurements from the tillite outcrops are basic, while the other 3 values from other places in the Feragen area are neutral. The remain mining site 100 m upslope to the location 2 and the mining site near the location 1 have the highest pH values, which are 9.1 and 9.34 respectively. The creak running through location 2 has a lower value as 8.0 that is still a

little basic. The details about each pH measurements have been converted into tabulated form and can be observed in table 4.1.

In addition, the field measured pH data, there are 3 pH values obtained in the laboratory for the Feragen tillite after crushing and then dissolving them into pure water. All of the 3 laboratory values are ranging from 8.7 to 9.8, which are consistent with the field values.

## 4.3 The thin-sections for the Leka tillite

(a) (b)

**Fig.4.12 Scanings of thin sections from concrete samples; (a) LK14-GC-1a; (b) LK14-GC-1b**

The raw rock samples of the Leka tillite have been processed into thin sections, demonstrated in Fig 4.12. It is necessary to observe them with optical microscope to see the mineral's texture, alteration extent of some mineral grains, weathering effect on minerals in the tillite, and estimate the distribution of sizes of grains.

## 4.4 Petrography and mineral chemistry of the Leka tillite

The Leka tillite is composed of lithic fragment of both minerals and rock. Most of the materials is from bedrock, but there are also materials that are derived from further away, such as quartz and feldspar. The fragments are common in angular to sub-round shapes. The larger grains sit in a finer grained matrix dominated by serpentine but also contain olivine and opaques, displayed in Fig 4.13(d). The fine grained nature of the material do not allow an assessment of the cement that binds the grains together. The larger serpentinized peridotite fragment is usually found to be accompanied with some

partly corroded quartz grains (refer to Fig 4.13 a, b, c). Fig 4.14 shows three corroded quartz grains, and other fragments distribute randomly around these quartz grains. Within the peridotite fragments or the dark matrix, pores can be observed, which are resulted by the dissolution processes in the Leka tillite.

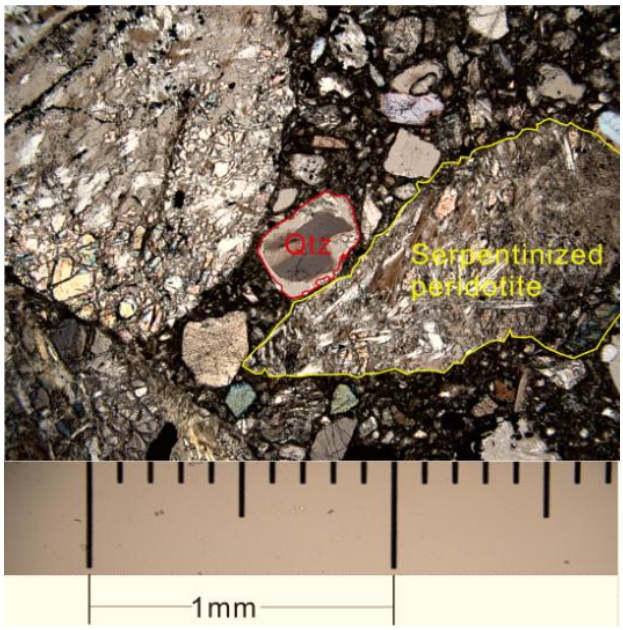


**(a)**

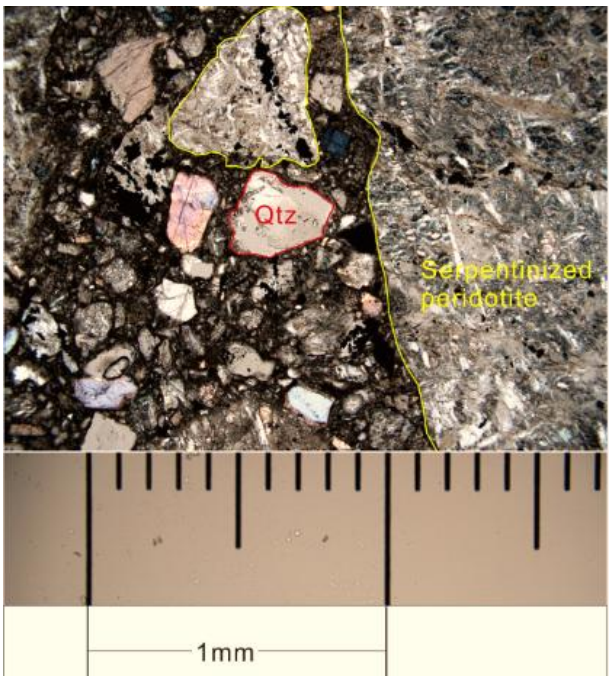


**(b)**

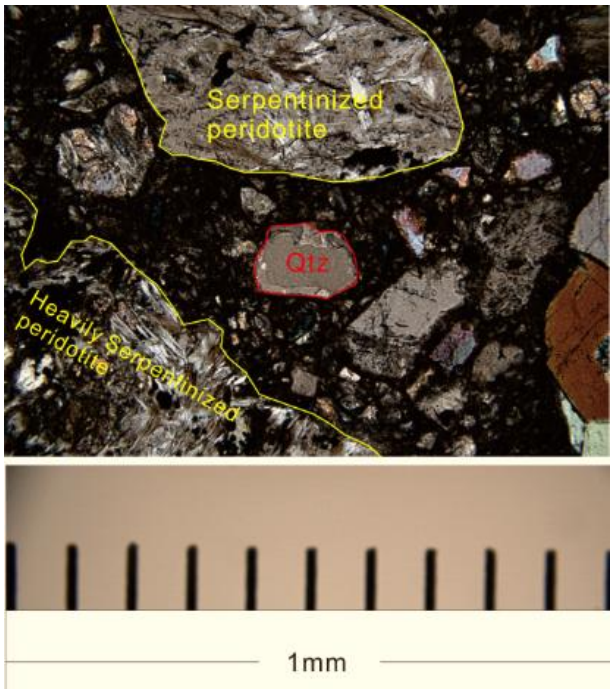


**(c)**

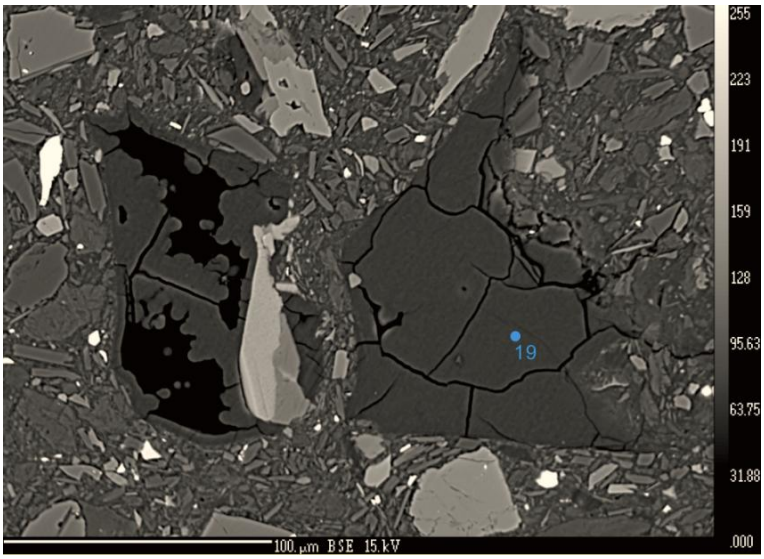


**(d)**

**Fig 4.13 Photomicrographics (taken with XPL) and BSE image of the Leka tillite with scales.**

Both quartz and feldspar display textural evidence for dissolution using EMP and SEM (refer to Fig 4.14). Fig 4.14 is obtained in the thin section **LK14-GC-1a**. In the case of feldspar the dissolution is also seen to make finers into the core of the mineral (Fig 4.14). There are some narrow porous spaces along the larger serpentine grain's boundary, which are partly filled with calcite. Furthermore, there are some tiny calcite clasts attached to the left bottom corner of the quartz grain, indicated in Fig 4.14.

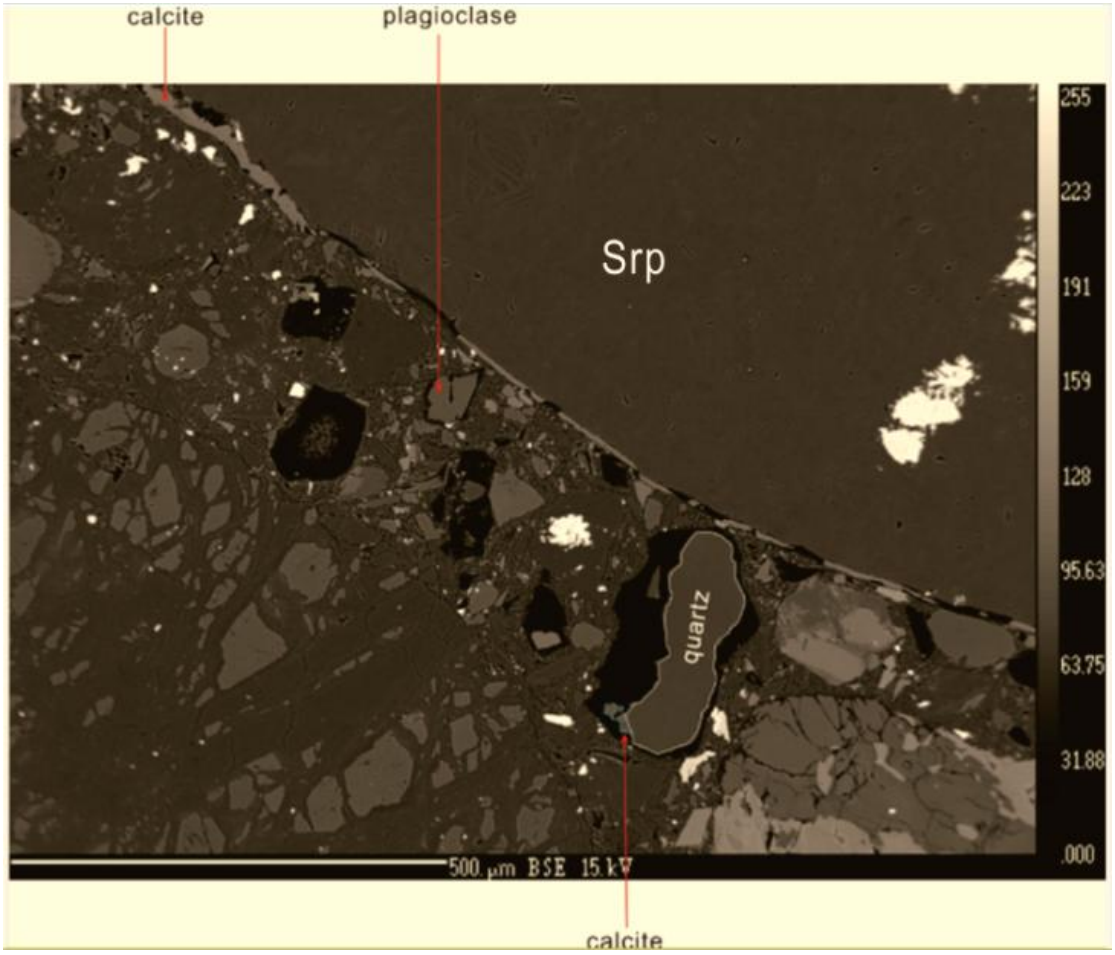


**Fig 4.14 BSE photo of tillite from Leka. Note pore around dissolving quartz.**

### 4.4.1 Quartz weathering phenomenon occurring in the Leka tillite

In the SEM and EMP observations from the Leka tillite samples, the details about the quartz enable for further observations of the quartz mineral during the deposit process, because of the two advanced methods can provide more powerful functions for geochemistry analysis and observation.

The phenomenon that quartz grain accompanied with some carbonate minerals is very widely occurring in the tillite. For example, there is quartz grain and two calcite grains existing in the same hole, where a tiny dolomite grain is found as well, displayed in Fig 4.15(a), these mineral grains have been analysed with the EDS system of SEM and the corresponding spectra are shown as well. Furthermore, a quartz grain around 200 um in size that has been dissolved irregularly (Fig 4.15 (b)). This is contacting with two

calcite clasts at both its upper and lower left bottom, displayed in Fig 4.15(b). Additionally, it is observed that quartz has been dissolved into different part by the dissolution as there is a smaller remnant left close to the larger one, and they are considered to be from a same original grain that occurred in the hole.

In addition, the contact relationship between quartz and carbonate in the tillite is not only that contact with each other on boundary, but also it can be embedded into the other one. For instance, there is a weathered quartz grain that is embedded by the calcite mineral, denoted with No.15 (Fig 4.16 (a)), and the boundary of the hole which contains the calcite and the quartz is completely attached with the cement. The cement even goes into the quartz grain along the calcite.

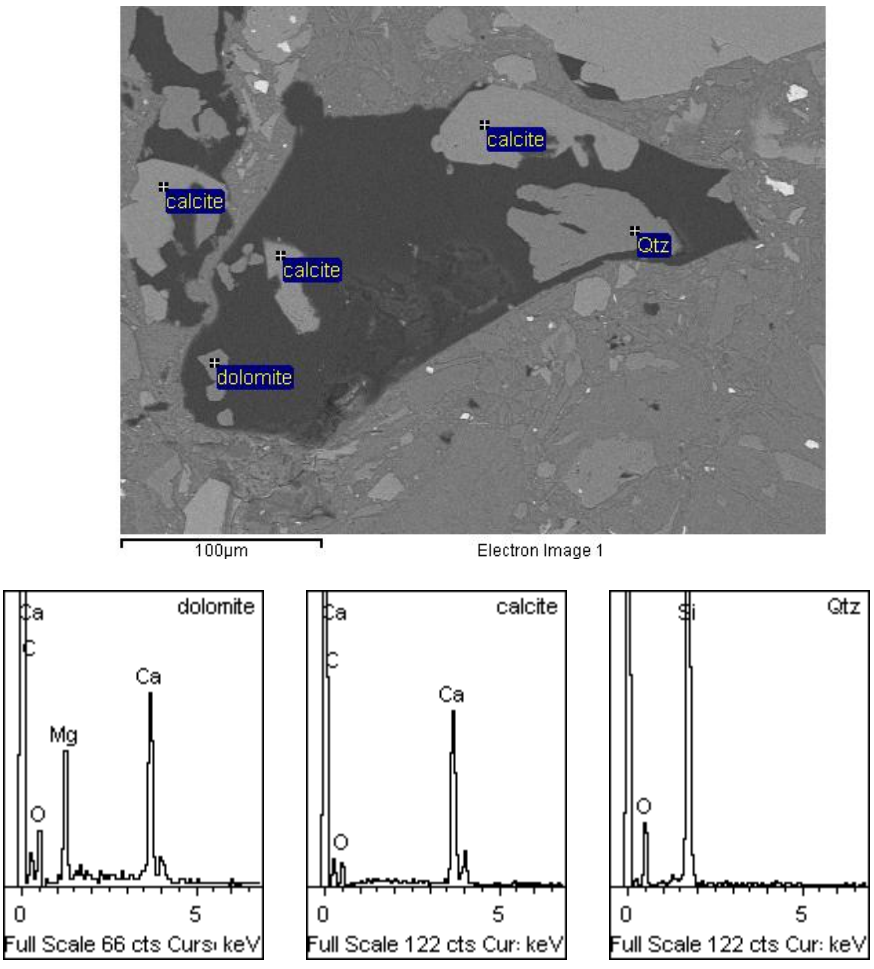


(a) A weathered quartz grain with calcite and dolomite in a same hole in the Leka tillite with related spectra. (Taken in the thin section LK14-GC-1a)

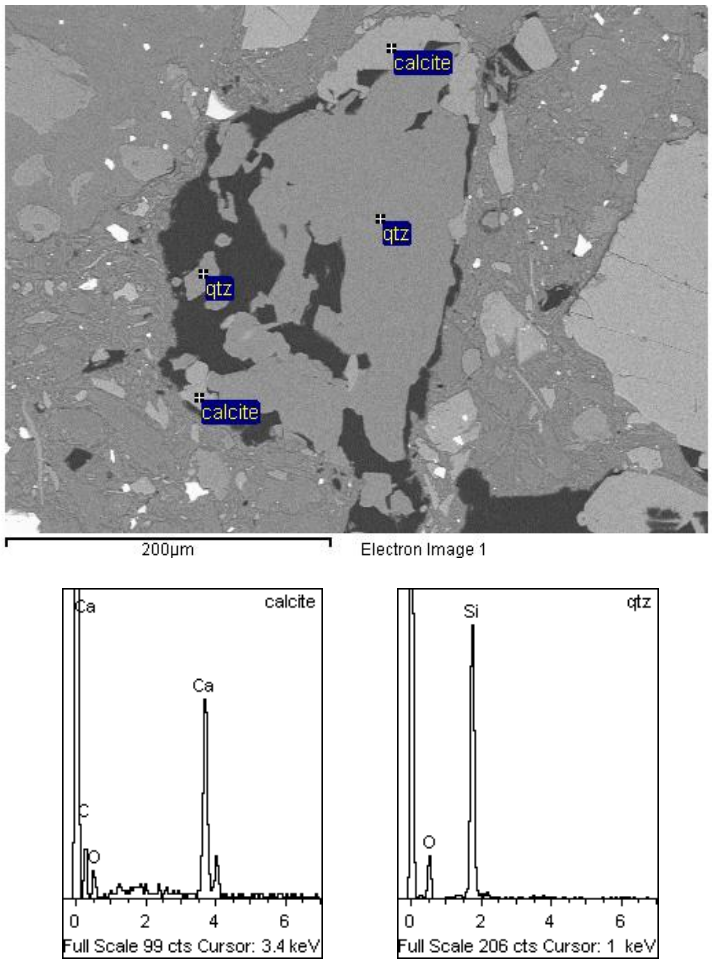


(b) A weathered quartz grain contacted with carbonate minerals.

**Fig 4.15 Backscattered electron images displaying the situation where the weathered quartz contacted with carbonate mineral**

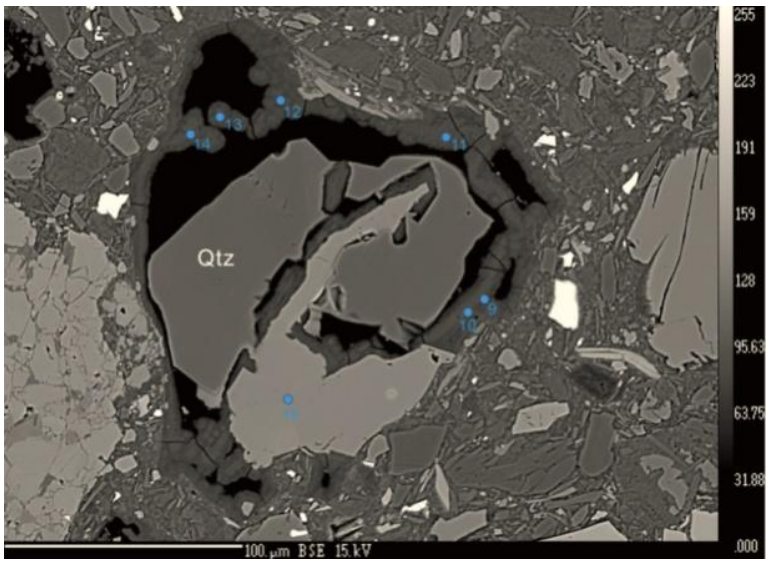


(a) A quartz grain embedded by calcite and cement

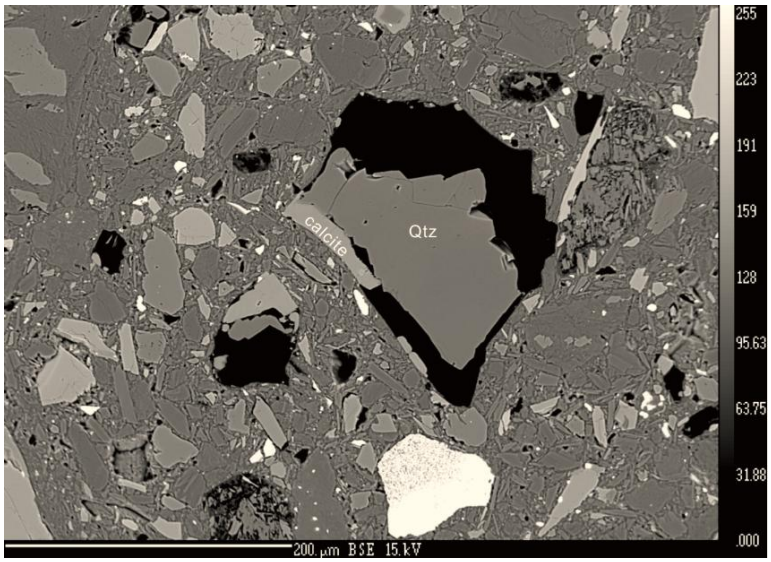


(b) A dissolved quartz with similar boundary shape to the hole

**Fig 4.16 The BSE images about the quartz weathering in the Leka tillite. (taken by EMP)**

In Fig 4.16 (b), it can be observed that the quartz grain partly remains in its original shape. Additionally, the dentate shape of the quartz is consistent with the boundary of the hole. Furthermore, the hole shape can be considered as the initial one, where a calcite slice is underneath the quartz.

## 4.4.2 Cement in Leka tillite

The optical image displays that the Leka tillite is supported by fine grained matrix. With the help of SEM and EMP, the details and chemical composition of the matrix can be shown clearly and obtained accurately. Through the use of SEM, some quartz grains are found to be surrounded by magnesium silicate. A pyramid-form quartz grain situates inside a sub-square hole that is partly filled by the cement, where the spectrum 2 is for the quartz grain and the spectrum 1 represents the cement, displayed in Fig 4.17. It is found in a stub from the sample LK-GC-1a in the SEM observation. The cement spectrum have three high peaks of Si, Mg and O. However, the spectrum 2 for the quartz should only have the two peaks for Si and O, the small peak of Mg in the spectrum 2 is due to that the analysis for the quartz is influenced by the cement nearby as the detecting area of incident beam in the SEM covered some cement when analyse the quartz grain.

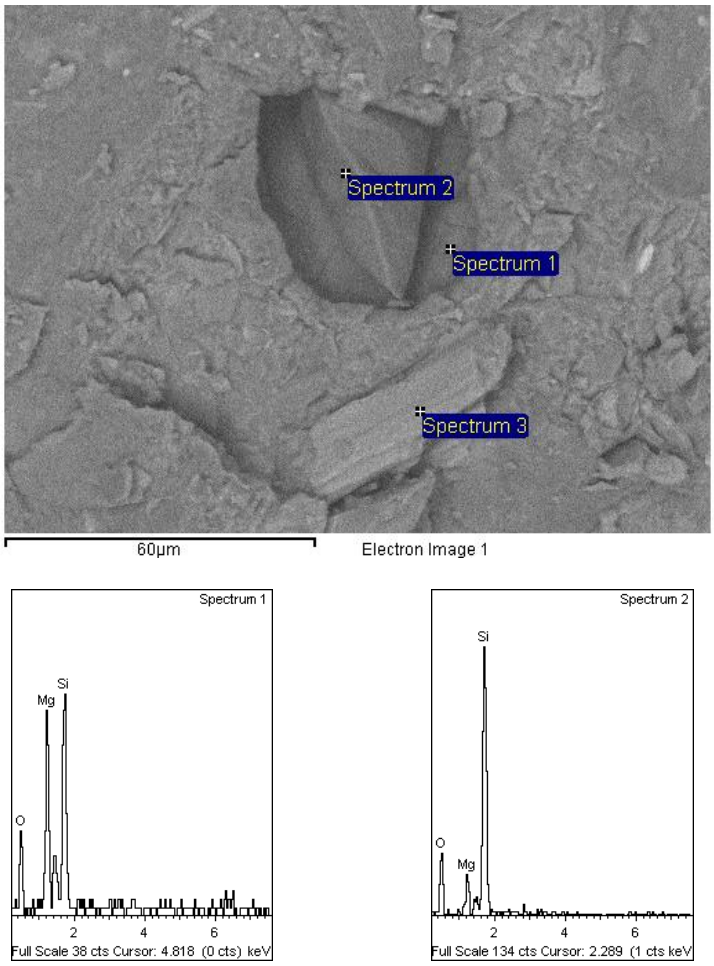


**Fig 4.17 The BSE image containing a quartz grain in a hole filled with the cement. Spectrum 1 representing the cement and spectrum 2 representing the quartz**

Spectrum 1, which represents cement, demonstrates that the Si peak in the cement is the highest here, while the Mg peak is a little less than that of Si. In addition, during the analysis of the thin-section LK14-GC-1b in the EMP, there are some similar phenomena found where these dissolved quartz grains are enclosed by cement. This is displayed in Fig 4.18. Referencing Fig 4.16 (a), it can be observed that the cement replaces the porous space resulted from the weathering. In Fig 4.18 (b), there is a quartz grain with cement occurring within the same hole, which can be seen in the lower section of the image. However, in the upper and larger hole, the quartz grain is mixed with calcite fragments with cement filling in the fractures between them.

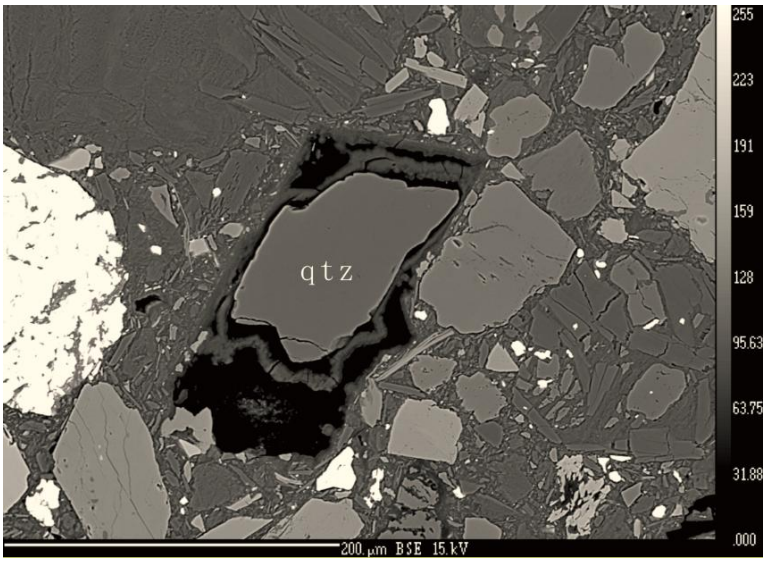


(a)

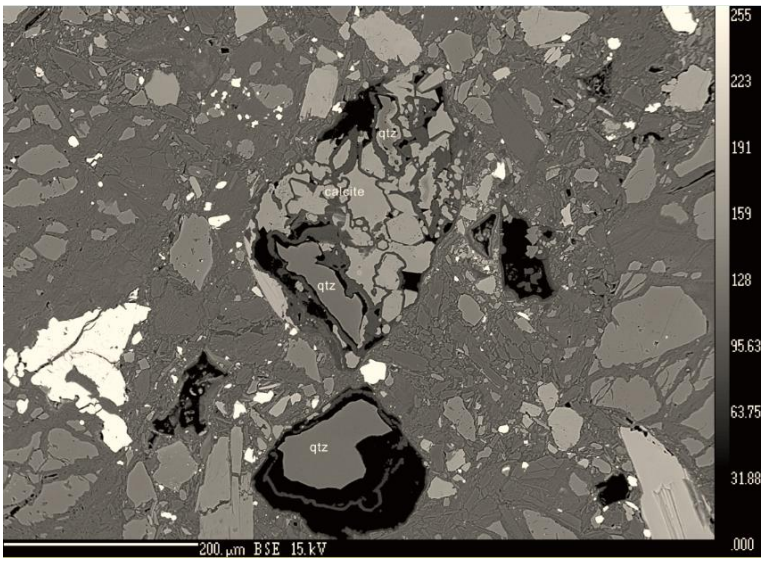


(b)

**Fig 4.18 The BSE images showing the situation that quartz surrounded by the cement**

Incidentally, cement is not only found near the quartz or carbonate minerals. The weathering of feldspar minerals is observed to be closely related with the cement generation and growing in the Leka tillite as well.

## 4.4.3 Feldspar dissolution

K-feldspar and plagioclase exist in the Leka tillite. The occurrence of the K-feldspar implies that the material source for the Leka tillite is not only the Leka ophiolite complex, but it also contains mineral from outside the Leka island. It will be discussed later in the chapter of Discussion about the material sources for the Leka tillite. Feldspar minerals are usually unstable under the earth surface environment, which can be easily weathered or dissolved by the surface fluids. In the Leka tillite, the feldspar grains, which are observed to be corroded in different levels, and the cement around them.

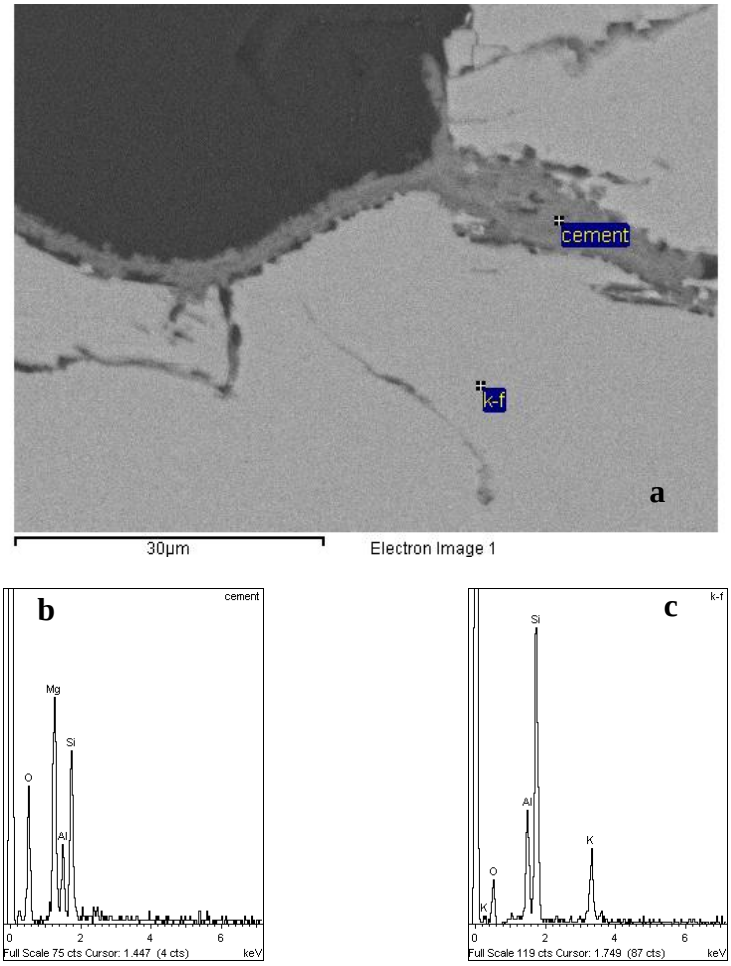


**Fig 4.19 a) K-feldspar grain rimmed and veined by cement. b) EDS sectra of Al- containing cement. c) EDS spectra of K-feldspar.**

For example, Fig 4.19 (a) displays the boundary of K-feldspar, which is covered by cement, with the cement filling up the fracture space inside it. It is apparent that the cement observed has a significant difference to those cements previously mentioned because of the cement contains aluminum in addition to Mg, Si and O, supported by the

spectrum in the Fig 4.19(b). Furthermore, the peak of Mg is higher than that of Si in the cement, whereas those cements near quartz or calcite always have higher peaks for Si. These characteristics are only found for the dissolved feldspar grains in Leka tillite.

Plagioclase is a solid-solution series between the end members albite and anorthite. The dissolution of plagioclase may be dependent on its composition. Thus, Leka tillite plagioclase grains show different dissolution phenomenons, because their compositions are not the same. This can be observed in Fig 4.20. The plagioclase grian (denoted with number 2 ), which has been dissolved mainly along the boundary. Consequently there are more than 60% of the grain left. However, the grain, denoted as 5 in Fig 4.20 (b), has been selectively dissolved along vein-like structures, which has led to a fragmentation of the grain. Furthermore, there is a smaller fragment left from a weathered plagioclase grain (number 8) that has been dissolved to be less than half of its initial area in Fig 4.20 (b). The composition of plagioclase may influence the dissolution rate and explain why some grains are more strongly dissolved than others. The dissolution along veins suggests that the process are more complicated. The analysis results for the feldspar compositions will be present in the next section.

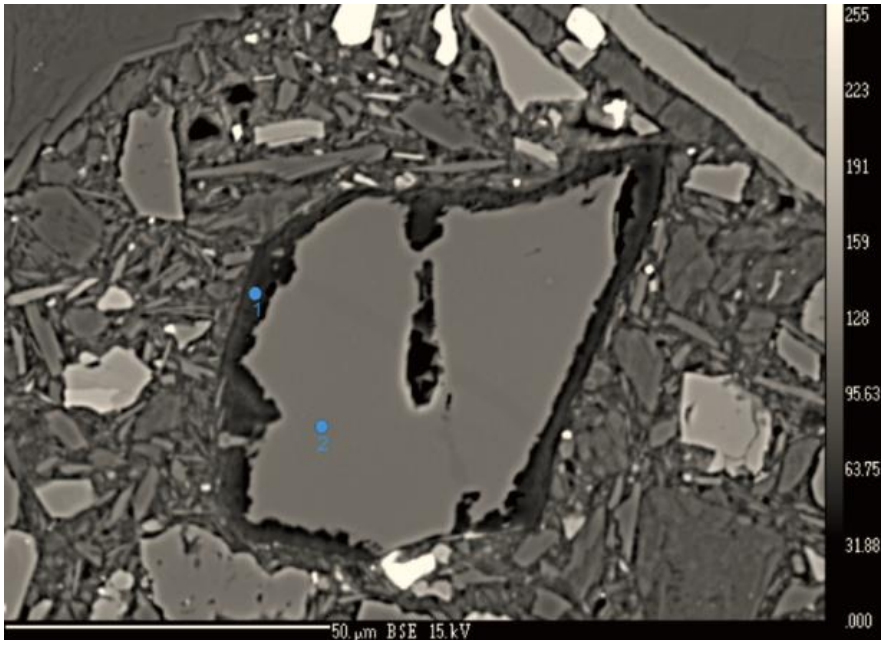


(a)

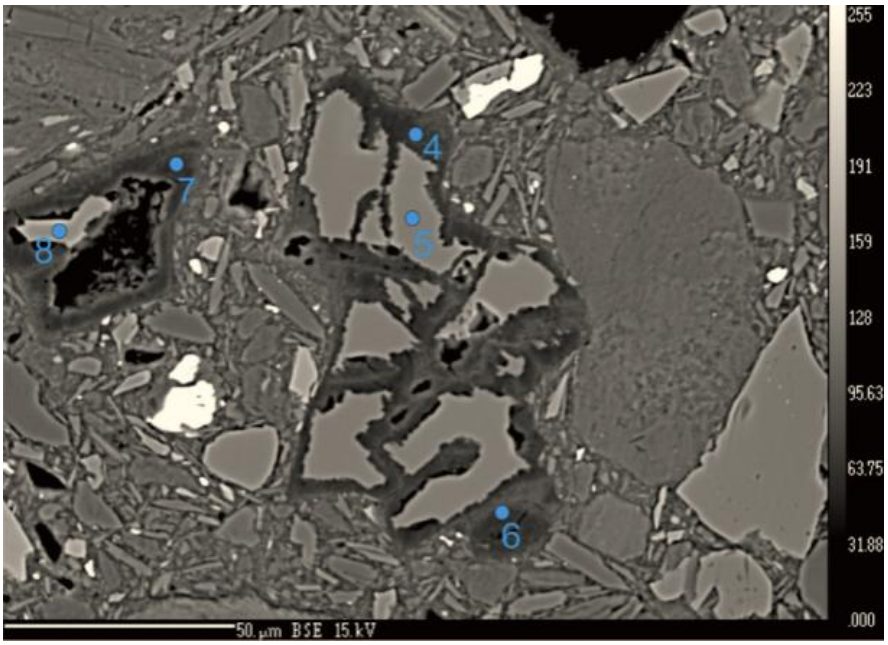


(b)

**Fig 4.20 Fragmentation of plagioclase grain by preferential dissolution along vein or finger-like structures.**

## 4.4.4 Composition of cement and the minerals in the Leka tillite

There are about 50 analysis finished with the WDS system of EMP in the Leka tillite thin-sections, which covers quartz, feldspar, cement and carbonate. It provides more accurate evidences for the weathering influence happening in the tillite during the deposit process.

### a Feldspar composition

A total of 10 partly dissolved grains were analysed by EMP(WDS). Each chemical formula of feldspar grains is listed in table 4.2 below, which contains their corresponding analysis sequence number. Furthermore, the molar content for each end member in feldspar group is also included. In addition, the BSE images and raw data of WDS analysis for these feldspar, quartz, carbonate and cement can be found in Appendix A & B.

**Table 4.2 The structural formulae of feldspar resulted from WDS analysis (Leka Tillite)**

| *Feldspar grain* | *Structural forumula* | *Albite%* | *Anorthite%* | *K-feldspar%* |
|---|---|---|---|---|
| 2 | $Na_{0.61}Ca_{0.40}K_{0.01}Al_{1.36}Si_{2.62}O_8$ | 56 | 43 | 1 |
| 3 | $Na_{0.62}Ca_{0.40}Fe_{0.01}Mg_{0.01}Al_{1.38}Si_{2.60}O_8$ | 57 | 43 | 0 |
| 5 | $Na_{0.59}Ca_{0.44}Mg_{0.09}Fe_{0.01}Al_{1.43}Si_{2.51}O_8$ | 53 | 47 | 0 |
| 8 | $Ca_{0.88}Na_{0.11}Fe_{0.01}Al_{1.86}Si_{2.12}O_8$ | 10 | 90 | 0 |
| 20 | $Na_{0.68}Ca_{0.32}Al_{1.30}Si_{2.69}O_8$ | 65 | 35 | 0 |
| 29 | $K_{1.01}Na_{0.02}Al_{1.03}Si_3O_8$ | 1.9 | 0 | 98.1 |
| 32 | $Na_{1.02}K_{0.01}Ca_{0.01}Al_{0.99}Si_{2.99}O_8$ | 98 | 1 | 1 |
| 39 | $Na_{1.01}K_{0.01}Ca_{0.01}Al_{1.01}Si_{2.99}O_8$ | 98 | 1 | 1 |
| 46 | $Na_{0.72}Ca_{0.31}Fe_{0.01}Al_{1.30}Si_{2.69}O_8$ | 67 | 33 | 0 |
| 50 | $Na_{0.75}Ca_{0.24}K_{0.01}Al_{1.23}Si_{2.76}O_8$ | 72 | 27 | 1 |

Reviewing the analyzed results in table 4.2, 8 out of the 10 feldspar grains contain more than 50% albite. Grains 32 and 39 are almost pure albite, whilst 9 grains contain not more than 1% K-feldpsar. However, the grain 29 is almost pure k-feldspar. In addition, it is more intuitive to understand the classes of the 10 found feldspar grains in Leka tillite with the help of the triangular diagram in Fig 4.21 where the triangle has albite, anorthite and k-feldspars as the end members at each angle, and each side is divided equally into 10 sections. In addition, there are 10 grains are plotted upon the diagram based on their weight fractions of these end members, which are obtained by relevant calculation based on the molar fractions in the table 4.2. The bottom side is for the plagioclase group includes the grains 2, 3, 5, 8, 20, 32, 39,46 and 50, while the grain 29 is close to the corner of K-feldspar.

As there are some sub-types in the plagioclase group, the 9 grains of the plagioclase are thus divided more based on their albite wt%, which can be observed in the table 4.3. Consequently, andesine is the most commom type feldspar in the tillite, while the albite is the second most common. Oligoclase or bytownite only has one member.

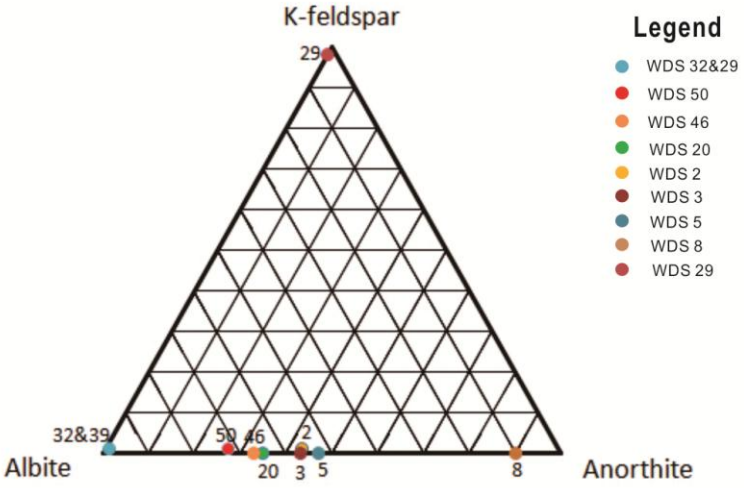


**Fig 4.21 Triangular diagram for feldspar classfication**

**Table 4.3 Sub-classification for plagioclase grains**

| *Variety* | *Albite fraction,* | *Grains* |
|---|---|---|
| Albite | 100% to 90% | 32,39 |
| Oligoclase | 90% to 70% | 50 |
| Andesine | 70% to 50% | 2,3,5,20,46 |
| Labradorite | 50% to 30% | |
| Bytownite | 30% to 10% | 8 |
| Anorthite | 10% to 0% | |

## b Composition of the cement

From the EDS spectra it can be seen that Mg, Si and O are the dominant elements in the cement. In addition, Al is present in cement adjacent to dissolving plagioclase. Nevertheless, it is not accurate enough to just know how much for each of the constituting elements in the cement. The EDS spectra are unable to provide enough information about minor elements in the cement. However, this may have some significant indications. Therefore, it is necessary to use WDS method to check the composition of the cement, and the structural formulae for the cements. These WDS analysis data calculations can be found in table 4.4. The mineral grains that are surrounded by the cements are also stored in the right column of the table 4.4.

**Table 4.4 Structural formulae for the cement in Leka Tillite (Normalized to 8 oxygens)**

| *WDS analysis number* | *Chemical formula* | *Surrounded mineral grain* |
|---|---|---|
| 1 | $Mg_{1.27}Na_{0.01}Ca_{0.02}Fe_{0.02}Ni_{0.01}Al_{0.52}Si_{0.79}O_{3.69}(H_2O)_{4.31}$ | Andesine |
| 4 | $Mg_{1.96}Al_{0.77}Si_{0.28}O_{3.68}(H_2O)_{4.32}$ | Andesine |
| 6 | $Mg_{1.81}Al_{0.77}Si_{0.29}O_{3.54}(H_2O)_{4.46}$ | Andesine |
| 7 | $Mg_{1.80}Fe_{0.01}Ni_{0.01}Al_{0.76}Si_{0.3}O_{3.55}(H_2O)_{4.45}$ | Bytownite |
| 9 | $Mg_{0.42}Si_{1.38}O_{3.18}(H_2O)_{4.82}$ | Corroded quartz and calcite |
| 10 | $Mg_{0.94}Ca_{0.01}Si_{1.40}O_{3.74}(H_2O)_{4.26}$ | The same as 9 |
| 11 | $Mg_{0.64}Ca_{0.01}Si_{1.29}O_{3.23}(H_2O)_{4.77}$ | The same as 9 |
| 12 | $Mg_{0.63}Si_{1.45}O_{3.53}(H_2O)_{4.47}$ | The same as 9 |
| 13 | $Mg_{0.45}Si_{1.35}O_{3.16}(H_2O)_{4.84}$ | The same as 9 |
| 14 | $Mg_{1.06}Ca_{0.01}Si_{1.45}O_{3.96}(H_2O)_{4.04}$ | The same as 9 |
| 18 | $Mg_{1.06}Al_{0.01}Si_{1.26}O_{3.61}(H_2O)_{4.39}$ | Unknown |
| 19 | $Mg_{1.97}Ca_{0.01}Mn_{0.01}Al_{0.01}Si_{1.54}O_{5.08(}H_2O)_{2.92}$ | Unknown |
| 19* | $Mg_{2.02}Ca_{0.01}Si_{1.57}O_{5.17}(H_2O)_{2.83}$ | Unknown |
| 21 | $Mg_{1.83}Na_{0.06}Ca_{0.06}Fe_{0.03}K_{0.01}Si_{1.00}O_{4.95}(H_2O)_{3.05}$ | Andesine |
| 22 | $Mg_{1.82}Na_{0.15}Ca_{0.12}Fe_{0.01}Al_{0.95}Si_{1.11}O_{5.67}(H_2O)_{2.33}$ | Andesine |
| 30 | $Mg_{1.83}Al_{0.51}Si_{0.39}O_{3.39}(H_2O)_{4.61}$ | K-feldspar |
| 33 | $Mg_{2.19}Fe_{0.01}Al_{0.53}Si_{0.65}O_{4.30}(H_2O)_{3.70}$ | Plagioclase |
| 37 | $Mg_{2.01}Al_{0.03}Si_{1.63}O_{5.31}(H_2O)_{2.69}$ | Corroded quartz |
| 38 | $Mg_{2.45}Na_{0.03}Ca_{0.01}Ni_{0.01}Al_{0.62}Si_{0.49}O_{4.39}(H_2O)_{3.61}$ | Plagioclase |
| 40 | $Mg_{2.02}Al_{0.16}Si_{1.31}O_{4.98}(H_2O)_{3.02}$ | Calcite |
| 42 | $Mg_{2.03}Ca_{0.01}Fe_{0.01}K_{0.02}Al_{0.08}Si_{1.61}O_{5.38}(H_2O)_{2.62}$ | Mica |
| 44 | $Mg_{2.19}Fe_{0.02}Mn_{0.01}Al_{0.38}Si_{1.31}O_{5.42}(H_2O)_{2.58}$ | Andesine |
| 47 | $Mg_{1.79}Ca_{0.02}Si_{1.82}O_{5.46}(H_2O)_{2.54}$ | Unknown |
| 48 | $Mg_{1.84}Ca_{0.02}Al_{0.01}Si_{1.70}O_{5.27}(H_2O)_{2.73}$ | Calcite |
| 51 | $Mg_{1.72}K_{0.01}Al_{0.68}Si_{0.51}O_{3.78}(H_2O)_{4.22}$ | Oligoclase |

Note: The raw WDS analysis data for the checked cement materials can be found in the Appendix. The 19* means that this point is analyzed with a larger diameter (5um) of the electron beam in the WDS system, while the other points are checked with the smallest diameter of beam in the WDS system (around 1 um).

Table 4.4 shows that the cement can also contain some other elements in some minor contents, which are probably from their surrounded weathered/altered mineral grains except the main elements (Mg, Si and O).

The cement in the Leka tillite can be roughly classfied as two different dominant types based on their WDS analysis results. The first type is named as Type A, whihc has 3 main oxide components that are MgO, $SiO_2$ and $H_2O$. Additionally, the other type cement-Type B has 4 main oxide components of MgO, $Al_2O_3$, $SiO_2$ and $H_2O$. There are 11 analysis points for Type A cement and 13 analysis points for Type B cements within the WDS

analysis for the Leka tillite. Those BSE images for the cement in the Leka tillite are displayed in the Appendix B.

The ratios for $MgO$-$SiO_2$-$H_2O$ in Leka cement are calculated out and listed in table 4.5 (a) & (b). The average ratio between MgO, $SiO_2$ and $H_2O$ in the Type A cement is 1 : 1.63 : 5.02, while the Type B cement has an average ratio of 1 : 0.43 : 1.94 for $MgO$-$SiO_2$-$H_2O$.

The aluminum oxide content is occuring in the Type B cement in Leka tillite. Similarly, the ratios between the three oxides $MgO$-$SiO_2$-$Al_2O_3$ for the cement are displayed in table 4.5 (c). The average ratio for $MgO$-$SiO_2$-$Al_2O_3$ of Type B is 1 : 0.43 : 0.14.

**Table 4.5 The ratio between dominant oxide components in Leka cement**

(a)$MgO$-$SiO_2$-$H_2O$ ratios in Type A from Leka

| **Origin&Type** | **WDS analysis point** | **Mole ratio** |
|---|---|---|
| | | **$MgO : SiO_2 : H_2O$** |
| **Type A of Leka cement** | **9** | 1: 3.29: 11.48 |
| | **10** | 1: 1.49: 4.53 |
| | **11** | 1: 2.02: 7.45 |
| | **12** | 1: 2.3: 7.1 |
| | **13** | 1: 3: 10.76 |
| | **14** | 1: 1.37: 3.81 |
| | **18** | 1 : 1.19 : 4.14 |
| | **19** | 1 : 0.78 : 1.4 |
| | **21** | 1: 0.55: 1.67 |
| | **47** | 1: 1.02: 1.42 |
| | **48** | 1 : 0.92 : 1.48 |

(b)MgO-$SiO_2$-$H_2O$ ratios in Type B from Leka

| Origin&Type | WDS analysis point | Mole ratio |
|---|---|---|
| | | **MgO: $SiO_2$: $H_2O$** |
| **Type B of Leka cement** | 1 | 1: 0.62: 3.39 |
| | 4 | 1: 0.14: 2.2 |
| | 6 | 1: 0.16: 2.46 |
| | 7 | 1: 0.17: 2.47 |
| | 22 | 1: 0.61: 1.28 |
| | 30 | 1: 0.21: 2.52 |
| | 33 | 1: 0.3: 1.69 |
| | 37 | 1: 0.81: 1.34 |
| | 38 | 1: 0.2: 1.47 |
| | 40 | 1: 0.65: 1.5 |
| | 42 | 1 : 0.79 : 1.29 |
| | 44 | 1: 0.6: 1.18 |
| | 51 | 1: 0.3: 2.45 |

(c)MgO-$SiO_2$-$Al_2O_3$ ratios in Type B of Leka cement

| Origin&Type | WDS analysis point | Mole ratio |
|---|---|---|
| | | **MgO: $SiO_2$: $Al_2O_3$** |
| **LekaType B** | 1 | 1: 0.62: 0.20 |
| | 4 | 1: 0.14: 0.20 |
| | 6 | 1: 0.16: 0.21 |
| | 7 | 1: 0.17: 0.21 |
| | 22 | 1: 0.61: 0.26 |
| | 30 | 1: 0.21: 0.14 |
| | 33 | 1: 0.3: 0.12 |

| | | |
|---|---|---|
| **LekaType B** | 37 | 1: 0.81: 0.01 |
| | 38 | 1: 0.2: 0.13 |
| | 40 | 1: 0.65: 0.04 |
| | 42 | 1 : 0.79 : 0.02 |
| | 44 | 1: 0.6: 0.09 |
| | 51 | 1: 0.3: 0.2 |

**c Composition of carbonate mineral in Leka tillite**

Five carbonate grains have been analysed using the WDS system, and the structural formulae for them are obtained in a similar way and shown in table 4.6. Calcite and magnesite are found. In addition, dolomitization in calcite is observed commonly, while the magnesite slightly contains Fe.

**Table 4.6 Structural formulae for the carbonate minerals**

| *WDS analysis number* | *Chemical formula* |
|---|---|
| 15 | $Ca_{0.98}Mg_{0.01}CO_3$ |
| 16 | $Mg_{1.02}Fe_{0.02}CO_3$ |
| 17 | $Ca_{0.99}Mg_{0.02}Mn_{0.01}C_{0.99}O_3$ |
| 26 | $Ca_{1.00}Mg_{0.01}CO_3$ |
| 41 | $Ca_{0.99}Mg_{0.01}CO_3$ |

## 4.4.5 The characteristion for mineral dissolution in Leka tillite

Under electron microprobe observation, almost each plagioclase grain demonstrates weathering phenomenon in various degrees. The initial shapes of some plagioclase grains are kept by those holes where the plagioclase grains are occurring. Using matlab's image processing functions and the software-Photoshop, it is possible to compare remain area of weathered plagioclase grain to its initial one by calculating out the ratio between them. The obtained results of describing the dissolving plagioclase grains are listed in the table 4.7, while the binary images for the initial and remain grain areas are shown respectively in the Fig 4.22. In addition, the quartz grains are processed in the same way, whose dissolution data are stored in table 4.8 and images shown in Fig 4.23.

**Table 4.7 The estimation results of the ratios for plagioclase grains in the Leka tillite**

| *Plagioclase grain shown in WDS number* | *Thin-section* | *Initial area(pixel number)* | | *Remain area(Pixel number)* | | *Ratio of dissolution,%* |
|---|---|---|---|---|---|---|
| | | *Pixel number* | *$um^2$* | *Pixel number* | *$um^2$* | |
| 2 | LK14-GC-1a | 197770 | 2981.5 | 143330 | 2160.8 | 37.5 |
| 5 | LK14-GC-1a | 136154 | 4089.3 | 63167 | 1897.2 | 53.6 |
| 8 | LK14-GC-1a | 36349 | 1105.3 | 3149.1 | 95.76 | 91.3 |
| 20 | LK14-GC-1b | 232330 | 3379.3 | 136880 | 1991 | 41.1 |
| 46 | LK14-GC-1b | 62704 | 5335.9 | 35976 | 3060.7 | 42.6 |
| 50 | LK14-GC-1a | 123030 | 17004 | 92683 | 12810 | 24.7 |

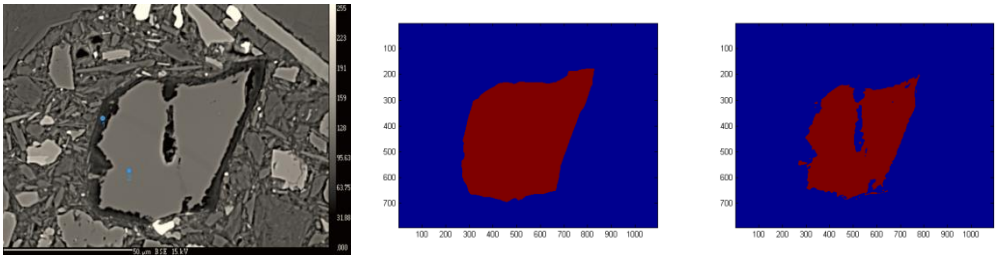

WDS 2

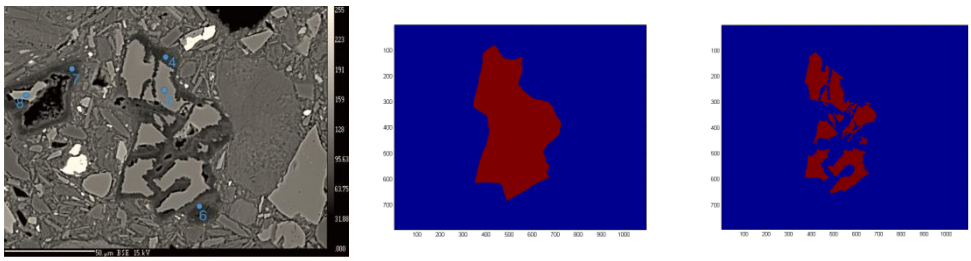

WDS 5

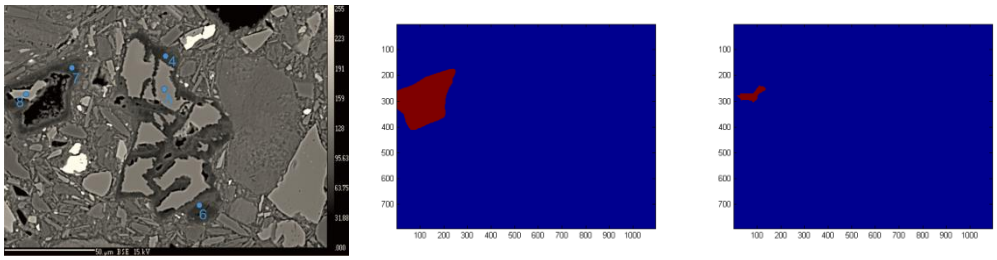

WDS 8

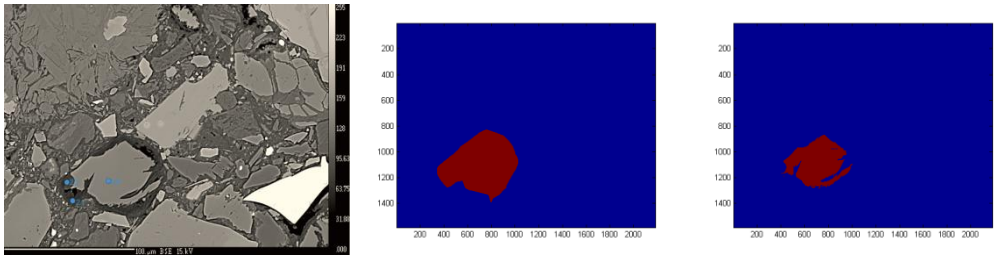

WDS 20

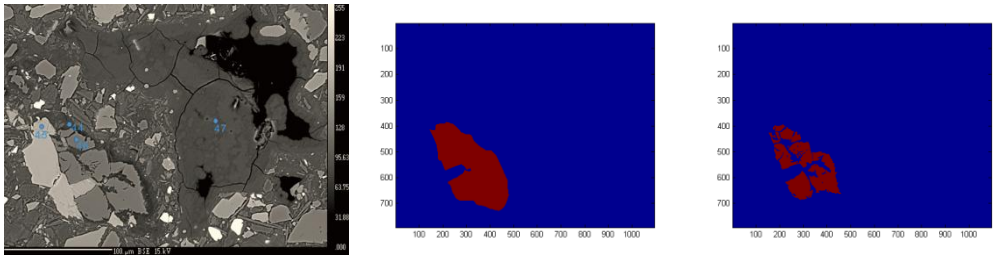

WDS 46

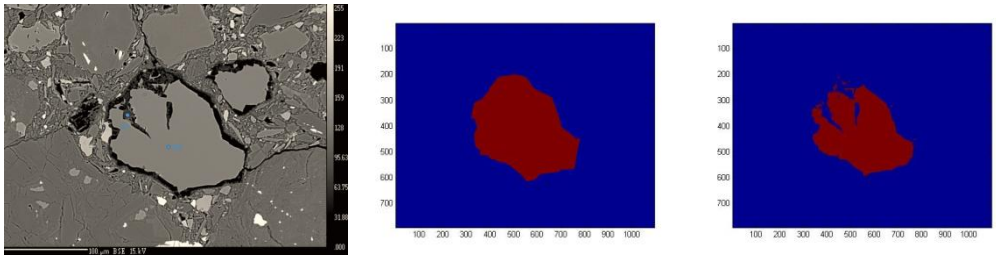

WDS 50

**Fig 4.22 Plagioclase Dissolution Estimation. Each plagioclase grain here is denoted by its WDS analysis number (left image is for the initial grain area and the right one is for the current grain area**

**Table 4.8 Estimation for the phenomenon of quartz dissolution**

| *Sequence number for quartz grain in this process* | *Thin-section* | *Initial area* | | *Remain area (pixel$^2$)* | | *Ratio of dissolution,%* |
|---|---|---|---|---|---|---|
| | | *Pixel number* | *um$^2$* | *Pixel number* | *um$^2$* | |
| I | LK14-GC-1a | 100204 | 23612 | 50785 | 11967 | 49.3 |
| II | LK14-GC-1b | 122790 | 21040 | 48765 | 8395 | 60.1 |
| III | LK14-GC-1b | 148933 | 19215 | 47391 | 6114 | 68.2 |

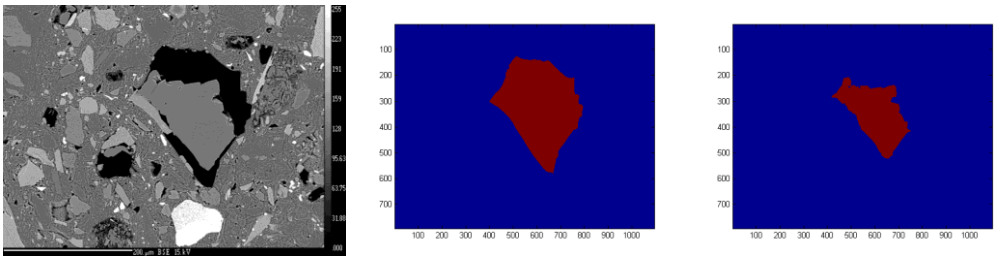

(I)

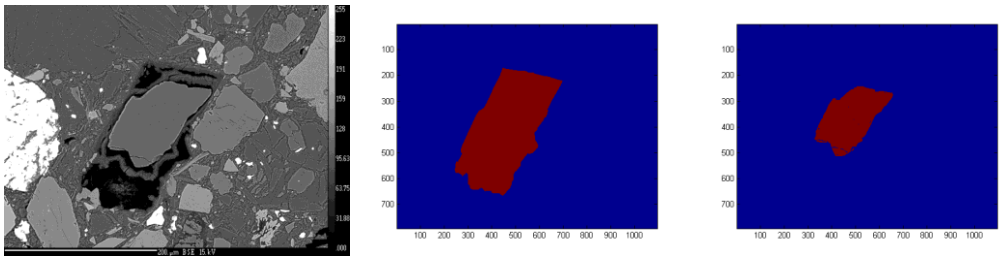

(II)

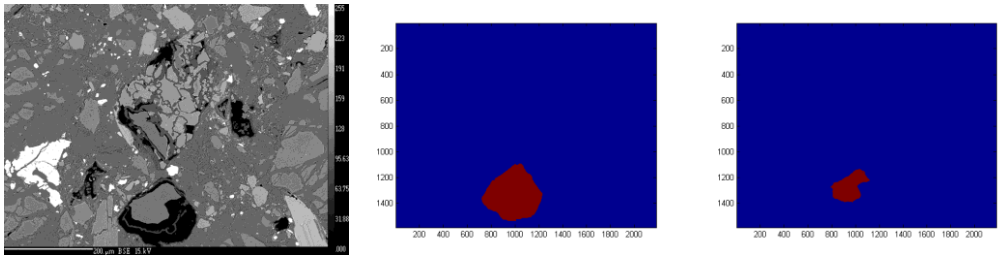

(III)

**Fig 4.23 Estimation for quartz dissolution (BSE image, Initial area and remain area)**

## 4.4.6 XRD results for the powdery samples from the Leka tillite

Sample WP-2014 of the white material on the fragment's surface is checked by XRD. The result about mineral phases detected in the specimen can be found in Fig 4.24 below. Within the specimen of the white material, two phases of dypingite and antigorite are found. Moreover, the main phase dypingite is a kind of hydrated magnesium carbonate $Mg_5(CO_3)_4(OH)_2{\cdot}5H_2O$, and the antigorite is a type of serpentine with chemical formula $Mg_3(Si_2O_5)(OH)_4$.

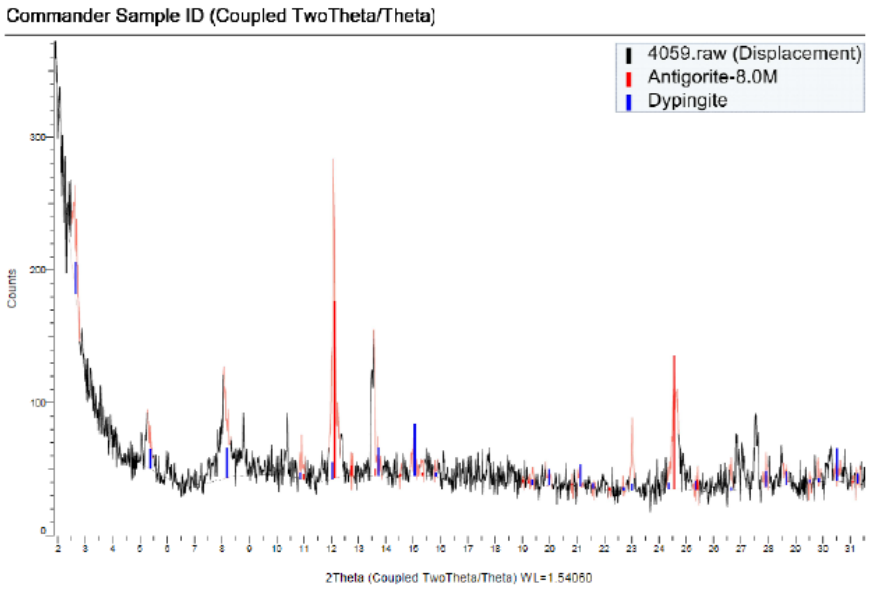


**Fig 4.24 XRD spectrum for the specimen WP-14 (white material on ultramafic fragment)**

### 4.4.7 Summuary for the observations and analysis results of Leka tillite

Leka tillite mainly consists of ultramafic fragments with some other minerals, such as quartz and feldspar. The shape of the mineral grains or lithic fragments in Leka tillite is usually from angular to sub-angular. Quartz and feldspar are the most commonly observed minerals to be dissolved in different extents. Furthermore, andesine and albite are the most popular feldspar members. The average dissolution extent of quartz grain is 59.2%, while it is 48.5% for dissolved plagioclase grains. This is not consistent with the common sense that quartz usually is a stable mineral. Carbonate minerals are secondary minerals and grow near the corroded quartz grains. The carbonates are mainly calcite and magnesite, which can be with minor contents of Fe or Mn, and dypingite (a kind of hydrated magnesium carbonate and identified by XRD) is found on the ultramafic fragments of the tillite. The cement in Leka tillite is identified as a kind of magnesium silicate hydrate. Moreover, the composition of cement in the tillite is apparently influenced by local dissolved minerals. Thus the cement usually contains some other elements, such as Al, Fe, Ca, Mn, Ni, Na,K. The Leka cement is classified as two main types-Type A and Type B. The Type A has the average ratio for $MgO$-$SiO_2$-$Al_2O_3$-$H_2O$ is 1 : 1.63 : 0.00 : 5.02; the ratio in Type B cement is 1 : 0.43 : 0.14 : 1.94. The atomic number for each of the other elements mentioned earlier is always not more than 0.03 in corresponding chemical formula of cement when normalized to 8 oxygens. Cement fills porous spaces resulted from other mineral's dissolution. Consequetly, it can suppress the growth of porosity in the tillite.

## 4.5 Petrography and mineral chemistry of the tillite from Feragen

### 4.5.1 Petrography

Dissolution and alteration of quartz grains are also common in the Feragen tillite. As shown in Fig 4.25 (a) the quartz grain has been strongly fragmented and the fragments are coated with cement. In addition, quartz grains show optical characteristic

of undulose extinction. This indicates that those quartz grains have been strained. There are two of such quartz grains illustrated in Fig 4.25 (b), which is taken using crossed nicol. The strainining process of quartz might be during the cementation of tillite as the overlying glacier pressured the tillite in the latest glaciation. The cement in the Feragen tillite has a similar EDS spectrum of the cement found at Leka tillite, where Si, Mg and O are the three dominant peaks in the spectrum. In addition, the tillite at Feragen is coated by Mg-carbonate with a desert-rose texture, displayed in Fig 4.26. The discovered Mg-carbonate using SEM is consistent with the field observation for the shaft walls covered by white magnesium carbonates. The texture of dypingite is similar as that desert-rose. Consequently, the Mg-carbonate is probably a kind of hydrated magnesium carbonate.

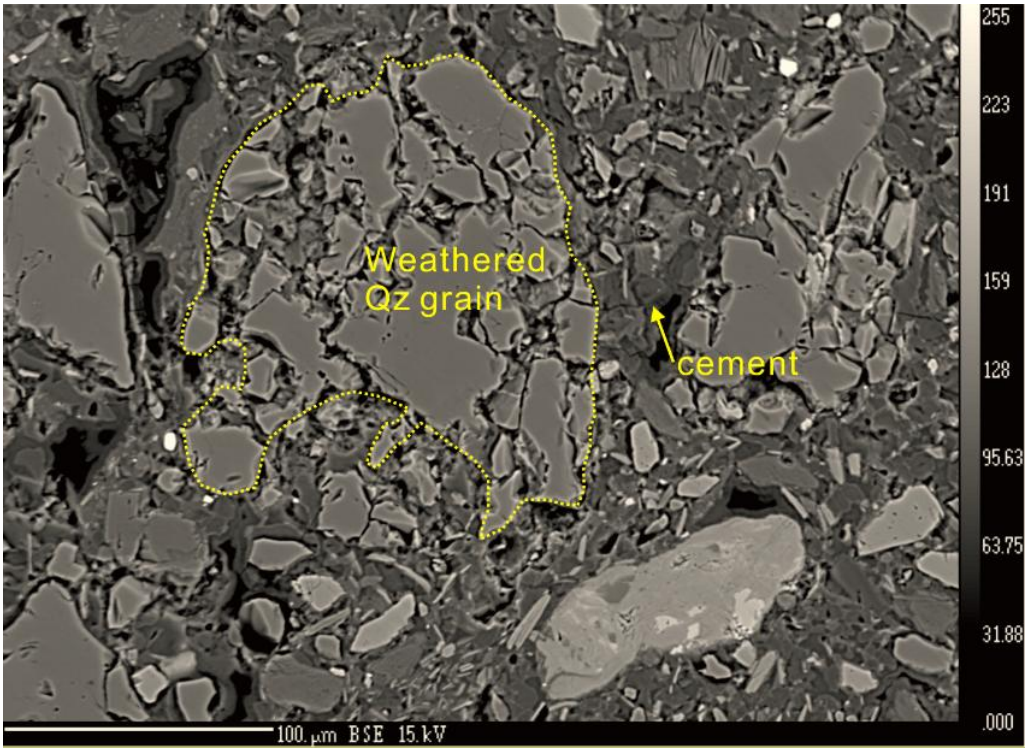


(a)Heavily dissolved quartz grain

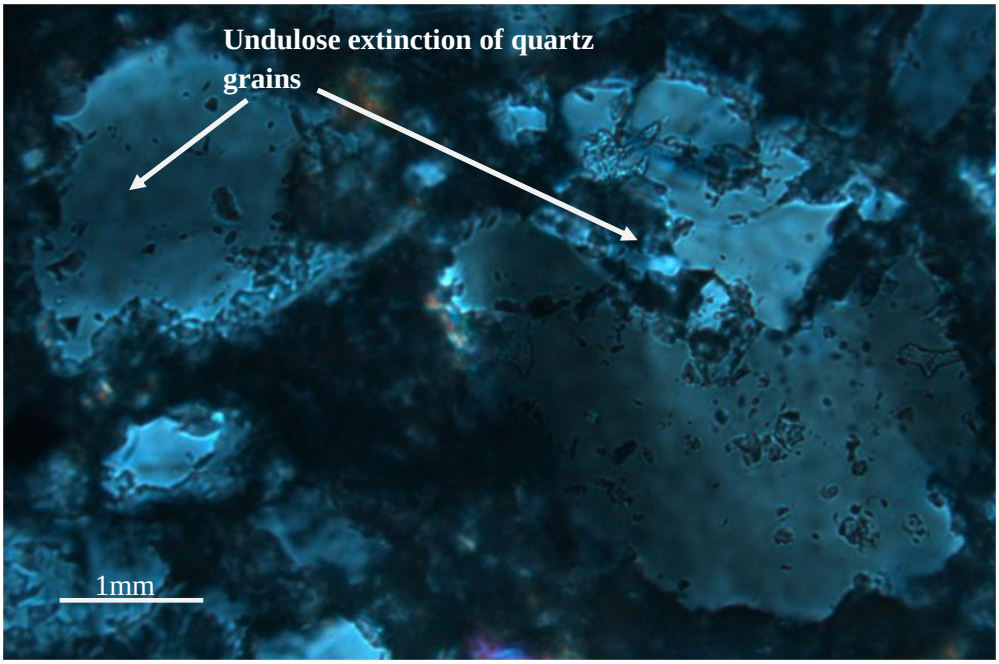


(b)Undulose extinction of quartz grain, taken with crossed nicol

**Fig 4.25 Photomicrograph showing undulose extinction of a partly dissolved and fragmented quartz grain , modified from Li et al., (2013)**

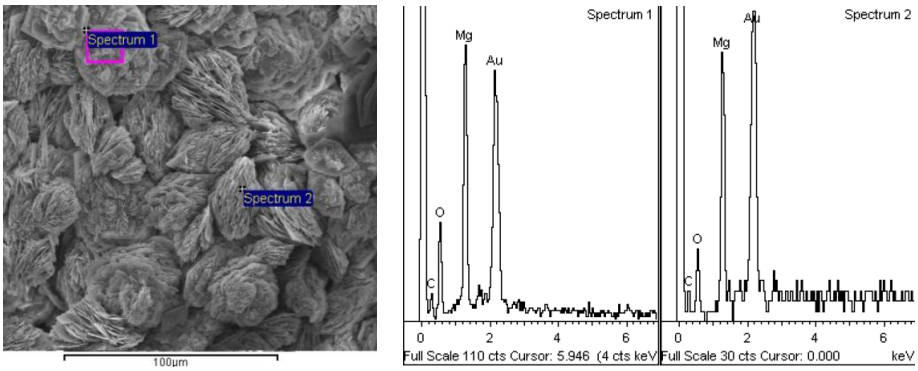


**Fig 4.26 The SE image for the magnesium carbonate hydrate with its EDS spectra**(Li et al., 2013)

The serpentinization on ultramafic mineral fragment is widely seen in Feragen tillite. The weathering effects on these minerals are able to be found as well in addition to serpentinization, with some analysis instruments. For example, both of a serpentinized mesh-texture olivine grain and a smaller pyroaurite (within the olivine grain) resulted from weathering can be seen in Fig 4.27 (a).

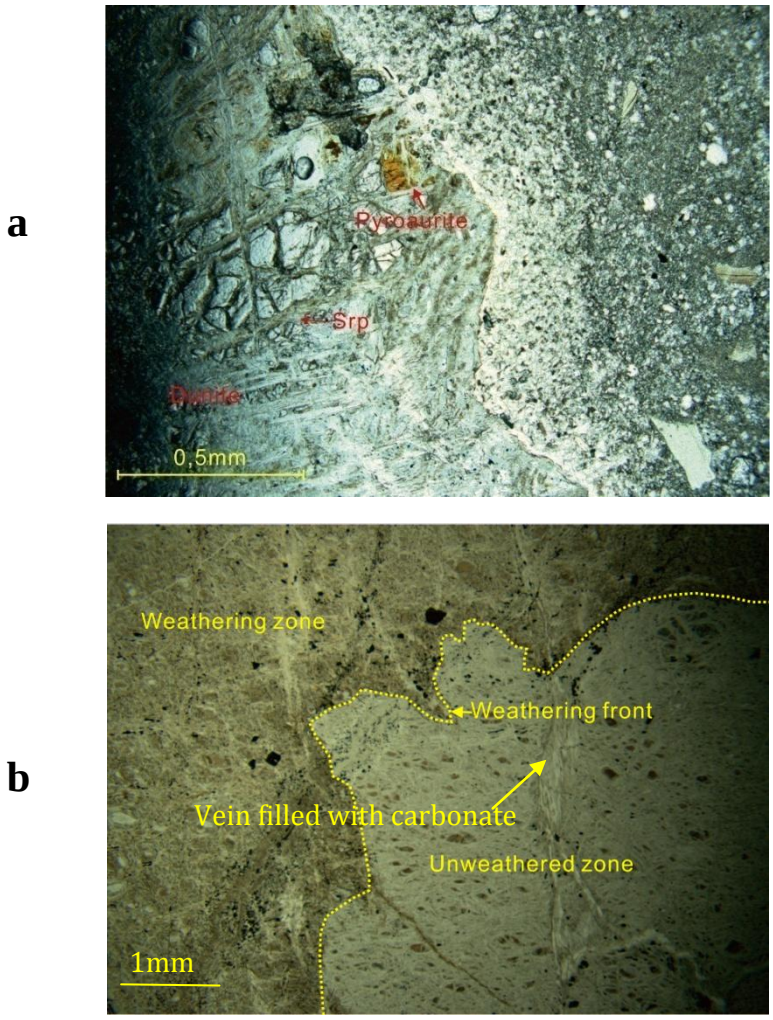


**Fig 4.27 Weathering front in serpentinized dunite fragment in tillite from Feragen modified from Li et al.,(2013)**

Additionally, observations of Fig 4.27 (b) indicate a wave shape weathering front in the serpentinized ultramafic mineral grain. This indicates, how the weathering process attacks the mineral grains of the Feragen tillite. It prefers to penetrate the grain along the crack formed before, and here the vein is filled with carbonate mineral. Furthermore, the weathering front divides the weathering and unweathered zones clearly. The weathering process was not easy to happen when the bedrock of the tillite was isolated from air and fluid by ice in the glaciation. Therefore, the weathering process probably started after the glaciation and during the cementation. Usually, the weathering zone has a lower porosity than the unweathered zone, such as the tight unweathered zone in Fig 4.28. The increase of porosity in weathering zone is due to that brucite has been dissolved to result in new porous space. Brucite (indicated by white arrow in fig 4.28) can be found between

fragments in unweathered zone, while much more porous space ( dark area and indicated in Fig 4.28) appearing between fragments are observed in weathering zone.

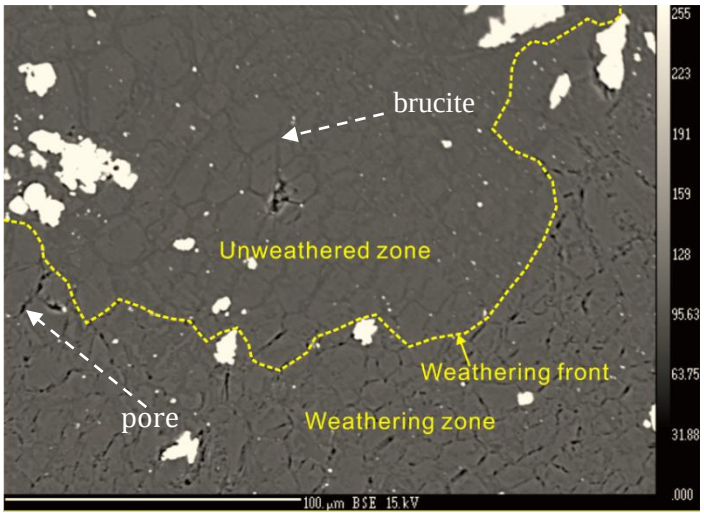


**Fig 4.28 The porosity difference between the weathering and unweathered zones in the Feragen tillite, modified from Li et al.,(2013)**

Fig 4.29 (a) shows a relatively smooth weathering front. In addition, on Fig 4.29(a), the WDS analysis, performed on the weathered and unweathered zones is indicated by the two yellow circles. Details of the unweathered and weathered brucite is displayed in Fig 4.29 (b) and (c). The unaltered and bright brucite is found within the unweathered zone in a serpentine grain, and another brucite observed to be weathered has become porous (Fig 4.29(c)). The differences of the chemical composition analysis between the fresh and weathered brucites are indicated in the table 5 in Appendix A for the minerals from Feragen tillite. In the table, the $H_2O$ molecular content apparently increases from the fresh brucite to the weathered one.

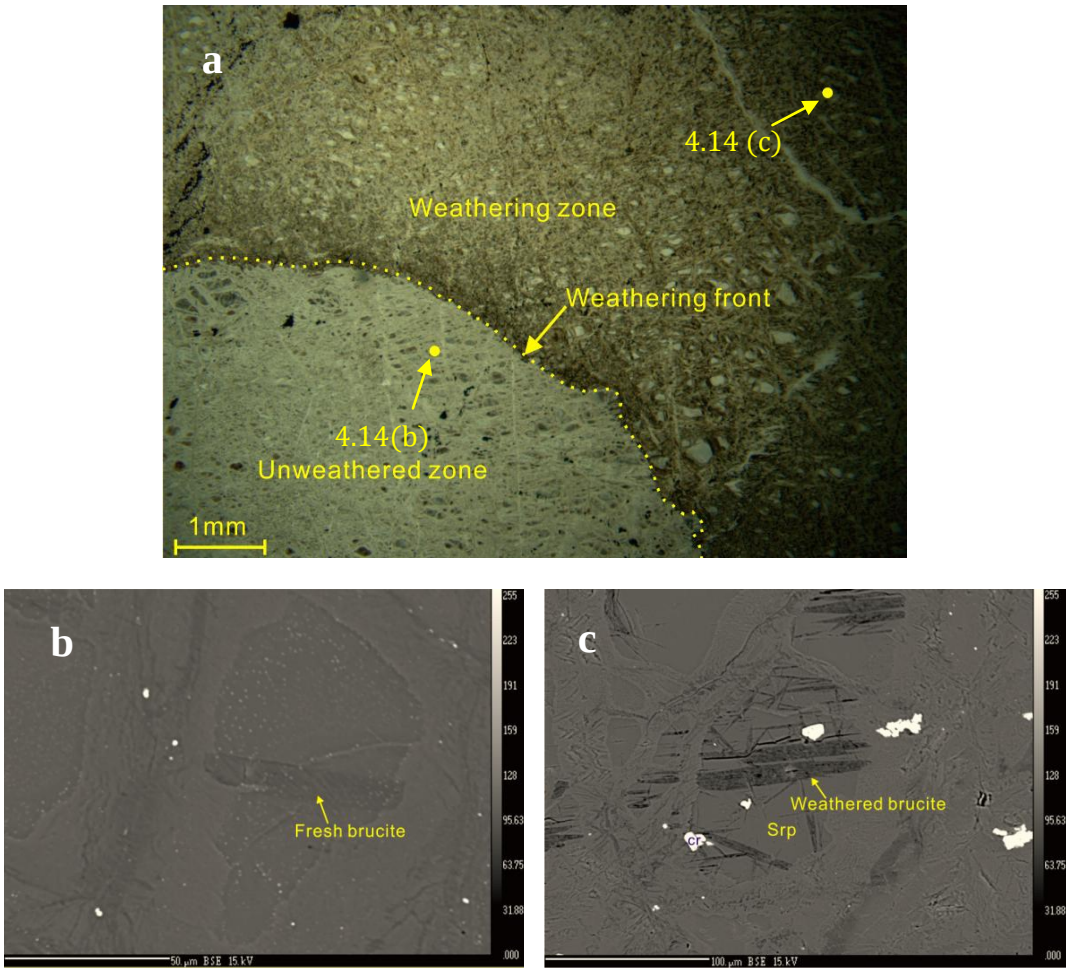


**Fig 4.29 (a) A smooth front is dividing the weathered and unweathering zones. (b) & (c)unaltered and weathered brucite, modified from Li et al., (2013)**

Locally brucite is found as separate grains in the tillite and is then coated by cement (Fig 4.30). For instance, the brucite grain contacted with the serpentine at both its left and right sides is covered with the cement on its up and bottom sides in the Fig 4.30. The brucite in Fig 4.30 shows a prominent cleavage and is surrounded by cement where the Si peak is higher than the Mg-peak. The spectra 5, 6 and 7 are the same and represent the serpentine near the brucite, the spectrum 1 for the brucite has both of high Mg and Fe peaks. This is a ferroan brucite that has changed composition during weathering.

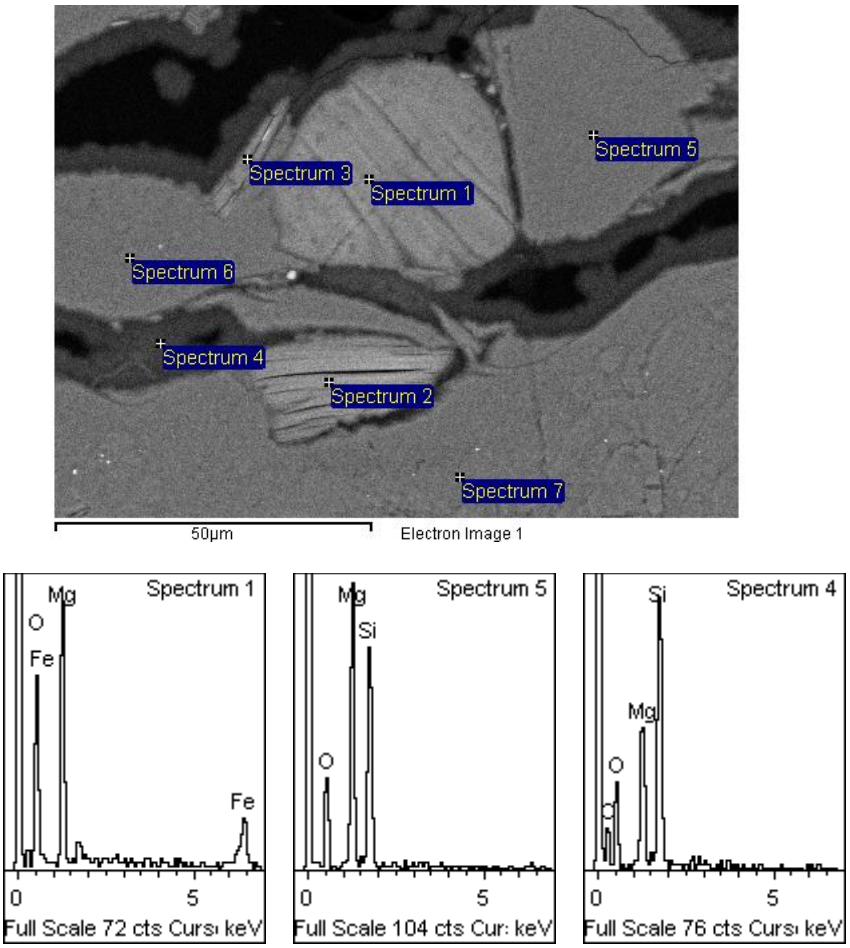


**Fig 4.30 EDS spectra of 1) ferroan brucite 5) serpentine and 4) cement**

## 4.5.2 The mineral chemistry in Feragen tillite

In addition to the qualitative and semi-quantitative geochemical analysis, the quantitative WDS analysis was also performed on minerals of the Feragen tillite. The WDS data for the Feragen tillite are stored in the tables 4&5 in the Appendix A. Furthermore, the chemical formulae for these minerals or cement are calculated on their WDS data and the resulted formulae are listed in the table 4.9 (a), (b) and (c) below.

**Table 4.9 The structural formulae for the minerals and cement in the Feragen tillite**
**(a) K-feldspar, Serpentine and Olivine**

| *Mineral name* | *Data No.* | *Chemical formula* |
|---|---|---|
| K-feldspar | 7-5/1 | $K_{0.92}Na_{0.04}Mg_{0.07}Al_{0.98}Si_{3.00}O_8$ |
| Serpentine | 7-6/1 | $Mg_{2.86}Fe_{0.08}Si_{2.06}O_{5.12}(OH)_{3.88}$ |
| | 7-11/1 | $Mg_{2.85}Fe_{0.08}Si_{2.06}O_{5.10}(OH)_{3.90}$ |
| | 7-13/1 | $Mg_{2.90}Fe_{0.07}Ni_{0.01}Si_{2.01}O_{4.99}(OH)_{4.01}$ |

| | | |
|---|---|---|
| Olivine | 7-14/1 | $Mg_{1.86}Fe_{0.14}Ni_{0.01}Si_{1.00}O_4$ |
| | 7-17/1 | $Mg_{1.86}Fe_{0.15}Ni_{0.01}Si_{0.99}O_4$ |
| | 9-19/1 | $Mg_{1.78}Fe_{0.11}Ni_{0.01}Si_{1.09}O_{4.08}$ |

**(b) Brucite and Quartz**

| *Mineral name* | *Data No.* | *Sub-class* | *Chemical formula* |
|---|---|---|---|
| Quartz | 7-3/1 | | $Si_{1.00}O_2$ |
| | 7-12/1 | | $Si_{0.97}Mg_{0.03}O_2$ |
| Brucite | 7-7/1 | Fresh | $Mg_{0.91}Fe_{0.09}(OH)_2$ |
| | 7-8/1 | | $Mg_{0.92}Fe_{0.07}(OH)_2$ |
| | 7-9/1 | Weathered | $Mg_{0.74}Fe_{0.20}Ni_{0.04}Si_{0.01}(OH)_2$ |
| | 7-10/1 | | $Mg_{0.72}Fe_{0.21}Si_{0.01}(OH)_2$ |
| | 7-16/1 | | $Mg_{0.73}Fe_{0.18}Ni_{0.01}Si_{0.07}(OH)_2$ |
| | 7-18/1 | | $Mg_{0.73}Fe_{0.18}Mn_{0.02}Ni_{0.01}Si_{0.06}(OH)_2$ |
| | 9-20/1 | | $Mg_{0.71}Fe_{0.19}Ni_{0.02}Mn_{0.01}Si_{0.07}(OH)_2$ |

**(c) cement**

| *Material name* | *Data No.* | *Chemical formula* |
|---|---|---|
| cement | F1 | $Mg_{1.64}Ca_{0.01}K_{0.04}Fe_{0.01}Al_{0.15}Si_{2.18}O_{6.27}(H_2O)_{1.73}$ |
| | F2 | $Mg_{1.56}Fe_{0.01}Al_{0.03}Si_{2.24}O_{6.10}(H_2O)_{1.90}$ |
| | F3 | $Mg_{2.30}Fe_{0.01}Al_{0.01}Si_{1.69}O_{5.70}(H_2O)_{2.30}$ |
| | F4 | $Mg_{2.16}Si_{1.62}O_{5.42}(H_2O)_{2.58}$ |
| | F5 | $Mg_{2.22}Al_{0.04}Si_{1.65}O_{5.57}(H_2O)_{2.43}$ |
| | F6 | $Mg_{2.89}Fe_{0.01}Al_{0.02}Si_{2.12}O_{5.02}(H_2O)_{2.98}$ |
| | F7 | $Mg_{1.96}Si_{1.37}O_{4.7}(H_2O)_{3.30}$ |
| | F8 | $Mg_{2.27}Fe_{0.02}K_{0.01}Al_{0.06}Si_{1.70}O_{5.79}(H_2O)_{2.21}$ |
| | F9 | $Mg_{2.28}Ca_{0.01}Si_{1.80}O_{5.89}(H_2O)_{2.11}$ |
| | F10 | $Mg_{2.14}Fe_{0.01}Si_{1.73}O_{5.62}(H_2O)_{2.38}$ |
| | F11 | $Mg_{2.36}Si_{1.71}O_{5.78}(H_2O)_{2.22}$ |
| | F12 | $Mg_{1.86}Fe_{0.01}Ca_{0.01}Al_{0.02}Si_{1.85}O_{5.62}(H_2O)_{2.38}$ |
| | F13 | $Mg_{1.90}Fe_{0.01}Ca_{0.01}K_{0.02}Al_{0.07}Si_{1.95}O_{5.93}(H_2O)_{2.07}$ |
| | F14 | $Mg_{2.09}Fe_{0.03}Ca_{0.02}Si_{1.89}O_{5.93}(H_2O)_{2.07}$ |

Furthermore, the oxide ratios for the Feragen cement (refer to table 4.10) have an average value as 1 : 0.89 : 1.11 for MgO-$SiO_2$-$H_2O$. Besides, some analysis points of the Feragen cement display minor contents of aluminum oxide, where the average ratio between MgO-$SiO_2$-$Al_2O_3$ for Feragen cement is 1 : 0.89 : 0.01(their ratios for MgO-$SiO_2$-$Al_2O_3$ refering to Table 4.10 (b)).

**Table 4.10 The ratio between dominant oxide components in Feragen cement**

(a) $MgO$-$SiO_2$-$H_2O$ ratios in Feragen cement

| Origin | WDS analysis point | Mole ratio |
|---|---|---|
| | | **$MgO : SiO_2 : H_2O$** |
| **Feragen** | F1 | 1 : 1.33; 1.05 |
| | F2 | 1: 1.44 :1.22 |
| | F3 | 1 : 0.73 : 1 |
| | F4 | 1: 0.75 : 1.19 |
| | F5 | 1: 0.74 : 1.09 |
| | F6 | 1 : 0.73 : 1.03 |
| | F7 | 1 : 0.7 : 1.68 |
| | F8 | 1 : 0.75 : 0.97 |
| | F9 | 1 ; 0.79 : 0.93 |
| | F10 | 1:0.81:1.11 |
| | F11 | 1:0.72:0.94 |
| | F12 | 1 :0.99: 1.28 |
| | F13 | 1: 1.03 :1.09 |
| | F14 | 1 :0.9: 0.99 |

(b) $MgO$-$SiO_2$-$Al_2O_3$ molar ratios in Feragen cement

| Origin | WDS analysis point | Mole ratio |
|---|---|---|
| | | **$MgO : SiO_2 : Al_2O_3$** |
| | F1 | 1 : 1.33 :0.05 |
| | F2 | 1: 1.44 :0.01 |
| | F3 | 1 : 0.73 : 0.00 |
| | F4 | 1: 0.75 : 0.00 |
| | F5 | 1: 0.74 : 0.01 |
| | F6 | 1 : 0.73 : 0.00 |

| | | |
|---|---|---|
| **Feragen** | F7 | 1 : 0.7 : 0.00 |
| | F8 | 1 : 0.75 : 0.01 |
| | F9 | 1 : 0.79 : 0.00 |
| | F10 | 1: 0.81: 0.00 |
| | F11 | 1: 0.72: 0.00 |
| | F12 | 1 : 0.99 : 0.01 |
| | F13 | 1: 1.03 : 0.02 |
| | F14 | 1 : 0.9: 0.00 |

### 4.5.3 The summary for the results of Feragen tillite

Similarly, Feragen tillite is mainly made of ultramafic fragments consolidated by cement. Angular or sub-angular is the most commom shape of mineral grain or lithic fragment in the tillite. Quartz grain is found to be seriously dissolved. No plagioclase is found. K-feldspar is the only observed one of feldspar mineral within Feragen tillite. However, undulose extinction is observed on the quartz grains, which is not seen on those quartz grains from Leka tillite. This means that the quartz grains from Feragen have been deformed. There are some apparent weathering fronts within the weathering ultramafic mineral grains. Consequently, the ultramafic grains are divided into two different zones- weathering zone (outter part) and unweathered zone (core part). Brucite, which is a product of the serpentinization of ultramafic mineral, has been recognized. It shows distinct states within the two zones. The brucite grain locating in the weathering zone has been weathered as well, while it is fresher in the unweathered zone. Pyroaurite, whose chemical formula is $Mg_6Fe_2(CO_3)(OH)_{16} \cdot 4(H_2O)$, can be discovered at some place in the weathered and serpentinized ultramafic grain. Furthermore, it can be another evident for brucite weathering. In addition, the weathering of brucite can result in some porous spaces in the tillite. magnesium carbonate is the dominant carbonate mineral in the tillite, some of which demonstrate the desert-rose structure under the SEM observation. The cement in the Feragen tillite is

also magnesium silicate hydrate, Al can be usually found within Feragen cement. The average oxide ratio between MgO-$SiO_2$-$Al_2O_3$-$H_20$ is 1 : 0.89 : 0.01 : 1.11 for Feragen cement. Some other elements, such as Ca, Fe and K, are occasionally found in the cement.

## 4.6 Simulation in phreeqc

### 4.6.1 Weathering in the tillites

The report (Li et al., 2013) has properly modeled the weathering processes in the Feragen tillite. They compared 4 different reactant combinations by their simulating results. Those combinations with brucite in reactants can provide good predictions for the weathering under a constant atmospheric $CO_2$ level. In addition, based on the observations for the two tillites, the simulation for the thesis will employ the reactant combination: brucite + serpentine +olivine. Moreover, this reactant combination will be tested in different conditions to look further into the influencing factors on this weathering, such as temperature, atmospheric $CO_2$ content, the presence of anorthite as one equilibrium phase. And the corresponding resulted diagrams are demonstrated in the Fig 4.31 with their relevant descriptions.

The basic details for the 5 simulations are that the porosity of the rock is 30%, and the brucite content of the rock is 20% . The modeling conditions for the simulation **a** is as follow: (1) reactant ratio: the moles of olivine are only 1% of that of brucite, so is the serpentine; (2) the Mg : Fe = 9 : 1 in the brucite; (3) the partial pressure of $CO_2$ is -3.4 (current atmospheric $CO_2$ content = 400 ppm in volume) ; (4) the temperature is 273.1 K (close to 0 ℃). The equilibrium phases in the simulation **a** can be found in the code in the Appendix C. Furthermore, the simulation **b** is obtained by increase the ratio Mg : Fe in the simulation **a** from 9 : 1 to 1 : 1. The simulation **c** is got by changed the temperature in the simulation **a** from 273.1 K to 293 K. The simulation **d** has a much lower $CO_2$ level than **a**, which is about 10 ppm-the lowest recorded value for the atmospheric $CO_2$ level in the late Quaternary (Lüthi et al., 2008). As a result the $CO_2$ partial pressure is -5. In the simulation **e**, anorthite, which is not present in the simulation **a**, is added into the equilibrium phase block. The other information about **d** or **e** are the same as those in **a**.

In the simulation (a), which can be found in Fig 4.31, the whole reaction process can be divided into two periods. The first period is represented by the quartz dissolution,

while the second one starts after the quartz consumed up. The pH increases more to about 10.5 from around 9, magnesium carbonate starts to be formed and the consuming rate for $CO_2$ increases apparently in the second period.

However, when the Fe content increases in the reactant-brucite, such as in the simulation **b** where the Mg : Fe in brucite in changed to 1 : 1 from 9 : 1, the pH curve within **b** doesn't have two steps like in **a**. In fact, it actually goes up to the final value of around 10.5 constantly, and the number of quartz increases instead of being dissolved. Furthermore, there becomes no carbonate formed during the reactions even though $CO_2$ is still consumed. However, pyroaurite is formed more than that in the simulation **a**.

In the simulation **c**, it shows that increasing the temperature for the reactions is good for the $CO_2$ consuming, but the final value for pH becomes a little lower and the formation for talc becomes more slowly after consuming up the quartz.

The ultra low $CO_2$ content in the simulation **d** has no significant impact on the quartz dissolution and pH values. However, the albite, which is one of those equilibrium phases, is only dissolved slight compared with the situation of **a**.

The change behaviors for the weathering reactions become quite different when there is a presence of anorthite in the group of equilibrium phases, which is described in Fig 4.30 (e). Its pH value can reach about 12 finally, and dolomite formed instead of magnesite. Furthermore, the amount of quartz actually increases at first. This begins to drop when the pH increases to around a stable value of 11.5. However, anorthite and dolomite become relatively stable at the same time.

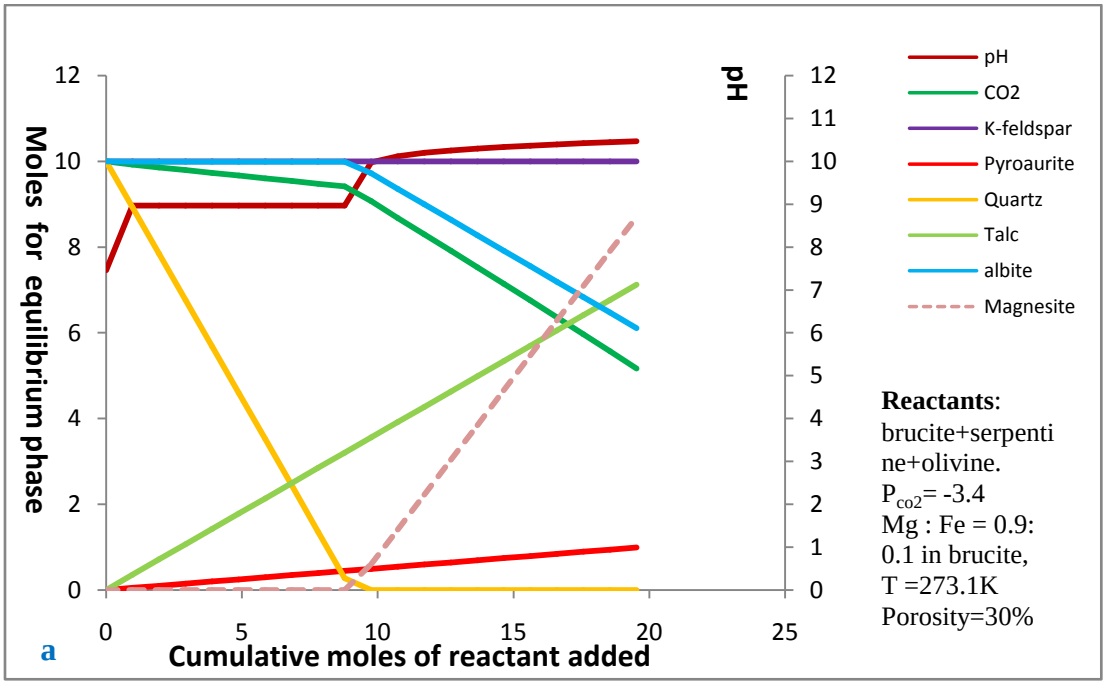
Moles for equilibrium phase
pH
Cumulative moles of reactant added
pH
CO2
K-feldspar
Pyroaurite
Quartz
Talc
albite
Magnesite
Reactants: brucite+serpentine+olivine.
$P_{co2}$= -3.4
Mg : Fe = 0.9: 0.1 in brucite,
T =273.1K
Porosity=30%
a

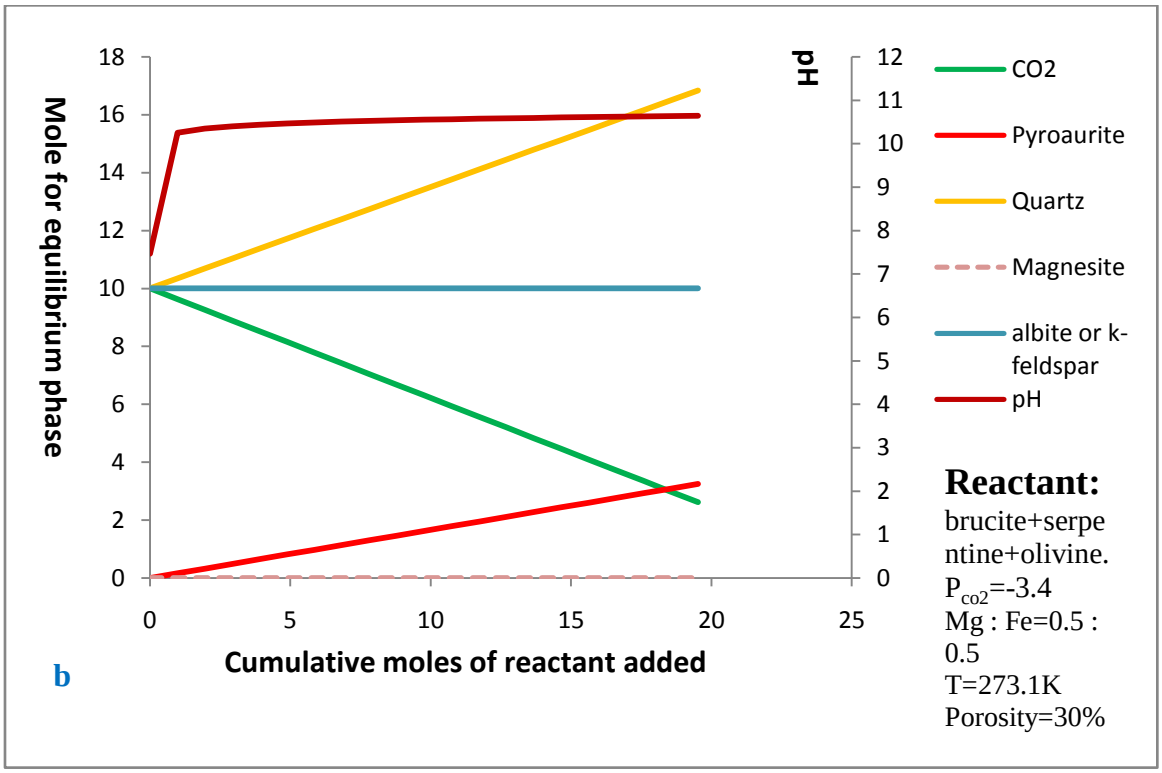
Mole for equilibrium phase
pH
Cumulative moles of reactant added
CO2
Pyroaurite
Quartz
Magnesite
albite or k-feldspar
pH
Reactant: brucite+serpentine+olivine.
$P_{co2}$=-3.4
Mg : Fe=0.5 : 0.5
T=273.1K
Porosity=30%
b

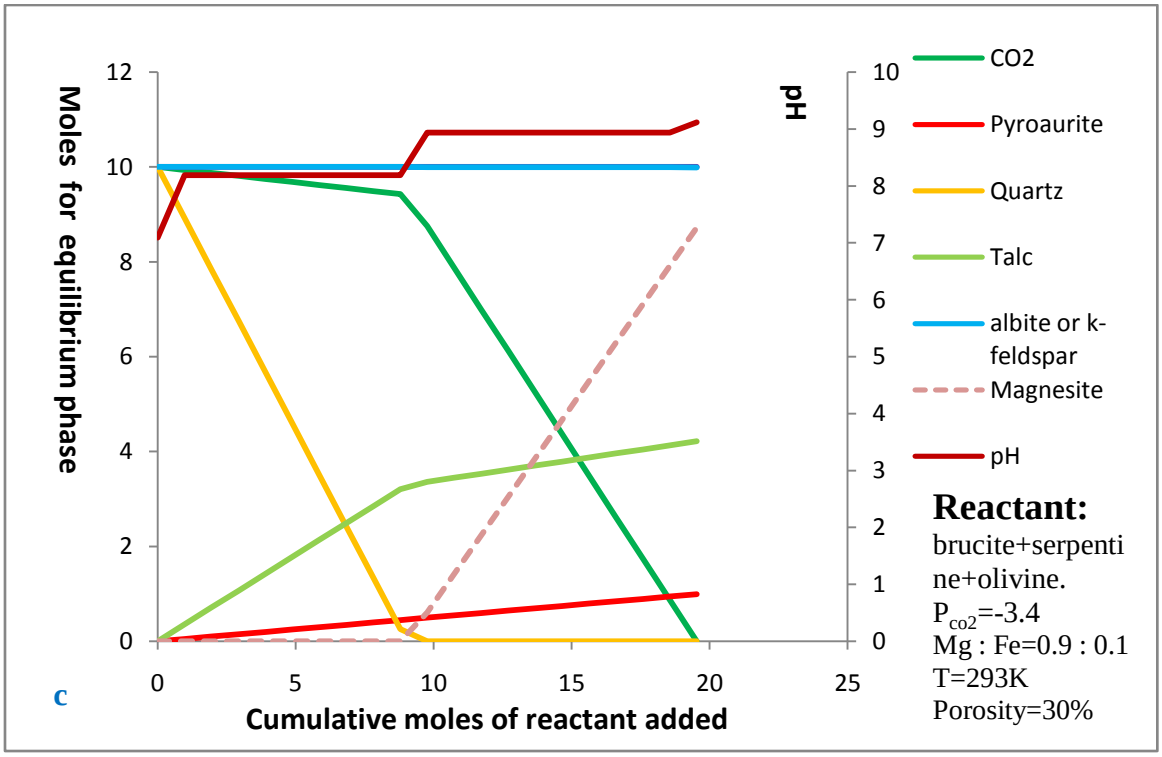
Moles for equilibrium phase
pH
Cumulative moles of reactant added
CO2
Pyroaurite
Quartz
Talc
albite or k-feldspar
Magnesite
pH
Reactant:
brucite+serpentine+olivine.
$P_{co2}$=-3.4
Mg : Fe=0.9 : 0.1
T=293K
Porosity=30%
c

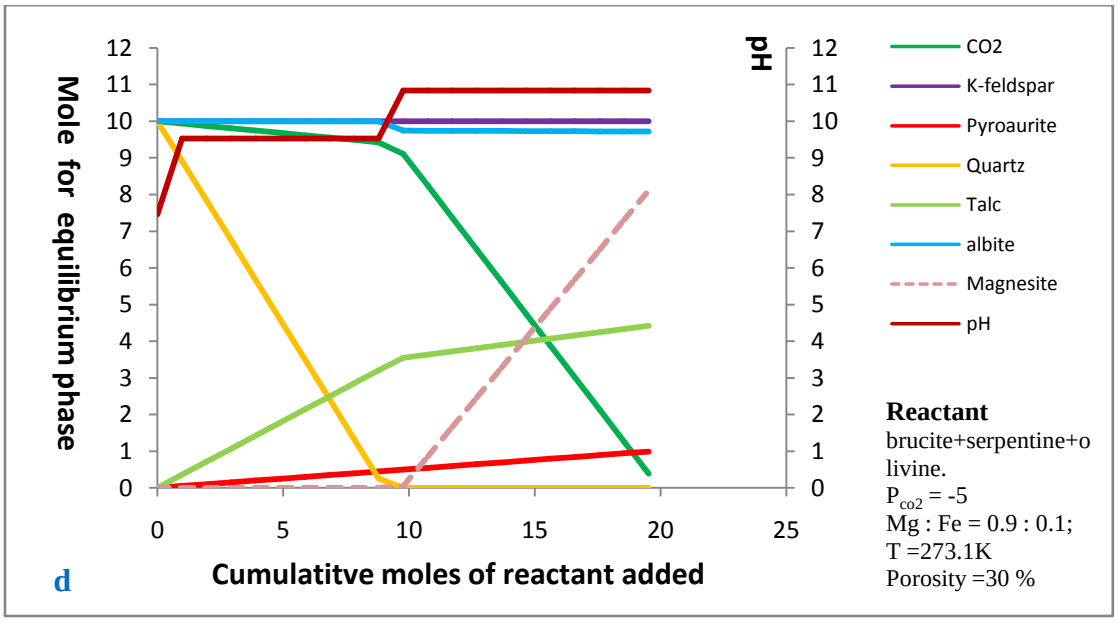
Mole for equilibrium phase
pH
Cumulativte moles of reactant added
CO2
K-feldspar
Pyroaurite
Quartz
Talc
albite
Magnesite
pH
Reactant
brucite+serpentine+olivine.
$P_{co2}$ = -5
Mg : Fe = 0.9 : 0.1;
T =273.1K
Porosity =30 %
d

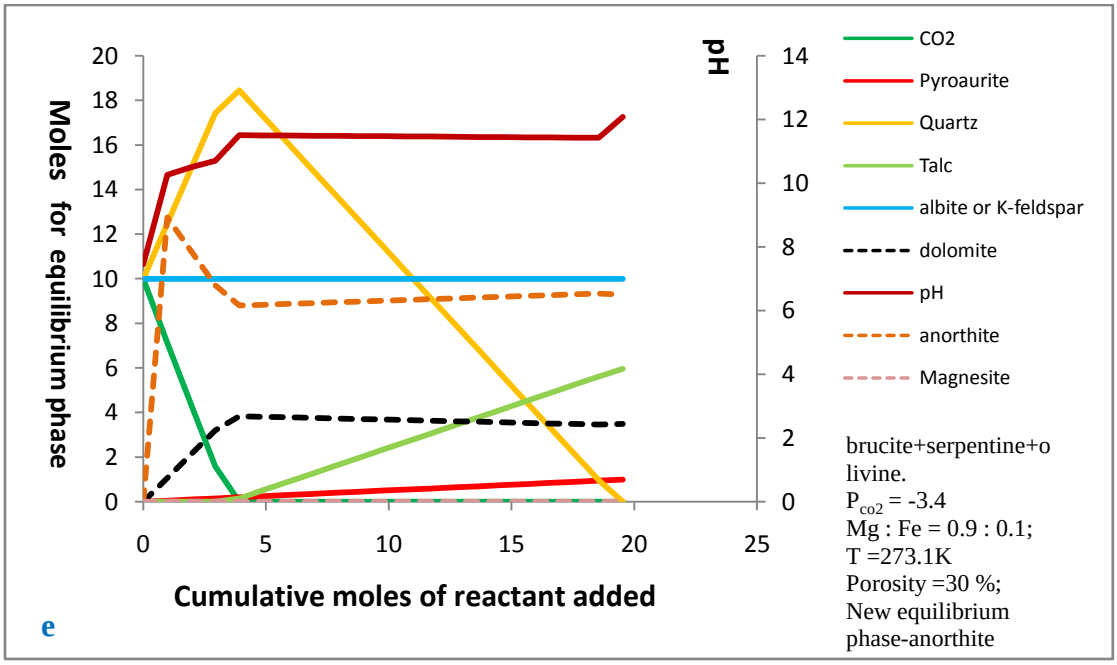


**Fig 4.31 The Phreeqc modeling results**

## 4.6.2 Summary for the PHREEQC simulation

1. The amount of quartz can increase instead of being dissolved when the Fe content is promoted to the same level as that of Mg in brucite. Higher Fe content in brucite is also favorable for $CO_2$ consumption, but it suppresses the formation of magnesite.

2. Higher temperature can apparently increase the consuming rate of $CO_2$. However, pH in solution is restrained slightly by higher temperature.

3. Lower atmospheric CO2 level will lead to a higher pH in solution.

4. The occurence of anorthite as equilibrium phase will not only accelerate the consuming rate of CO2, but also delay the generation of talc. In addition, dolomite is formed instead of magnesite, and quartz starts to be dissolved just after the CO2 is depleted in this case.

## 4.7 Quartz dissolution experiment results

The phenomenon of quartz dissolution has been observed in both cases. However, it is still unclear about that how fast it goes. Therefore, two rounds of experiments are performed in order to estimate the quartz dissolution rate in solution saturated with $Mg(OH)_2$. Before the second experiment is conducted, the quartz was immersed in a solution saturated with $Mg(OH)_2$ for one month at pH around 9.8 in the first round experiment. Nevertheless, the quartz surface did not show any detectable changes. Therefore the pH value needs to be increased by using sodium hydroxide to be possible for getting a detectable change in the short period of one month.

The mean height in Fig 4.32 is the mean height of the selected area (indicated by the rectangular) on the quartz surface relative to the surrounding epoxy surface. The height between the quartz and the surrounding epoxy of **SP4** decreases from about 35.8 um to around 1.5 um. **SP9'** s height decreases from 38 um to 21 um based on the resulted images (Fig 4.32) processed from matlab. Additionally, the processed images in Fig 4.32 demonstrate the two topography of specimen before and after experiment. The left image conveys the origin of the topography, and the right one represents the topography after the experiment. As each image's colorbar is not completely the same, so it is not correct to oberve the topography's change only by comparing the two images.

In addition, there are 8 measurements for pH value of the solution in the two sets respectively, using the electrical pH meter during the whole experiment period, and these pH measurements can be found in table 4.11.

The calculated dissolution rate of SP4 is $1.8 \times 10^{-12}$ mol/s, and the rate of SP9 is $4.6 \times 10^{-13}$ mol/s.

**Table 4.11 pH measurement for the solution in the quartz experiment**

| *Solution Identity* | *T* | *pH measurement* | | | | | | | |
|---|---|---|---|---|---|---|---|---|---|
| | | *1d* | *5d* | *9d* | *13d* | *17d* | *21d* | *25d* | *29d* |
| SP4 | 5 ℃ | 12.8 | 13.0 | 12.9 | 12.9 | 12.9 | 12.9 | 12.9 | 13.0 |
| SP9 | 20 ℃ | 13.0 | 13.1 | 13.0 | 13.0 | 13.1 | 13.1 | 13.0 | 13.1 |

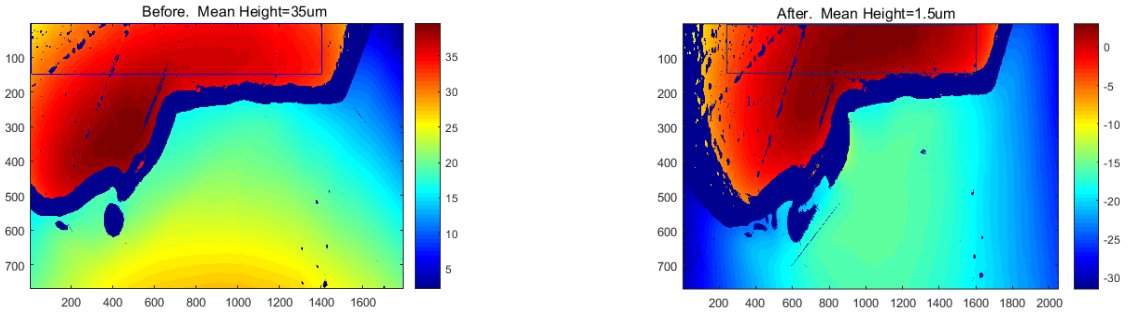


(a) The comparison between the origin specimen surface of **SP4** and the one after the experiment. (The size of rectangular is 5.5mm × 0.6mm)

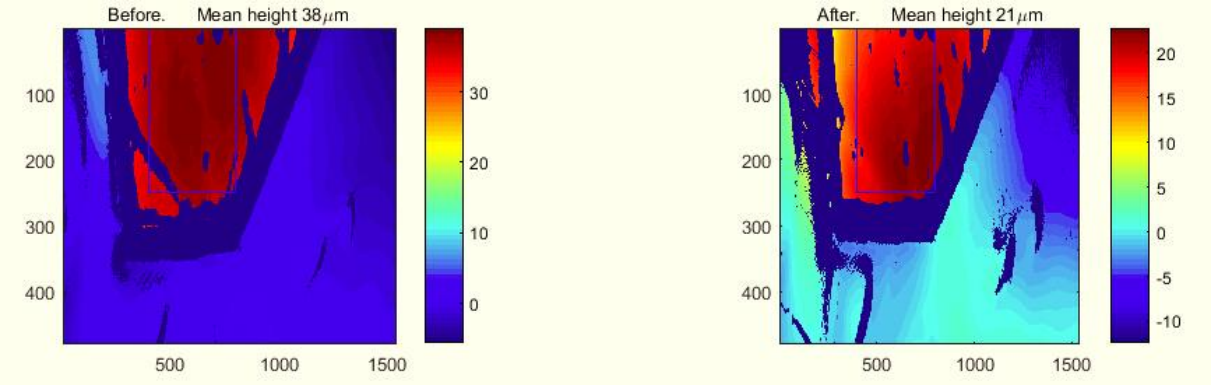


(b) The comparison between the orgin specimen surface of **SP9** and the one after the experiment (The size of rectangular is 1.6mm × 1.0mm)

**Fig 4.32 The change about the quartz surface change in the experiment (The right image is for the origin surface, and the left image is for the dicreased surface after the experiment).**

# Chapter 5 *Discussion*

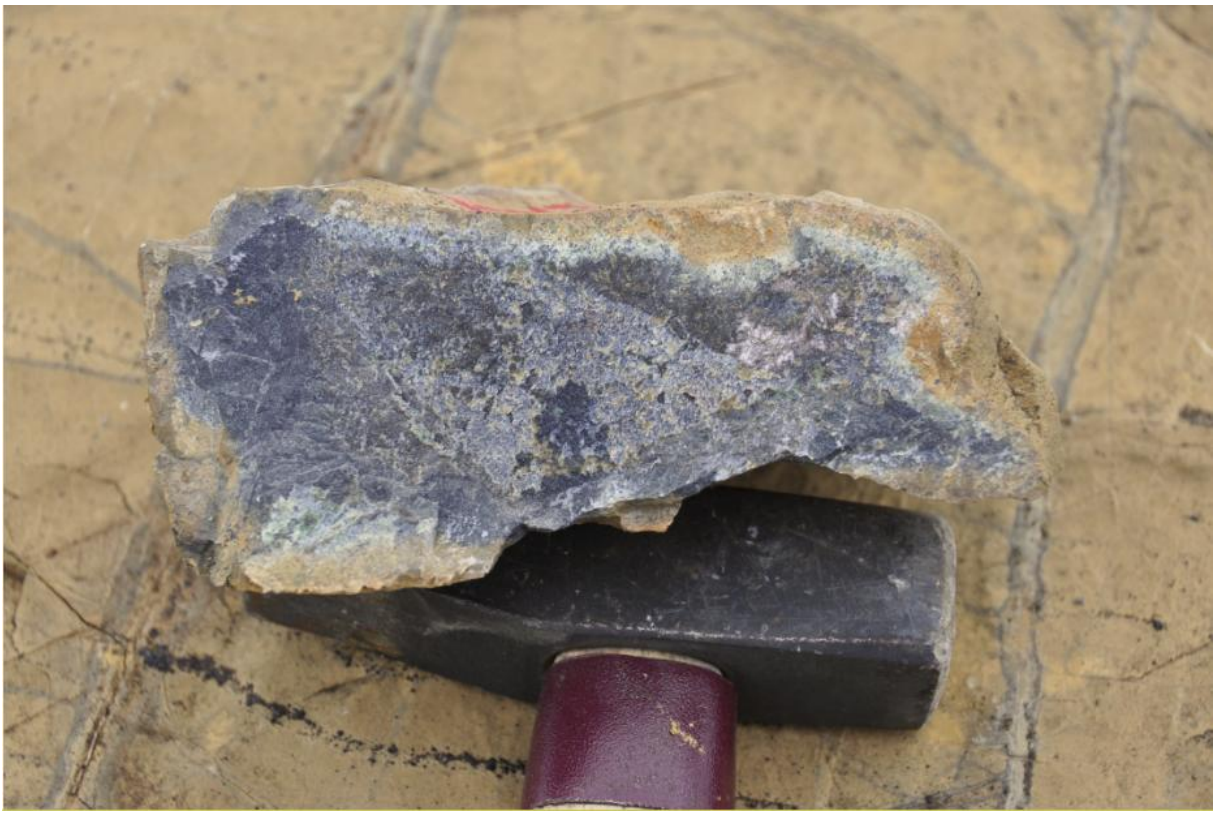

## 5.1 Mineral Dissolution

### 5.1.1 Dissolution of feldspar and quartz in Leka tillite

Usually the quartz should be much more resistant than feldspar to weathering, but the quartz grain appears to be observed to be dissolved more strongly than plagioclase grain in Leka tillite. For example, the average dissolution ratio of plagioclase is only 46.8% , while the mean dissolution ratio for the three quartz grains in Fig 4.23 is 59.2%. The uncommon phenomenon observed here indicates that the environment is more favorable to quartz dissolution in the tillite. In general, quartz will be dissolved in the environment with high pH. Moreover, the environment inside the tillite is likely to be basic.

### 5.1.2 Anorthite content influence on dissolution of plagioclase

Based on the data about plagioclase composition and dissolution in tables 4.2 and 4.7, the influence on the dissolution of plagioclase from its fraction of anorthite will be discussed. For instance, from points 46 to 8 in Fig 5.1, the dissolution content of plagioclase is considered to be related with anorthite content of plagioclase. Whereas the amount of dissolved feldspar increases with the anorthite content decreasing in the points from 50 to 46. However, there is a poorly quantified effect that the anorthite content in plagioclase is favorable for the dissolution rate of plagioclase(Palandri and Kharaka, 2004). Our observation is partly consistent with this trend. However, the data must be treated with care since we observe in 2-dimension while the grain is in 3-dimension. Point 8 could be an outlier due to 2D/3D problem. The anorthite contents for other points are almost on the same level, and then there is a statistical variation of +/- 20% in the measurements for dissolution extent of them. This could be an uncertainty for estimation on plagioclase dissolution. Therefore, the calculation for the plagioclase dissolution is probably not sufficient to explicitly explain what happened for plagioclase grain in reality.

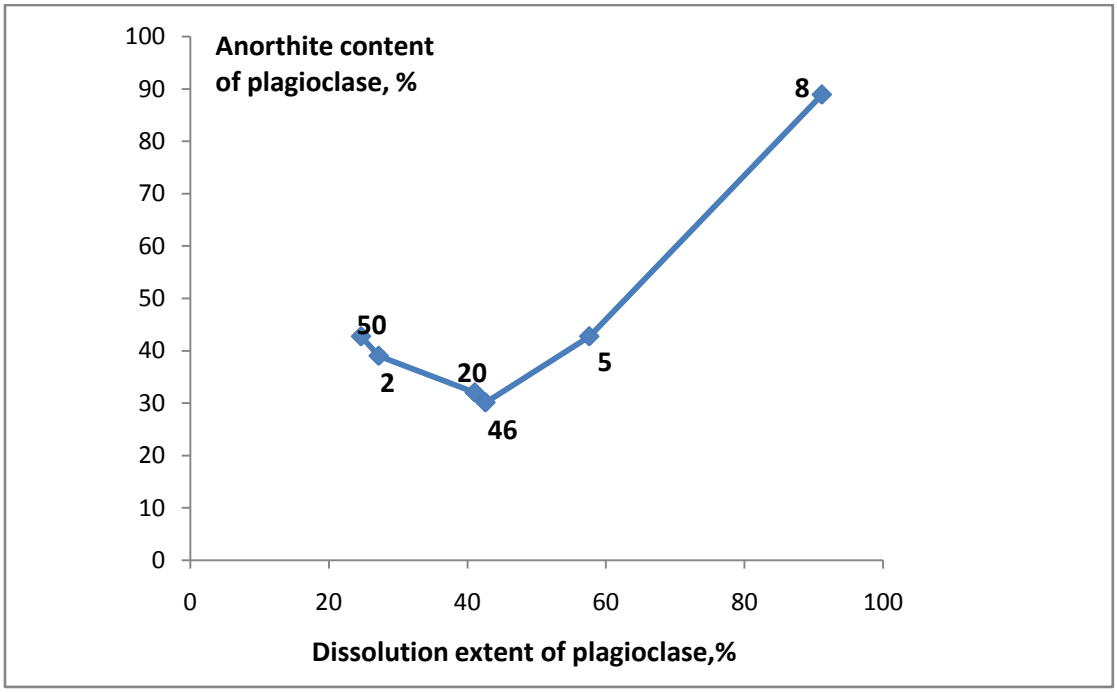


**Fig 5.1 Weathering content of plagioclase against its anorthite content**

## 5.1.3 Mineral dissolution influence on cement

The element mapping function of EMP provides an intuitive way to observe the weathering phenomenon in the tillite. Some minerals dissolutions will influence the composition of cement nearby, especially plagioclase, which can increase Al contents in the nearby cement. However, the cement near the plagioclase has a lower content of Si than those near quartz (indicated by an arrow in Fig 5.2). This means that quartz dissolution provides more Si to the formation of cement. Furthermore, Al is mainly found in those cements close to the corroded plagioclase grain(indicated in Fig 5.2). These situations are shown in the Al and Si mappings in the Fig 5.2. It is indicated that Leka cement can hav two Si sources: quartz and plagioclase. However, its Al source is only feldspar.

On the other hand, the Mg content in the cement is close to its background value. The weathering of ultramafic minerals is the dominant source of Mg for the cement and very common in the tillite. The released Mg can be transported to various positions through the porous system in the tillite by pore fluids, which makes the Mg distribution more homogeneous. As found in the Feragen tillite, brucite has been weathered in the

weathering zone within the partly weathered serpentinized ultramafic grain. It is known that the dissolution of brucite can provide $Mg^{2+}$ and $OH^-$ into the pore fluids. Subsequently, its dissolution can promote the pH of pore fluids.

Fe is rarely occuring in Leka cement (refer to Fe mapping in Fig 5.2). Forsterite is the dominant ultramafic mineral within Leka tillite, and Fayalite or pyroxene is not widely found. It can explain why Fe is not popular to be seen in the cement. Ca is only rich at some positions within the image of Ca mapping from Fig 5.2.

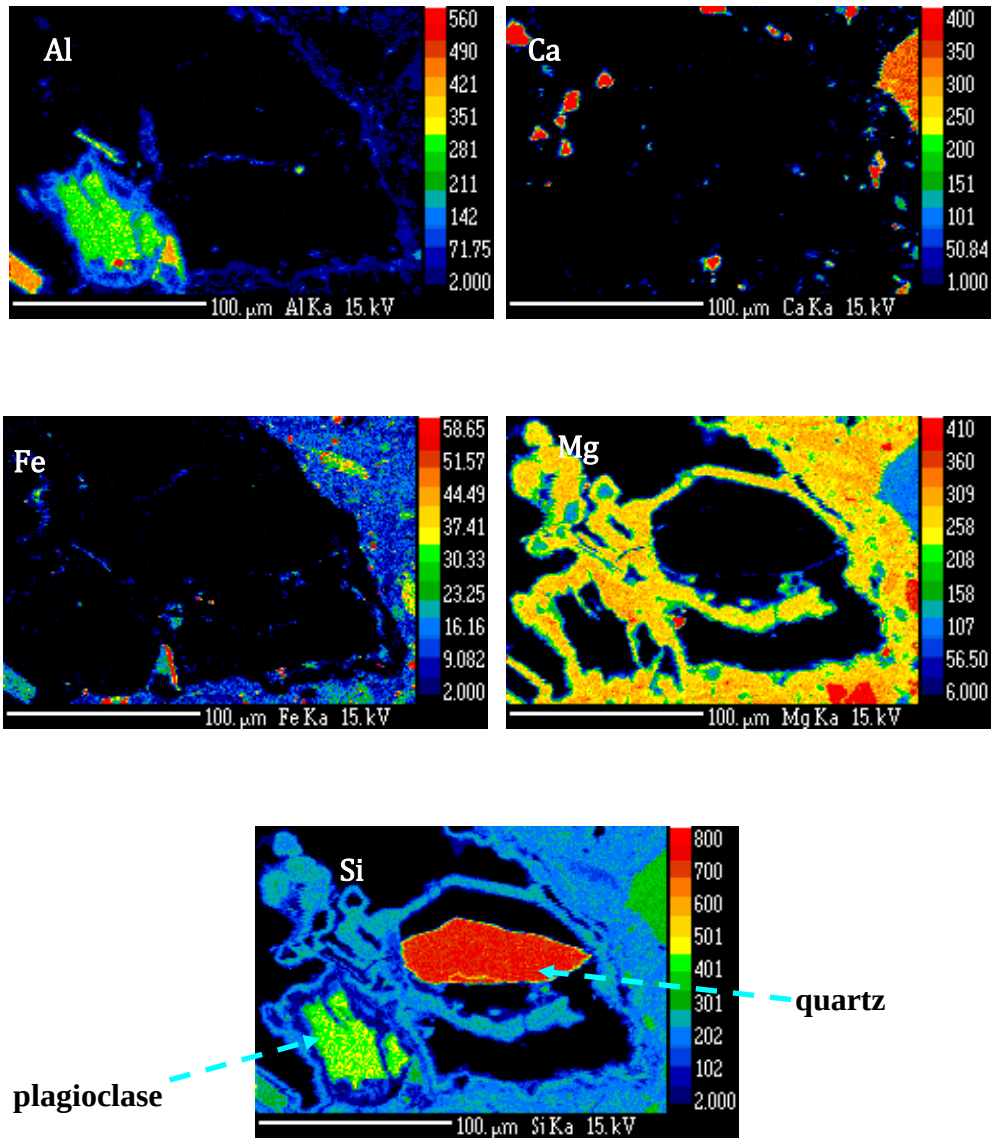


**Fig 5.2 Element mapping for 5 selected elements in one area within the Leka tillite**

## 5.2 Comparisons between the Leka tillite and the Feragen tillite:

### 5.2.1 Composition of cement in the two tillites

Based on the WDS analysis results for the cement in the Leka tillite, can be roughly classified as two different dominant types. The first type named as type A, has 3 main components that are MgO, $SiO_2$ and $H_2O$, while the other type B has 4 main components of MgO-$Al_2O_3$-$SiO_2$-$H_2O$..The number of type A cement is found in 11 different WDS analysis points, while type B is found in 13 WDS analysis positions. From quantitatively analysis about the cementing material in Feragen tillite (refer to Appendix A-table 4), the Feragen cement mainly contains MgO, $SiO_2$ and $H_2O$, and most of them have minor contents for $Al_2O_3$. The Feragen cement is similar to the type A cement in the Leka tillite on composition.

MgO, $SiO_2$, $H_2O$ and/or $Al_2O_3$ are the main components in the Leka cement and the Feragen cement. Thus, the characteristics of the mole ratios between these oxides are estimated out based on their WDS data. The ratio of MgO to $SiO_2$ in type A cement of the Leka tillite is from about 1 : 0.5 to 1 : 3.3. However, most of them are within the range of 1:1 to 1:3.3, while each result of ratio is obtained after normalize the value for MgO as 1. The ratios in type B are between 1 : 0.1 and 1 : 0.8. Whereas, there are 6 points in the 13 WDS analysis points for type B, which are between 1:0.6 and 1:0.8 and the other 7 ratios are between 1 : 0.1 and 1 : 0.3. For cementing material from Feragen, most of such ratios are between 1:0.7 and 1:0.8.

In addition, the mole ratio of $SiO_2$ : $H_2O$ in type A cement of Leka is around 1:3. Whereas, type B of Leka are quite dramatic, which are more than 1:5. The majority of type B has a larger mole fraction of $H_2O$ molecular, which implies that the hydration degrees of some type B cements are higher.

In the triangle diagram found in Fig 5.3 (a) of MgO-$SiO_2$-$H_2O$, it is plotted at each end member's weight fraction in the total of the three end members. The points representing the Feragen cement are plotted in a small area in Fig 5.3 (a), while those for type B of Leka cement have a scattered distribution in the diagram. Type A has an

intermediate distribution situation. On the diagram, the fraction of MgO is decreasing, the fraction of $SiO_2$ increasing and $H_2O$ fraction keeping appropriately in the same level from type B to type A.

In addition to the MgO-$SiO_2$-$H_2O$ diagram, the triangular diagram with MgO-$SiO_2$-$Al_2O_3$ as end members is also made. In the diagram of Fig 5.3 (b), the type A of Leka cement and the Feragen cement are on or near the side of the triangle opposite to the end member of $Al_2O_3$. This shows an extremely low or no content of aluminate. However, the type B of Leka cement certainly has fractions for aluminum oxide mostly ranging from 10% to 30% in the sum of MgO, $SiO_2$ and $Al_2O_3$ contents.

The details about molar ratios between MgO, $SiO_2$ and $Al_2O_3$ in all cementing materials are collected in the tables 4.5(c) and 4.10(b). For type B, the ratios between $SiO_2$ and $Al_2O_3$ have a very wide value range, which is from about 0.7 : 1 to about 340 : 1, and most of the mole ratios between MgO : $Al_2O_3$ are from 1: 0.1 to 1 : 0.2.

Ultramafic rock contains relatively high concentrations of Ni and Cr in the order of 2000-4000 ppm. Cement derived from ultrmafic rock may does harm to human health. Fortunatly, the contents of Cr and Ni in the cement from Feragen and Leka are low and in the order of hundreds of ppm.

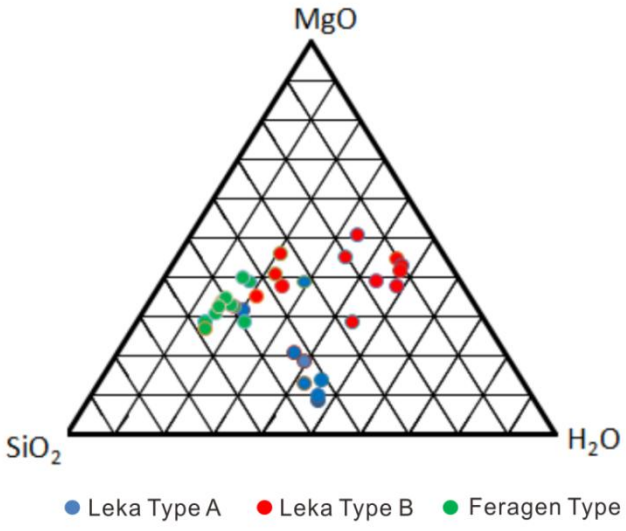


(a) MgO-$SiO_2$-$H_2O$ triangular diagram about cementing material from both of the Leka and Feragen tillites

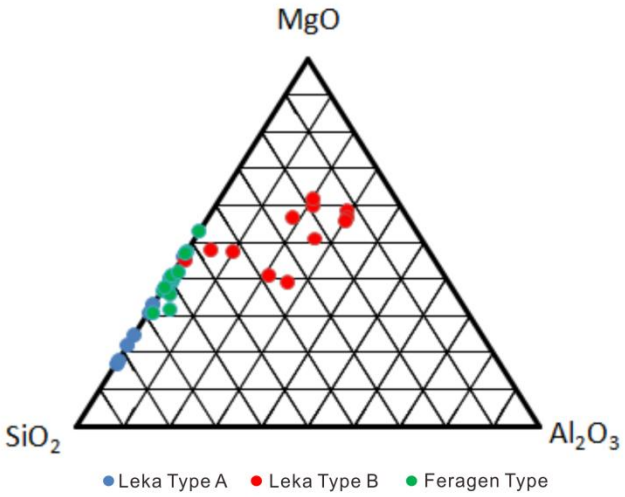


(b) MgO-SiO2-Al2O3 triangular diagram about cementing material from both of Leka and Feragen tillites

**Fig 5.3 Triangular diagrams of different combinations of three oxides in the tillites cement**

## 5.2.2 Carbonate and undulose extinction of quartz

Calcite, dolomite and hydrated magnesium carbonate (dypingite) are discovered in Leka tillite. Calcite and dolomite are usually observed to form near those dissolved quartz grain. Carbonate is also a common cement in some sedimentary rocks. However, the carbonate in Leka tillite is not observed to bind fragments together, it just locates in the same hole containg dissolved quartz grain. Therefore, carbonate is not considered as another cementing material in addition to the cement of magnesium silicate in Leka tillite.

Hydrated magnesium carbonate showing desert-rose structure is recognized in Feragen tillite. It often grows on serpentinized ultramafic grain's surface and has not demonstrated the ability of binding materials yet based on current observation for it. In addition, the walls of a shaft in Feragen area are commonly coated with lansfordite (a hydrated magnesium carbonate), and the shaft is connected with atmosphere(Beinlich and Austrheim, 2012), displayed in Fig 5.4. The formation of the hydrated magnesium carbonate on the shaft wall is related with evaporation process (Beinlich and Austrheim 2012). Similarly, the lithification observed in the channel wall (near the shaft, refers to Fig 4.8) is also possible to be linked with evaporation. Fluids carrying ions flow through

the wall and then evaporate from the channel wall to atmosphere, while $CO_2$ enters pore fluid at the wall surface by diffusion. Therefore, precipitate of magnesium silicate hydrate or magnesium carbonate hydrate can form from pore fluid between ultramafic fragments in the part near the wall, and binds them together as cementing material, displayed in Fig 5.5. However, the evaporation process is relatively difficult to happen in the inner part of the wall. Consequently, there will not be enough precipitate formed as cementing material between fragments, which can explain why the inner part is not lithified.

According to the history of Feragen mining activity (mining for chromite in Feragen is during 19th century and stopped about 100 years ago, refers to Beinlich et al., 2012), the shaft was excavated by miner in the last 100 years. Thus, the carbonate on the shaft wall was formed in the last 100 years as well. In addition, it could also imply that the lithification of the tillite in the channel wall at Feragen was finished in the last century.


**Fig 5.4 (a) The wall coated with lansfordite(white) of a shaft at Feragen. (b)Close-up photo about the white mineral on the shaft wall. Photos are from Beinlich et al., 2012**

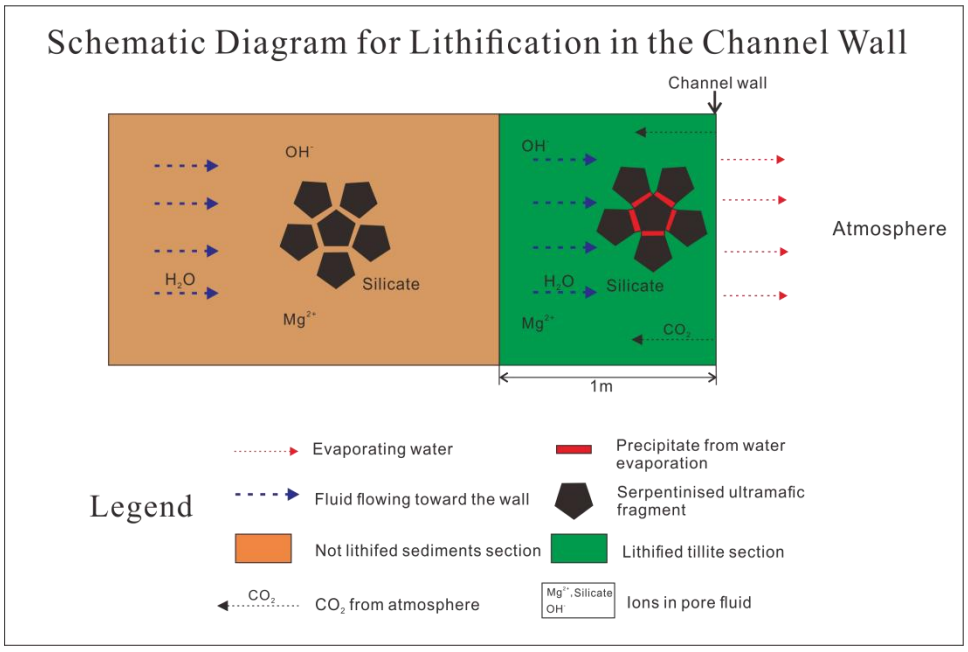


**Fig 5.5 Schematic Diagram for the lithification in the channel wall at Feragen**

Almost all quartz grains in Feragen tillite have the characteristic of undulose extinction, which means that the Feragen quartz grains have been deformed. The exactly happen time of the deformation is still unknown. If it happened in the last glaciation, then the deformation of quartz grain may be caused by the pressure of glacier. More likely, it could happen earlier than the tillite formed. In the Feragen case, it may enhance the dissolution ability of quartz. However, undulose extinction is not found on quartz grains from Leka tillite and the two tillites are probably formed in the same glaciation, it indicates that the deformation of quartz grain in Feragen tillite is not made by glacier.

# 5.3 Serpentinization and comparing oxide ratio in serpentine and its replacements with the cement from the two tillites.

## 5.3.1 Serpentinization and serpentine minerals

Serpentinization is a well-known hydration process affecting magnesium silicates in ultramafic rock (Moody, 1976). Furthermore, olivine is the most abundant mineral in ultramafic rocks, and its serpentinization mechanism has been intensely investigated for tens of years. In the Leka and Feragen tillites, like in most ultramafic rocks the olivine is Mg-rich close to the forsterite end member (FO90). If the serpentinization takes place in dunite or peridotite without much pyroxene content, then the hydration products would

be serpentine and brucite (Moody, 1976). Chemical expression for such serpentinization is often written as below,

$$2Mg_2SiO_4 + 3H_2O = Mg_3Si_2O_5(OH)_4 + Mg(OH)_2$$

In the Feragen tillite, brucite is indeed found (Fig 4.29 b&c). On current observations for the Leka tillite, such as in SEM or EMP, brucite has not been found so far. However, serpentinized ultramafite clasts are observed in many places in the tillite with the occurrence of magnesium carbonate (table 4.6) and dypingite (found by XRD). They could be results of brucite weathering with $CO_2$-bearing fluids (Moody, 1976). The brucite has been found in the bedrock of Leka tillite(Iyer et al., 2008).Therefore, it is assumed that brucite is present in Leka tillite as well. Additionally, brucite in the Feragen tillite contains Fe element that may be released from the serpentinization of fayalite(ironic olivine-$Fe_2SiO_4$).

Serpentine is actually a name for a group of minerals, which have almost the same chemical formula $Mg_3Si_2O_5(OH)_4$. These minerals are namely lizardite, chrysotile and antigorite. Nevertheless, their micro structures are different. Usually, the trioctahedral 1:1 layer is the basic, but the detailed assembly is different, lizardite is made up of two planar layers. These layers being chrysotile, which consists of two scrolled layers, and the two layers in antigorite crystal are periodically reverse to that of lizardite, the sketch diagrams about serpentine crystal structures are shown in the Fig 5.6 (Mével, 2003):

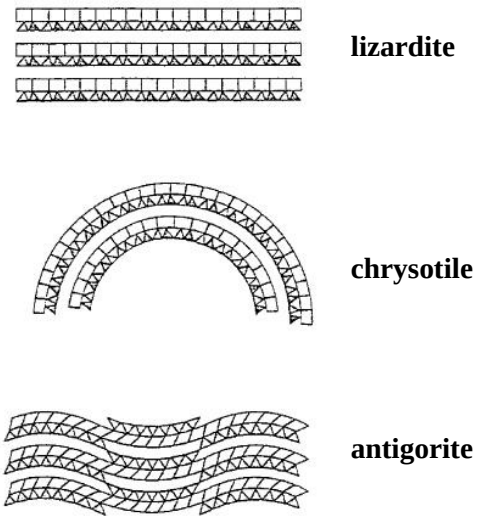


**Fig 5.6 Crystal structure for minerals in serpentine group (Mével, 2003)**

In the serpentine micro-structure, the Si at tetrahedral sites can be replaced by Al and $Fe^{3+}$, while Mg at octahedral sites can be substituted by $Fe^{2+}$, $Fe^{3+}$, Cr, Al, Ni and Mn(Mével, 2003). Among the 3 dominant members, lizardite is favorable for such substitution processes. Whereas the substitutions are not the same popular in antigorite as it lacks of octahedral sites(Mével, 2003).

Antigorite and lizardite are identified as the two dominant kinds of serpentine minerals in the Leka tillite.

### 5.3.2 Oxide ratio in serpentine, replacement minerals from serpentine and the tillites' cement.

Feldspar mineral is unstable on the surface of earth; it can be altered to various clay minerals according to corresponding weathering conditions. For example, albite is altered to montmorillonite when there is the presence of $Mg^{2+}$, while alteration product is kaolinite or gibbsite if the reaction environment is acidic (Appelo and Postma, 2005). In both Leka and Feragen tillites, Mg silicate minerals have been widely weathered. Therefore, $Mg^{2+}$ in the pore fluids of the tillite should be abundance, and the pore fluids is unlikely to be acidic because of the brucite dissolution. Thus, the reaction for albite weathering here is expressed as below:

$$3Na(AlSi_3)O_8 + Mg^{2+} + 4H_2O \rightarrow 2Na_{0.5}(Al_{1.5}Mg_{0.5})Si_4O_{10}(OH)_2 + 2Na^+ + H_4SiO_4$$

(Appelo and Postma, 2005)

However, the montmorillonite has not yet been detected or observed in the thin sections from the Leka tillite, which seems to need further analysis on them in the future to solve this question.

As discussed earlier, the cement in the Leka tillite has two dominant types, one is Type A in the $MgO$-$SiO_2$-$H_2O$ system and the other one is Type B in the $MgO$-$SiO_2$-$Al_2O_3$-$H_2O$ system. Type B is always found to be surrounding a dissolved plagioclase grain. Al, Cr, Ni are regared as relatively immobile during alteration process of serpentinization(Mével, 2003). Moreover, it indicates that Al in the Type B cement within the Leka tillite is likely from in situ dissolved plagioclase grain. In addition, both the two kinds of cement have a similar composition as serpentine mineral. Consequently, there is a hypothesis for the formation of such cement, the fundamental mineral for the

cement is serpentine formed by serpentinization, and it absorbs some other elements during its weathering, such as Al, released from other mineral's weathering (such as plagioclase) and partly substitutes Si at tetrahedral site in the serpentine structure. The proper type of serpentine mineral here is considered as lizardite instead of antigorite based on their abilities to be substituted. As weathering of substituted serpentine mineral continues, there may be such kind of cement formed

Mg and Si can be substituted by Al in lizardite structure, but this process is not an instant process; as there will be some intermediate mineral phases between lizardite and its end member. Those intermediate minerals can be named as septechlorites, while the name for the resulted end member is amesite (Moody, 1976). $(MgAl)_3(SiAl)_2O_5(OH)_4$ and $Mg_2Al(SiAl)O_5(OH)_4$ are general structure formulae for septechlorites and amesite, respectively. Lizardite, septechlorites and amesite can be considered under the $MgO$-$SiO_2$-$Al_2O_3$-$H_2O$ system for the ratios between each oxide. The molar ratio $MgO$: $SiO_2$: $Al_2O_3$: $H_2O$ is from 1 : 0.67 : 0 : 0.67 to 1 : 0.5 : 0.5 : 1 from unsubstituted lizardite to the end member amesite, while ratios for intermediate septechlorites are between them.

Using a general mathematical expression for the ratio to look further into the relations between the 4 components, which can give a clearer impression about elements changing and moving. The detailed mathematical process is demonstrated below,

Firstly assume that there are $\mathbf{x}$ moles $MgO$ and $\mathbf{y}$ moles $SiO_2$ in one mole molecular $(MgAl)_3(SiAl)_2O_5(OH)_4$ of septechlorite, and $2 \ll \mathbf{x} \ll 3$ that is obtained based on magnesium number in lizardite's formula and amesite formula respectively.

As charge balance in chemical formula, so

$$2x + 4y + (5 - x - y) \cdot 3 + 4 = 18$$

$$y = x - 1$$

Thus the ratio $MgO : SiO_2 : Al_2O_3 : H_2O$ can be expressed as x : x-1 : 3-x : 2, then normalize the number of $MgO$ in ratio to 1 as x is a positive real number, the ratio becomes that

$$1:(1-\frac{1}{x}):(\frac{3}{x}-1):\frac{2}{x}\ (2 \ll \mathbf{x} \ll 3)$$

In addition, there are 21 potential values made for such ratio. These are estimated from x changing from 2 to 3, with an increment value of 0.05 in matlab. These potential values are tabulated to be useful for comparing them with actual such ratios in the cements from the two tillites. Comparing each ratio in table 5.1 with those ratios for cement in the Lek tillite, it is found that most of cement values are quite different to those for pure serpentine and its substituted minerals in table 5.1. Based on the actual ratio values for the Leka cement, they are classified again as 4 groups. Group I, which contains all WDS analysis points for Type A cement, shows that both their $SiO_2$ and $H_2O$ contents exceed all possible values in table 5.1, but no $Al_2O_3$ included. Group II has only two WDS analysis points No.37 and No.42, belonged to Type B cement, whose $SiO_2$, $Al_2O_3$ and $H_2O$ contents are higher than those in table 5.1. Group III, contains WDS points 1, 22 and 40 of Type B, has only $H_2O$ content that exceeds potential values for $H_2O$ in the table 5.1, while their ratio values for $SiO_2$ and $Al_2O_3$ are in the ranges of table 5.1. Group IV, includes WDS points 4, 6, 7, 30, 33, 38, 44, 51 of type B. They are with the three characteristics of much lower $SiO_2$ content than serpentine and its substituted minerals, $Al_2O_3$ contents consistent with some values in table 5.1, but $H_2O$ contents are higher.

The Feragen Type cement also has higher contents of $SiO_2$ and $H_2O$, because of the ratio values of the two oxides in MgO : $SiO_2$ : $Al_2O_3$ : $H_2O$ for Feragen cement are usually larger than those in table 5.1. howerver, its $Al_2O_3$ content is lower than that in table 5.1.

The actual ratio values for the Leka and Feragen cements are quite different to the calculated ones of serpentine and its substituted members. Furthermore, the cement in the two tillites may also be amorphous magnesium silicate material. Thus, the hypothesis that the cement is from serpentine is unlikely to be correct. In addition, dissolutions of quartz and feldspar have been confirmed to provide some main elements for the formation of cement, and brucite (the other product of serpentinization) weathering is also observed. Consequently, it is more reasonable that quartz, feldspar and brucite can be the material sources of cement in the tillites.

**Table 5.1 Estimation for normalized ratio MgO : $SiO_2$ : $Al_2O_3$ : $H_2O$ in lizardite and its substituted minerals**

| x | MgO | $SiO_2$ | $Al_2O_3$ | $H_2O$ |
|---|---|---|---|---|
| 2 | 1 | 0.50 | 0.50 | 1 |
| 2.05 | 1 | 0.51 | 0.46 | 0.98 |
| 2.10 | 1 | 0.52 | 0.43 | 0.95 |
| 2.15 | 1 | 0.53 | 0.40 | 0.93 |
| 2.2 | 1 | 0.55 | 0.36 | 0.91 |
| 2.25 | 1 | 0.56 | 0.33 | 0.89 |
| 2.3 | 1 | 0.57 | 0.30 | 0.87 |
| 2.35 | 1 | 0.57 | 0.28 | 0.85 |
| 2.4 | 1 | 0.58 | 0.25 | 0.83 |
| 2.45 | 1 | 0.59 | 0.22 | 0.82 |
| 2.5 | 1 | 0.60 | 0.20 | 0.80 |
| 2.55 | 1 | 0.61 | 0.18 | 0.78 |
| 2.6 | 1 | 0.62 | 0.15 | 0.77 |
| 2.65 | 1 | 0.62 | 0.13 | 0.75 |
| 2.7 | 1 | 0.63 | 0.11 | 0.74 |
| 2.75 | 1 | 0.64 | 0.09 | 0.73 |
| 2.8 | 1 | 0.64 | 0.07 | 0.71 |
| 2.85 | 1 | 0.65 | 0.05 | 0.70 |
| 2.9 | 1 | 0.66 | 0.03 | 0.69 |
| 2.95 | 1 | 0.66 | 0.02 | 0.68 |
| 3 | 1 | 0.67 | 0.00 | 0.67 |

## 5.4 Estimation for mineral dissolution rate in Leka tillite

### 5.4.1 Estimation for quartz dissolution rate and comparing it with the experiment rate

As mentioned previously, quartz dissolution is found in Leka tillite. The shapes of some remain quartz grain is similar as the outline of the hole where it is, as seen in Fig 4.23 (I) &(II). This indicates that the observed quartz dissolution process from the initial state to the current state started after its deposit. Consequently, based on the kinetic parameters about quartz dissolution and the dissolved ratio of quartz grain, it is possible to estimate the quartz dissolution rate during the deposit process.

Firstly, it is thought that the Leka tillite originates from the latest glaciations and that the weathering of brucite will increase the pH of the pore fluid. Furthermore, brucite has a low solubility. It is reasonable to make the second assumption that pore fluid is saturated with brucite, and its resulted pH is about 10. In addition, there is a lack of data about ancient temperature in the Leka area, so it has to estimate the dissolution rate of quartz under current climate data. The weather on Leka island is usually cold. 273K will be then used in the estimation for the quartz dissolution rate, which is almost the same as that in PHREEQC simulation (refer to section 4.6.1).

There are another two assumptions, one is that the quartz grains, both of its initial grain (equal to the hole where it is ) and remain grain (current grain) during the dissolution process (refer to Fig 4.23) are considered as spheres with the equivalent radius in the calculation. With the other assumption is that dissolution rate is the same along all directions towards the center of quartz sphere. Moreover, with dissolution goes, the quartz sphere will decrease in radius homogeneously. The equivalent initial radius and current radius for the same quartz grain are estimated from the initial area and current one, respectively. The latest glaciations period almost ended 10000 years ago, the time value in calculation thus is $3.15 \times 10^{11}$ s. There are two different ways to estimate the quartz dissolution rate; one is the observed rate equation in the given time,

$$\frac{dm}{dt} = \frac{\rho}{M} \cdot \frac{4}{3} \cdot \pi \frac{d(r^3)}{dt} \qquad \textbf{(eq-3)}$$

Where M is the mole mass of quartz, ρ is quartz density, 2.66g/cm$^3$, d(r$^3$) is the difference between initial $r_0^3$ and current $r^3$ and dt is the time span.

The equation **eq4** below is simplified from **eq2** (section 3.6.2) for theoretical dissolution rate of quartz in basic mechanism,

$$\frac{dm}{dt} = S \cdot K_{base}^{298} e^{\frac{-E_{base}}{R}\left(\frac{1}{T}-\frac{1}{298}\right)} a_{H^+}^{n_3} \qquad (\textbf{eq-4})$$

Comparing **eq-4** with the equation **eq-2**, the **eq-4** is without the term about saturation state of solution $(1-\Omega^{p_3})^{q_3}$ because of it is firstly assumed to be under the situation where the solution (pore fluids) is extremely unsaturated with quartz during the whole deposit process. The rate calculated by the equation **eq-4** then can be considered as the maximum theoretical dissolution rate. In addition, the surface area S is equal to $4\pi\bar{r}^2$, while $\bar{r}$ is estimated by averaging the two values of remain radius and initial radius . The influence of grain radius on the rate is much smaller than other factors in the **eq-4**. Consequently, the average radius $\bar{r}$ can be used in the calculation. The rate constant is $10^{-16.29}$ mole $\cdot$ m$^{-2}$ $\cdot$ s$^{-1}$ at 298K for quartz in base mechanism. The exponent $n_3$ of $a_{H^+}$ is -0.5 in the same mechanism and activation energy of quartz in basic condition is 96KJ/mole(Worley and Tester, 1994).

In the situation of that pore fluid is much unsaturated with respect to quartz, then the observed rate should be similar to the calculated theoretical rate. The calculated results are listed in Table 5.2. However, the observed rate and the theoretical one are quite different based on the results in Table 5.2. As a result, this large difference may mean that the actual solution state in pore fluids is very close to saturation state with respect to quartz. On the other hand, the observed dissolution rates of the 3 quartz grains are almost the same or close to each other, which is consistent with that they stay in the same environment.

If the time span is 5000 years, which is realistic to consider that the ground of Leka may be frozen during half of the 10000 years, then the observed dissolution rate of quartz grain is increased to $4.8 \times 10^{-19}$mol/s, still very lower. If the quartz dissolution can be equal to the theoretical one all the time during its deposit, the needed time for dissolving to the same extent is decreased to about 2 years. The observed dissolution rate ($2.4 \times 10^{-19}$mol/s) of quartz grain is approximately 1/2000000 of the smaller

dissolution rate ($4.6 \times 10^{-13}$mol/s) of quartz (SP9) in experiment. The concentration of OH- in the experiment (pH=13) is rougly a thousand times as high as that in the ultramafic tillite (pH=10), but its rate can be much faster than the rate in the ultramafic tillite. Thus, it indicates that promoting pH could be a high-efficient way to dissolving quartz for generating the cement. The dissolution rate ($1.8 \times 10^{-12}$mol/s) of quartz specimen (SP 4) in a lower temperature (4.5℃) is almost four times as fast as rate of SP9 (20℃). This means that cold environment is also favorable for quartz dissolution in addition to pH.

The lithification in Feragen tillite may be during the last 100 years (section 5.2.2). If the lithification in Leka tillite is in the same period, the observed dissolution rate for quartz ($2.4 \times 10^{-17}$ mol/s)will be 100 times as large as that in Table 5.2, but it's still very low in comparison with the theoretical one. It becomes around 3% of the theoretical rate in Table 5.2.

**Table 5.2 Estimation results for quartz dissolution in the Leka tillite**

| *Quartz grain* | *Initial equivalent radius(um)* | *Remain equivalent radius (um)* | *dr3 ($10^5 um^3$)* | *Time span (s)* | *Observed dissolution rate (mol/s)* | *Theoretical Dissolution rate (mol/s)* |
|---|---|---|---|---|---|---|
| I | 86.7 | 61.7 | 4.17 | $3.15 \times 10^{11}$ | $2.4 \times 10^{-19}$ | $2.0 \times 10^{-15.3}$ |
| II | 81.8 | 51.7 | 4.01 | $3.15 \times 10^{11}$ | $2.4 \times 10^{-19}$ | $1.6 \times 10^{-15.3}$ |
| III | 78.2 | 44.1 | 3.92 | $3.15 \times 10^{11}$ | $2.3 \times 10^{-19}$ | $1.4 \times 10^{-15.3}$ |

## 5.4.2 Estimation for dissolution rate of feldspar mineral

Similarly, the observed dissolution rate and theoretical dissolution rate of feldspar mineral from Leka tillite are estimated with the same equations (**eq-3** and **eq-4**) , assumptions and the same conditions (same pH and temperature). Only those parameters ( rate constant, exponent n of $a_{H^+}$, and activation energy) for albite in basic mechanism are found in Palandri et al., 2004. The rate constant for albite is $10^{-15.60}$mol $\cdot$ $m^{-2} \cdot s^{-1}$ at 298K , and the exponent $n_3$ of $a_{H^+}$ is -0.572 for albite in base mechanism. The activation energy for it in the same mechanism is 71 KJ/mole (Palandri et al., 2004).

The estimation for feldspar has to be based on albite. In addition, the plagioclase grain WDS 50 in Fig 4.22 is the most close to albite in composition, where its dissolution ratio is 24.7% (refer to Table 4.7). Its density is 2.62 g/cm$^3$.

Its actual dissolution rate is $1.8 \times 10^{-26}$ mol/s, and its theoretical rate is $1.1 \times 10^{-18.28}$mol/s. WDS 50 has the lowest content of anorthite. As a result, other feldspar grains' theoretical rates may be higher than $1.8 \times 10^{-26}$ mol/s . The difference between feldspar's observed rate and theoretical rate implies that the pore fluid is close to saturation with feldspar minerals.

## 5.5 Local topography around Leka tillite site and its implication for local hydrology environment

The 3-dimensional topography image about the Leka tillite site can demonstrate local land features directly. The elevation about the site is about 50 meter, while the local highest position on the mountain is about 215 meter, which is approximately 400 meter away east to the site. There is a red line in the Fig 5.7 (a) that connects the site point (shown in yellow marker) with a certain point near the highest one (in red marker). This represents a vertical profile with trend of 90°E. The actual topography along the profile is plotted against the horizontal position in Fig 5.7 (b) where the tillite site is considered to be at the 0 position on the horizontal axis. The 3-D figure and the data of topography are obtained using the application of Google Earth, which is also used to process elevation data to obtain actual slope situation along the profile's outline. Mostly the slopes of the points on the outline are within the range of 40% to 50%.


(a)

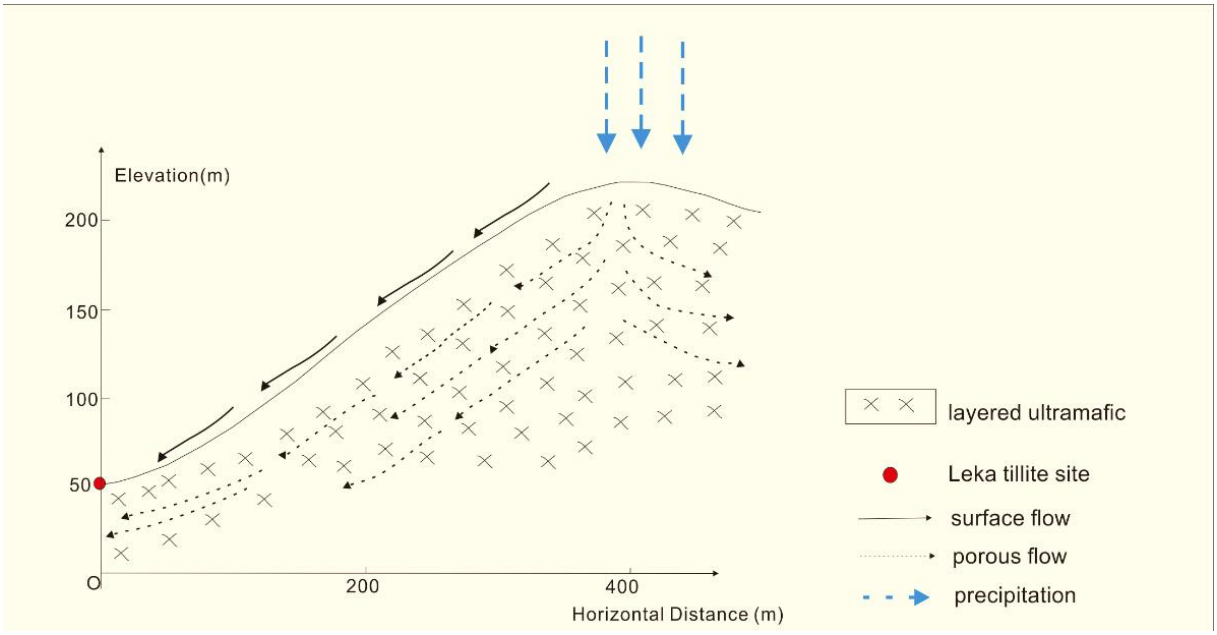


(b)

**Fig 5.7 (a) 3D topography image about the Leka tillite site; (b)The profile through the red line.** .

The local topographical feature may have an influence on the local hydrology background. For instance, when the rain falls at this site, some of it will flow along the surface of the slope to the tillite site, shown as full line arrow in Fig 5.7 (b). However, water can also enter the porous or fracture networks in the rock body. This could then enter the underground water below the site if there are fractures or channels connecting them occur (represented by dash arrow in Fig 5.7 (b)). As mentioned above, the rock body of ultramafic or mafic rock has undergone weathering process, which will provide

some elements released from such weathering to the water flow through it, such as $Mg^{2+}$. Thus, the compositions of the surface water and the underground water are different. As a consequence, they can give various influences on the formation of the cement in the Leka tillite. For example, the water flowing through the rock body probably carry $Mg^{2+}$ and $OH^-$ from weathering of ultramafic mineral. In addition, the mining site near location 2 (Fig 4.9) in Feragen region has a pH value of 9.34, and pH of the creak originning it and flowing through the location 2 is 8.0 (slight basic). They confirm that the tillite is inlfuenced by the basic fluids resulted from weathering of local ultramafic rock.

# 6 *Summary*

1. The two tillites are unique as that they apparently contain ultrmafic fragments from local complexes. However, quartz and feldspar minerals are also observed within them, which are unlikely from the same local rock bodies. Thus, both the tillites have multiple material sources.

2. Quartz and feldspar are dissolved in the tillite. The dissolution of quartz is more rapid than feldspar. Serpentinized ultramafic mineral grain has been weathered and provides brucite resulting in a high pH environment in the tillite by its dissolution. This is considered as the reasonable reason for quartz dissolution. In addition, dissolutions of quartz and feldspar give Si and Al with Mg from brucite dissolution to the formation of cement in the tillites.

3. In addition to the three dominant elements mentioned above, water content is obviously high in the cement. It means that the hydration process of the cement may be good for increasing its ability of binding materials.

4. The experimentally determined quartz dissolution rate ($4.6 \times 10^{-13}$ to $1.8 \times 10^{-12}$ mol/s) is much higher than actual dissolution in Leka tillite. The experiment results indicate that higher pH and lower temperature are positive factors for quartz dissolution within brucite saturated solution. Whether they are also good for the cement formation or not is still unconfirmed. If there are more works to perform on researching the relationships between the cement formation, mineral influence, pressure and temperature, it can be helpful to find out a way of accelerating the cement generation process.

5. From the researchs of the thesis on the cement, it can be said that ultramafic mineral, quartz and feldpspar can be material sources for a new potential cement. They are not only abundant in crust, but also easily to be exploited. Significantly, they don't contain any $CO_2$. Consequently, it can be more environmental during processing them than burning limestone for producing Portland cement.

# *Bibliography*


Ali, M.M., Gopal, S., and Handoo, S.K., 1994, Studies on the formation kinetics of calcium sulphoaluminate: Cement and Concrete Research, v. 24, no. 4, p. 715–720, doi: 10.1016/0008-8846(94)90196-1.

Appelo, C.A.., and Postma, D., 2005, Geochemistry,groundwater and pollution: A.A. Balkema Publishers, Amsterdam.

Arvidson, R.S., Ertan, I.E., Amonette, J.E., and Luttge, A., 2003, Variation in calcite dissolution rates: A fundamental problem? Geochimica et Cosmochimica Acta, v. 67, no. 9, p. 1623–1634.

Austrheim, H., and Prestvik, T., 2008, Rodingitization and hydration of the oceanic lithosphere as developed in the Leka ophiolite, north-central Norway: Lithos, v. 104, no. 1-4, p. 177–198, doi: 10.1016/j.lithos.2007.12.006.

Barret, P., and Ménétrier, D., 1980, Filter dissolution of C3S as a function of the lime concentration in a limited amount of lime water: Cement and Concrete Research, v. 10, no. 4, p. 521–534, doi: 10.1016/0008-8846(80)90096-4.

Barret, P., Ménétrier, D., and Bertrandie, D., 1983, Mechanism of C3S dissolution and problem of the congruency in the very initial period and later on: Cement and Concrete Research, v. 13, no. 5, p. 728–738, doi: 10.1016/0008-8846(83)90064-9.

Beinlich, A., and Austrheim, H., 2012, In situ sequestration of atmospheric CO 2 at low temperature and surface cracking of serpentinized peridotite in mine shafts: Chemical Geology, v. 332-333, p. 32–44, doi: 10.1016/j.chemgeo.2012.09.015.

Bellmann, F., Damidot, D., Möser, B., and Skibsted, J., 2010, Improved evidence for the existence of an intermediate phase during hydration of tricalcium silicate: Cement and Concrete Research, v. 40, no. 6, p. 875–884.

Bellmann, F., Stark, J., and Matschei, T., 2005, Hydration behaviour of sulphate-activated slag cements: Advances in Cement Research, v. 17, no. 4, p. 167–178, doi: 10.1680/adcr.2005.17.4.167.

Bijen, J., and Niël, E., 1981, Supersulphated cement from blastfurnace slag and chemical gypsum available in the Netherlands and neighbouring countries: Cement and Concrete Research, v. 11, no. 3, p. 307–322, doi: 10.1016/0008-8846(81)90104-6.

Bishnoi, S., and Scrivener, K.L., 2009, µic: A new platform for modelling the hydration of cements: Cement and Concrete Research, v. 39, no. 4, p. 266–274, doi: 10.1016/j.cemconres.2008.12.002.

Bullard, J.W., and Flatt, R.J., 2010, New insights into the effect of calcium hydroxide precipitation on the kinetics of tricalcium silicate hydration: Journal of the American Ceramic Society, v. 93, no. 7, p. 1894–1903.

Bullard, J.W., Jennings, H.M., Livingston, R.A., Nonat, A., Scherer, G.W., Schweitzer, J.S., Scrivener, K.L., and Thomas, J.J., 2011, Mechanisms of cement hydration: Cement and Concrete Research, v. 41, no. 12, p. 1208–1223, doi: 10.1016/j.cemconres.2010.09.011.

Bushnell-Watson, S.M., and Sharp, J.H., 1990, On the cause of the anomalous setting behaviour with respect to temperature of calcium aluminate cements: Cement and Concrete Research, v. 20, no. 5, p. 677–686, doi: 10.1016/0008-8846(90)90002-F.

CAMCOR at University of Oregon, 1995, Telemedicine Journal, v. 1, no. 4, p. 11, doi: 10.1089/tmj.1.1995.1.347.

D.Damidot, 2007, Calculation of the dissolution rate of tricalcium silicate in several electrolyte compositions: Cement Wapno Beton, v. 2, p. 57–67.

Damidot, D., Nonat, A., and Barret, P., 1990, Kinetics of Tricalcium Silicate Hydration in Diluted Suspensions by Microcalorimetric Measurements: Journal of the American Ceramic Society, v. 73, no. 11, p. 3319–3322.

Dunning, G.R., and Pedersen, R.B., 1988, U/Pb ages of ophiolites and arc-related plutons of the Norwegian Caledonides: implications for the development of Iapetus: Contributions to Mineralogy and Petrology, v. 98, no. 1, p. 13–23, doi: 10.1007/BF00371904.

Dutta, D.K., and Borthakur, P.C., 1990, Activation of low lime high alumina granulated blast furnace slag by anhydrite: Cement and Concrete Research, v. 20, no. 5, p. 711–722, doi: 10.1016/0008-8846(90)90005-I.

Duxson, P., Provis, J.L., Lukey, G.C., and van Deventer, J.S.J., 2007, The role of inorganic polymer technology in the development of “green concrete”: Cement and Concrete Research, v. 37, no. 12, p. 1590–1597, doi: 10.1016/j.cemconres.2007.08.018.

Erdem, E., and Ölmez, H., 1993, The mechanical properties of supersulphated cement containing phosphogypsum: Cement and Concrete Research, v. 23, no. 1, p. 115–121, doi: 10.1016/0008-8846(93)90141-U.

Furnes, H., Pedersen, R.B., and Stillman, C.J., 1988, The Leka Opholite Complex, central Norwegian Caledonides: field characteristics and geotectonic significance: Journal of the Geological Society, v. 145, no. 3, p. 401–412, doi: 10.1144/gsjgs.145.3.0401.

Garrault, S., 2005, Study of C-S-H growth on C3S surface during its early hydration: Materials and Structures, v. 38, no. 278, p. 435–442, doi: 10.1617/14343.

Garrault, S., and Nonat, A., 2001, Hydrated layer formation on tricalcium and dicalcium silicate surfaces: Experimental study and numerical simulations: Langmuir, v. 17, no. 26, p. 8131–8138.

Garrault-Gauffinet, S., and Nonat, A., 1999, Experimental investigation of calcium silicate hydrate (C-S-H) nucleation: Journal of Crystal Growth, v. 200, no. 3, p. 565–574.

Gartner, E., 2004, Industrially interesting approaches to “low-CO2” cements: Cement and Concrete Research, v. 34, no. 9, p. 1489–1498, doi: 10.1016/j.cemconres.2004.01.021.

Gartner, E.M., 2011, Potential improvements in cement sustainability: 31st Cement and Concrete Science Conference, p. 13.

Gartner, E.M., and MacPhee, D.E., 2011, A physico-chemical basis for novel cementitious binders: Cement and Concrete Research, v. 41, no. 7, p. 736–749, doi: 10.1016/j.cemconres.2011.03.006.

Gartner, E.M., and Macphee, D.E., 2011, A physico-chemical basis for novel cementitious binders: Cement and Concrete Research, v. 41, no. 7, p. 736–749, doi: 10.1016/j.cemconres.2011.03.006.

George, C., 1983, Industrial aluminous cements (P. Barnes, Ed.): Elsevier Ltd, London.

Glasser, F.P., and Zhang, L., 2001, High-performance cement matrices based on calcium sulfoaluminate-belite compositions: Cement and Concrete Research, v. 31, no. 12, p. 1881–1886, doi: 10.1016/S0008-8846(01)00649-4.

Goldschmidt, V.M., 1913, Das Devongebiet am Røragen bei Røros. Skr. Nor. Vidensk. Akad i Oslo:.

Gruskovnjak, A., Lothenbach, B., Winnefeld, F., Figi, R., Ko, S.C., Adler, M., and Mäder, U., 2008, Hydration mechanisms of super sulphated slag cement: Cement and Concrete Research, v. 38, no. 7, p. 983–992, doi: 10.1016/j.cemconres.2008.03.004.

Hultin, I., 1965, En mineralogisk undersøkelse as kromitmalmer i Feragen, Kartbaldet Aursunden: Universitetet i Oslo.

I.Odler, 1981, Early hydration of tricalcium silicate 3. Control of the induction period: Cem.Concr.Res, v. 11, p. 765–774.

Imbert, L., Geringer, J., Boyer, B., and Farizon, F., 2012, Proceedings of the Institution of Mechanical Engineers , Part J , Journal of Engineering Tribology Wear analysis of hip explants , dual mobility concept : comparison of quantitative and qualitative analyses: Journal of Engineering Tribology, v. 10, p. 838–853.

Ings, J.B., Brown, P.W., and Frohnsdorff, G., 1983, Early hydration of large single crystals of tricalcium silicate: Cement and Concrete Research, v. 13, no. 6, p. 843–848, doi: 10.1016/0008-8846(83)90085-6.

Iyer, K., Austrheim, H., John, T., and Jamtveit, B., 2008, Serpentinization of the oceanic lithosphere and some geochemical consequences: Constraints from the Leka Ophiolite Complex, Norway: Chemical Geology, v. 249, no. 1-2, p. 66–90, doi: 10.1016/j.chemgeo.2007.12.005.

J.F.Young, E.M.G., 2002, Hydration of portland cement: Structure and Performance of Cements, 2nd Edition, p. 57–113.

J.N.Maycock, and J.P.Skalny, 1974, Solid-state defects and clinker mineral hydration: Am.Ceram.Soc.Bull, v. 53, p. 326.

J.Thomas, J., 2013, A New Approach to Modeling the Nucleation and Growth Kinetics of Tricalcium Silicate Hydration: Society, American Ceramic,.

Jennings, H.M., and Pratt, P.L., 1979, An experimental argument for the existence of a protective membrane surrounding portland cement during the induction period: Cement and Concrete Research, v. 9, no. 4, p. 501–506.

Juenger, M.C.G., Winnefeld, F., Provis, J.L., and Ideker, J.H., 2011, Advances in alternative cementitious binders: Cement and Concrete Research, v. 41, no. 12, p. 1232–1243, doi: 10.1016/j.cemconres.2010.11.012.

Juilland, P., Gallucci, E., Flatt, R., and Scrivener, K., 2010, Dissolution theory applied to the induction period in alite hydration: Cement and Concrete Research, v. 40, no. 6, p. 831–844, doi: 10.1016/j.cemconres.2010.01.012.

Kurtis, K., 2007, Portland Cement Hydration: , p. 1–35.

Lasaga, A.C., and Luttge, A., 2001, Variation of crystal dissolution rate based on a dissolution stepwave model.: Science (New York, N.Y.), v. 291, no. 5512, p. 2400–2404.

Li, L., Chiu, K.Y., Scigajlo, D., and Dinku, B., 2013, Case study Feragen Green Concrete-student assigment report for course FYS-GEO4200: , no. December.

Lüthi, D., Le Floch, M., Bereiter, B., Blunier, T., Barnola, J.-M., Siegenthaler, U., Raynaud, D., Jouzel, J., Fischer, H., Kawamura, K., and Stocker, T.F., 2008, High-resolution carbon dioxide concentration record 650,000-800,000 years before present.: Nature, v. 453, no. 7193, p. 379–382, doi: 10.1038/nature06949.

Mehrotra, V.P., Sai, A.S.R., and Kapur, P.C., 1982, Plaster of Paris activated supersulfated slag cement: Cement and Concrete Research, v. 12, no. 4, p. 463–473, doi: 10.1016/0008-8846(82)90061-8.

Mével, C., 2003, Serpentinization of abyssal peridotites at mid-ocean ridges: Comptes Rendus Geoscience, v. 335, no. 10-11, p. 825–852, doi: 10.1016/j.crte.2003.08.006.

Moody, J.B., 1976, Serpentinization: a review: Lithos, v. 9, no. 2, p. 125–138, doi: 10.1016/0024-4937(76)90030-X.

Moore, A.C., and Hultin, I.A., 1980, petrology mineraligy and origin of the Feragen ultramafic body Sør-Trøndelag Norway.pdf: Norsk Geologisk Tidsskrift, v. 60, p. 235–254.

Mun, K.J., Hyoung, W.K., Lee, C.W., So, S.Y., and Soh, Y.S., 2007, Basic properties of non-sintering cement using phosphogypsum and waste lime as activator: Construction and Building Materials, v. 21, no. 6, p. 1342–1350, doi: 10.1016/j.conbuildmat.2005.12.022.

Muzhen, S., Kurdowskl, W., and Sorrentino, F., 1992, DEVELOPMENT IN NON-PORTLAND CEMENTS, *in* 9th International Congress on the Chemistry of Cement, Vol. 1, p. 317–354.

Nesse, W., 2003, Introduction to Optical Mineralogy: Oxford University Press.

Nicolas, A., and Violette, J.F., 1982, Mantle flow at oceanic spreading centers: Models derived from ophiolites: Tectonophysics, v. 81, p. 319–390.

Palandri, J.L., and Kharaka, Y.K., 2004, A compilation of rate parameters of water-mineral interaction kinetics for application to geochemical modeling: U.S. Geological Survey Open file Report, v. 2004-1068, p. 71, doi: 10.1098/rspb.2004.2754.

Parkhurst, D.L., and Appelo, C. a. J., 2013, Description of Input and Examples for PHREEQC Version 3 — A Computer Program for Speciation , Batch-Reaction , One-Dimensional Transport , and Inverse Geochemical Calculations Chapter 43 of: Modeling Techniques, Book 6, p. 1–678.

Prestvik, T., and Bøe, P., 1974, A serpentinite Conglomerate on the Island of Leka Nord-Trøndelag: Norsk Geologisk Tidsskrift, v. 54, p. 117–121.

Reed, S.J.B., 2005, Electron Microprobe Analysis and Scanning Electron Microscopy in Geology: Cambridge University Press.

Sahu, S., and Majling, J., 1993, Phase compatibility in the system CaO-SiO2-Al2O3-Fe2O3-SO3 referred to sulphoaluminate belite cement clinker: Cement and Concrete Research, v. 23, no. 6, p. 1331–1339, doi: 10.1016/0008-8846(93)90070-P.

Schema MEB-wikimedia.

Schweitzer, J.S., Livingston, R.A., Rolfs, C., Becker, H.-W., Kubsky, S., Spillane, T., Castellote, M., and Viedma, P.G. de, 2007, In Situ Measurements of the Cement Hydration Profile during the Induction Period, *in* 12th International Congress on the Chemistry of Cement.,.

Scrivener, K.L., 2001, Historical and present day applications of calcium aluminate cements, *in* Proceedings of the International Conference on Calcium Aluminate Cements (CAC), Heriot-Watt University, Edinburgh, Scotland, UK, IOM Communications, p. 3–23.

Scrivener, K.L., and Capmas, A., 1998, Calcium aluminate cements in: P.C. Hewlett(Ed.): Lea's Chemistry of Cement and Concrete, p. 713–782.

Singh, M., and Garg, M., 2002, Calcium sulfate hemihydrate activated low heat sulfate resistant cement: Construction and Building Materials, v. 16, no. 3, p. 181–186, doi: 10.1016/S0950-0618(01)00026-5.

Stein, H.N., and Stevels, J.M., 1964, Influence of silica on the hydration of 3CaO.SiO2: Appl.Chem, v. 14, p. 338–346.

Su, M., Juan, D., Zongdao, W., and Xiaolin, L., 1992, Research on the chemical composition microstructures of sulpho-aluminate cement clinker, *in* 9th International Congress on the Chemistry of Cement Vol II, New Delhi, p. 94–100.

Su, M., Wang, Y., and Zhang, L., 1997, Preliminary study on the durability of sulfo/ferro-aluminate cements, *in* 10th International Congress on the Chemistry of Cement, Gothenburg, p. 4iv029.

Taha, A.S., EI-Diamony, H., Abo-El-Enein, S.A., and Amer, H.A., 1981, Physico -chemical properties of supersulphated cement pastes: Zem. Kalk Gips, v. 6, p. 315–317.

Thomas, J.J., Allen, A.J., and Jennings, H.M., 2009, Hydration Kinetics and Microstructure Development of Normal and CaCl2-Accelerated Tricalcium Silicate Pastes: The Journal of Physical Chemistry C, v. 113, no. 46, p. 19836–19844, doi: 10.1021/jp907078u.

Titus, S.J., Fossen, H., Pedersen, R.B., Vigneresse, J.L., and Tikoff, B., 2002, Pull-apart formation and strike-slip partitioning in an obliquely divergent setting, Leka Ophiolite, Norway: Tectonophysics, v. 354, no. 1-2, p. 101–119, doi: 10.1016/S0040-1951(02)00293-7.

U.S. Geological Survey, 2009, Mineral Commodity Summaries 2009: U.S. Geological Survey, p. 195 p.

Wang, L., and Glasser, F.P., 1996, Hydration of calcium sulphoaluminate cements: Adv. Cem. Res, v. 31, p. 127–134.

Wang, Y., and Su, M., 1994, The third cement series in China: World Cem., v. 8, p. 6–10.

Worley, W.G., and Tester, J.W., 1994, Dissolution Kinetics of Quartz and Granite in Acidic and Basic Salt Solutions: , p. 2545–2551.

Wu, Z.Q., and Young, J.F., 1984, The hydration of tricalcium silicate in the presence of colloidal silica: Journal of Materials Science, v. 19, no. 11, p. 3477–3486, doi: 10.1007/BF00552262.

Wyko NT9100 Optical Pro ling System System,.

ZAJAC, M., 2007, Etude des relations entre vitesse d'hydratation, texturation des hydrates et résistance mécanique finale des pâtes et micro-mortiers de ciment Portland / A study of the relationship between hydration rate, hydrate texturing and final mechanical strength o.

Zhang, L., 2000, Microstructure and performance of calcium sulfoaluminate cements: University of Aberdeen.

Zhang, L., Wang, Y., and Su, M., 1999, Development of the use of sulfo- and ferroaluminate cements in China: Advances in Cement Research, v. 11, no. 1, p. 15–21, doi: 10.1680/adcr.1999.11.1.15.

# *Appendix*

## A. WDS Analysis Results for Tillite Samples

Table 1 The EMP analysis results for feldspar in the Leka tillite. Values are presented as oxide weight percent. Feldspar is normalized to 8 oxygens.

| Sample No. | LK14-GC1 | | | | | | | |
|---|---|---|---|---|---|---|---|---|
| Thin section | 1a | | | | 1b | | | |
| Mineral | andesine | | | bytownite | andesine | K-feldspar | albite | |
| Analysis No. | 2 | 3 | 5 | 8 | 20 | 29 | 32 | 39 |
| SiO2 | 58.00 | 57.73 | 56.83 | 46.46 | 60.63 | 64.95 | 70.28 | 69.41 |
| Na2O | 6.97 | 7.06 | 6.94 | 1.29 | 7.93 | 0.23 | 12.35 | 12.16 |
| Al2O3 | 25.55 | 25.98 | 27.45 | 34.64 | 24.85 | 18.23 | 19.75 | 19.90 |
| K2O | 0.09 | 0.08 | 0.16 | 0.04 | 0.09 | 16.49 | 0.06 | 0.07 |
| CaO | 8.23 | 8.38 | 9.27 | 17.93 | 6.66 | 0.00 | 0.18 | 0.10 |
| TiO2 | 0.01 | 0.00 | 0.02 | 0.00 | 0.00 | 0.01 | 0.00 | 0.00 |
| FeO | 0.10 | 0.26 | 0.16 | 0.20 | 0.11 | 0.05 | 0.06 | 0.10 |
| MnO | 0.00 | 0.00 | 0.00 | 0.00 | 0.00 | 0.00 | 0.07 | 0.00 |
| MgO | 0.00 | 0.20 | 1.28 | 0.20 | 0.00 | 0.04 | 0.03 | 0.01 |
| Cr2O3 | 0.01 | 0.01 | 0.02 | 0.00 | 0.02 | 0.00 | 0.00 | 0.00 |
| NiO | 0.00 | 0.00 | 0.00 | 0.00 | 0.04 | 0.02 | 0.00 | 0.00 |
| Total | 98.93 | 99.67 | 102.05 | 100.58 | 100.29 | 99.86 | 102.77 | 101.70 |
| Si | 2.57 | 2.60 | 2.51 | 2.12 | 2.69 | 3.00 | 2.99 | 2.99 |
| Na | 0.60 | 0.62 | 0.59 | 0.11 | 0.68 | 0.02 | 1.02 | 1.01 |
| Al | 1.33 | 1.38 | 1.43 | 1.86 | 1.30 | 1.03 | 0.99 | 1.01 |
| K | 0.01 | 0.00 | 0.01 | 0.00 | 0.00 | 1.01 | 0.01 | 0.01 |
| Ca | 0.39 | 0.40 | 0.44 | 0.88 | 0.32 | 0.00 | 0.01 | 0.01 |
| Ti | 0.00 | 0.00 | 0.00 | 0.00 | 0.00 | 0.00 | 0.00 | 0.00 |
| Fe2+ | 0.00 | 0.01 | 0.01 | 0.01 | 0.00 | 0.00 | 0.00 | 0.00 |
| Mn | 0.00 | 0.00 | 0.00 | 0.00 | 0.00 | 0.00 | 0.00 | 0.00 |
| Mg | 0.00 | 0.01 | 0.09 | 0.01 | 0.00 | 0.00 | 0.00 | 0.00 |
| Cr | 0.00 | 0.00 | 0.00 | 0.00 | 0.00 | 0.00 | 0.00 | 0.00 |
| Ni | 0.00 | 0.00 | 0.00 | 0.00 | 0.00 | 0.00 | 0.00 | 0.00 |
| H(H2O) | 0.31 | 0.00 | 0.00 | 0.00 | 0.00 | 0.00 | 0.00 | 0.00 |

Table 1 continued

| Sample No. | LK14-GC-1 | |
|---|---|---|
| Thin section | 1b | 1a |
| Mineral | andesine | oligoclase |
| Analysis No. | 46 | 50 |
| SiO2 | 61.04 | 62.36 |
| Na2O | 8.47 | 8.81 |
| Al2O3 | 24.99 | 23.62 |
| K2O | 0.02 | 0.16 |
| CaO | 6.56 | 5.13 |
| TiO2 | 0.00 | 0.00 |
| FeO | 0.11 | 0.05 |
| MnO | 0.02 | 0.01 |
| MgO | 0.00 | 0.00 |
| Cr2O3 | 0.00 | 0.00 |
| NiO | 0.00 | 0.00 |
| Total | 101.18 | 100.14 |
| Si | 2.69 | 2.76 |
| Na | 0.72 | 0.75 |
| Al | 1.30 | 1.23 |
| K | 0.00 | 0.01 |
| Ca | 0.31 | 0.24 |
| Ti | 0.00 | 0.00 |
| Fe | 0.01 | 0.00 |
| Mn | 0.00 | 0.00 |
| Mg | 0.00 | 0.00 |
| Cr | 0.00 | 0.00 |
| Ni | 0.00 | 0.00 |
| H(H2O) | 0.00 | 0.00 |

Table 2. The EMP analysis results for magnesium silicate cement in the Leka tillite. Values are presented as oxide weight percent. The cement is normalized on 8 oxygens.

| Sample No. | LK14-GC1 | | | | | | | |
|---|---|---|---|---|---|---|---|---|
| Thin section | 1a | | | | | 1b | | |
| Analysis No. | 1 | 4 | 6 | 7 | 51 | 9 | 11 | 12 |
| SiO2 | 23.04 | 7.78 | 8.20 | 8.45 | 14.48 | 44.33 | 40.95 | 45.08 |
| Na2O | 0.14 | 0.00 | 0.03 | 0.00 | 0.03 | 0.04 | 0.02 | 0.01 |
| Al2O3 | 12.89 | 18.47 | 18.68 | 18.42 | 16.42 | 0.02 | 0.03 | 0.01 |
| K2O | 0.01 | 0.00 | 0.00 | 0.00 | 0.28 | 0.05 | 0.01 | 0.06 |
| CaO | 0.73 | 0.10 | 0.11 | 0.04 | 0.14 | 0.13 | 0.14 | 0.06 |
| TiO2 | 0 | 0.00 | 0.01 | 0.00 | 0.01 | 0.01 | 0.00 | 0.00 |
| FeO | 0.73 | 0.14 | 0.15 | 0.36 | 0.17 | 0.07 | 0.04 | 0.07 |
| MnO | 0.05 | 0.00 | 0.04 | 0.02 | 0.06 | 0.00 | 0.00 | 0.00 |
| MgO | 24.59 | 36.78 | 34.42 | 34.24 | 32.52 | 8.94 | 13.51 | 13.04 |
| Cr2O3 | 0.04 | 0.07 | 0.00 | 0.00 | 0.00 | 0.01 | 0.01 | 0.00 |
| NiO | 0.22 | 0.15 | 0.18 | 0.42 | 0.00 | 0.02 | 0.00 | 0.03 |
| Total | 62.44 | 63.46 | 61.78 | 61.88 | 64.12 | 53.63 | 54.67 | 58.32 |
| Si | 0.79 | 0.28 | 0.29 | 0.30 | 0.51 | 1.38 | 1.29 | 1.45 |
| Na | 0.01 | 0.00 | 0.00 | 0.00 | 0.00 | 0.00 | 0.00 | 0.00 |
| Al | 0.52 | 0.77 | 0.77 | 0.76 | 0.68 | 0.00 | 0.00 | 0.00 |
| K | 0.00 | 0.00 | 0.00 | 0.00 | 0.01 | 0.00 | 0.00 | 0.00 |
| Ca | 0.02 | 0.00 | 0.00 | 0.00 | 0.00 | 0.00 | 0.01 | 0.00 |
| Ti | 0.00 | 0.00 | 0.00 | 0.00 | 0.00 | 0.00 | 0.00 | 0.00 |
| $Fe^{2+}$ | 0.02 | 0.00 | 0.00 | 0.01 | 0.00 | 0.00 | 0.00 | 0.00 |
| Mn | 0.00 | 0.00 | 0.00 | 0.00 | 0.00 | 0.00 | 0.00 | 0.00 |
| Mg | 1.27 | 1.96 | 1.81 | 1.80 | 1.72 | 0.42 | 0.64 | 0.63 |
| Cr | 0.00 | 0.00 | 0.00 | 0.00 | 0.00 | 0.00 | 0.00 | 0.00 |
| Ni | 0.01 | 0.00 | 0.00 | 0.01 | 0.00 | 0.00 | 0.00 | 0.00 |
| H(H2O) | 8.61 | 8.64 | 8.91 | 8.90 | 8.44 | 9.63 | 9.54 | 8.93 |

Table 2 continued

| Sample No. | LK14-GC1 | | | | | | | |
|---|---|---|---|---|---|---|---|---|
| Thin section | 1b | | | | | | | |
| Analysis No. | 13 | 14 | 18 | 19 | 21 | 22 | 30 | 33 |
| SiO2 | 43.40 | 42.94 | 38.25 | 41.13 | 26.22 | 27.47 | 11.37 | 17.45 |
| Na2O | 0.00 | 0.01 | 0.01 | 0.00 | 0.75 | 1.96 | 0.05 | 0.00 |
| Al2O3 | 0.03 | 0.04 | 0.31 | 0.20 | 14.75 | 20.04 | 12.59 | 12.23 |
| K2O | 0.04 | 0.02 | 0.05 | 0.02 | 0.13 | 0.02 | 0.09 | 0.02 |
| CaO | 0.11 | 0.17 | 0.11 | 0.15 | 1.37 | 2.82 | 0.00 | 0.04 |
| TiO2 | 0.00 | 0.01 | 0.00 | 0.00 | 0.01 | 0.01 | 0.01 | 0.02 |
| FeO | 0.08 | 0.07 | 0.05 | 0.10 | 0.86 | 0.17 | 0.16 | 0.47 |
| MnO | 0.00 | 0.01 | 0.09 | 0.16 | 0.05 | 0.01 | 0.04 | 0.05 |
| MgO | 9.68 | 20.84 | 21.38 | 34.91 | 31.96 | 30.11 | 35.48 | 39.53 |
| Cr2O3 | 0.00 | 0.00 | 0.00 | 0.01 | 0.00 | 0.02 | 0.00 | 0.06 |
| NiO | 0.02 | 0.00 | 0.02 | 0.01 | 0.03 | 0.03 | 0.08 | 0.09 |
| Total | 53.31 | 64.09 | 60.19 | 76.67 | 76.10 | 82.65 | 59.85 | 69.95 |
| Si | 1.35 | 1.45 | 1.26 | 1.54 | 1.00 | 1.11 | 0.39 | 0.65 |
| Na | 0.00 | 0.00 | 0.00 | 0.00 | 0.06 | 0.15 | 0.00 | 0.00 |
| Al | 0.00 | 0.00 | 0.01 | 0.01 | 0.66 | 0.95 | 0.51 | 0.53 |
| K | 0.00 | 0.00 | 0.00 | 0.00 | 0.01 | 0.00 | 0.00 | 0.00 |
| Ca | 0.00 | 0.01 | 0.00 | 0.01 | 0.06 | 0.12 | 0.00 | 0.00 |
| Ti | 0.00 | 0.00 | 0.00 | 0.00 | 0.00 | 0.00 | 0.00 | 0.00 |
| $Fe^{2+}$ | 0.00 | 0.00 | 0.00 | 0.00 | 0.03 | 0.01 | 0.00 | 0.01 |
| Mn | 0.00 | 0.00 | 0.00 | 0.01 | 0.00 | 0.00 | 0.00 | 0.00 |
| Mg | 0.45 | 1.06 | 1.06 | 1.97 | 1.83 | 1.82 | 1.83 | 2.19 |
| Cr | 0.00 | 0.00 | 0.00 | 0.00 | 0.00 | 0.00 | 0.00 | 0.00 |
| Ni | 0.00 | 0.00 | 0.00 | 0.00 | 0.00 | 0.00 | 0.00 | 0.00 |
| H(H2O) | 9.68 | 8.08 | 8.77 | 5.84 | 6.10 | 4.66 | 9.22 | 7.40 |

Table 2 continued

| Sample No. | LK14-GC1 | | | | | | |
|---|---|---|---|---|---|---|---|
| Thin section | 1b | | | | | | |
| Analysis No. | 37 | 38 | 40 | 42 | 44 | 47 | 48 |
| SiO2 | 42.79 | 13.01 | 35.13 | 41.83 | 33.58 | 48.01 | 45.05 |
| Na2O | 0.00 | 0.35 | 0.00 | 0.03 | 0.01 | 0.00 | 0.00 |
| Al2O3 | 0.75 | 14.04 | 3.61 | 1.70 | 8.34 | 0.10 | 0.31 |
| K2O | 0.00 | 0.02 | 0.03 | 0.44 | 0.02 | 0.02 | 0.00 |
| CaO | 0.06 | 0.23 | 0.07 | 0.15 | 0.08 | 0.45 | 0.39 |
| TiO2 | 0.00 | 0.00 | 0.00 | 0.01 | 0.00 | 0.01 | 0.01 |
| FeO | 0.05 | 0.13 | 0.13 | 0.16 | 0.64 | 0.03 | 0.01 |
| MnO | 0.00 | 0.04 | 0.01 | 0.00 | 0.11 | 0.00 | 0.01 |
| MgO | 35.18 | 43.30 | 36.09 | 35.20 | 37.34 | 31.35 | 32.47 |
| Cr2O3 | 0.00 | 0.01 | 0.00 | 0.03 | 0.05 | 0.00 | 0.02 |
| NiO | 0.01 | 0.17 | 0.09 | 0.00 | 0.03 | 0.01 | 0.00 |
| Total | 78.75 | 71.31 | 75.03 | 79.52 | 80.20 | 79.97 | 78.25 |
| Si | 1.63 | 0.49 | 1.31 | 1.61 | 1.31 | 1.82 | 1.70 |
| Na | 0.00 | 0.03 | 0.00 | 0.00 | 0.00 | 0.00 | 0.00 |
| Al | 0.03 | 0.62 | 0.16 | 0.08 | 0.38 | 0.00 | 0.01 |
| K | 0.00 | 0.00 | 0.00 | 0.02 | 0.00 | 0.00 | 0.00 |
| Ca | 0.00 | 0.01 | 0.00 | 0.01 | 0.00 | 0.02 | 0.02 |
| Ti | 0.00 | 0.00 | 0.00 | 0.00 | 0.00 | 0.00 | 0.00 |
| $Fe^{2+}$ | 0.00 | 0.00 | 0.00 | 0.01 | 0.02 | 0.00 | 0.00 |
| Mn | 0.00 | 0.00 | 0.00 | 0.00 | 0.01 | 0.00 | 0.00 |
| Mg | 2.01 | 2.45 | 2.02 | 2.03 | 2.19 | 1.79 | 1.84 |
| Cr | 0.00 | 0.00 | 0.00 | 0.00 | 0.00 | 0.00 | 0.00 |
| Ni | 0.00 | 0.01 | 0.00 | 0.00 | 0.00 | 0.00 | 0.00 |
| H(H2O) | 5.38 | 7.21 | 6.03 | 5.24 | 5.16 | 5.08 | 5.46 |

Table 3 The EMP analysis results for carbonate minerals and quartz in the Leka tillite. Values are presented as oxide weight percent. The carbonate is normalized on 3 oxygens and the quartz is normalized on 2 oxygens.

| Sample No. | LK14-GC-1 | | | | | |
|---|---|---|---|---|---|---|
| Thinsection No. | 1b | | | | | |
| Dominant Mineral | Calcite | Magnesite | Calcite | Calcite | Calcite | Quartz |
| Analysis No. | 15 | 16 | 17 | 26 | 41 | 36 |
| SiO2 | 0.05 | 0.00 | 0.18 | 0.03 | 0.03 | 100.57 |
| Na2O | 0.00 | 0.00 | 0.00 | 0.04 | 0.04 | 0.00 |
| Al2O3 | 0.00 | 0.00 | 0.00 | 0.00 | 0.02 | 0.01 |
| K2O | 0.00 | 0.00 | 0.00 | 0.02 | 0.02 | 0.02 |
| CaO | 55.17 | 0.15 | 55.03 | 55.91 | 55.52 | 0.00 |
| TiO2 | 0.00 | 0.00 | 0.00 | 0.02 | 0.00 | 0.00 |
| FeO | 0.06 | 1.89 | 0.08 | 0.11 | 0.10 | 0.06 |
| MnO | 0.14 | 0.24 | 0.45 | 0.00 | 0.06 | 0.00 |
| MgO | 0.29 | 47.53 | 0.86 | 0.41 | 0.31 | 0.01 |
| Cr2O3 | 0.00 | 0.00 | 0.00 | 0.02 | 0.00 | 0.00 |
| NiO | 0.00 | 0.00 | 0.00 | 0.00 | 0.07 | 0.06 |
| Total | 55.70 | 49.80 | 56.60 | 56.54 | 56.15 | 100.59 |
| Si | 0.00 | 0.00 | 0.00 | 0.00 | 0.00 | 1.00 |
| Na | 0.00 | 0.00 | 0.00 | 0.00 | 0.00 | 0.00 |
| Al | 0.00 | 0.00 | 0.00 | 0.00 | 0.00 | 0.00 |
| K | 0.00 | 0.00 | 0.00 | 0.00 | 0.00 | 0.00 |
| Ca | 0.98 | 0.00 | 0.99 | 1.00 | 0.99 | 0.00 |
| Ti | 0.00 | 0.00 | 0.00 | 0.00 | 0.00 | 0.00 |
| $Fe^{2+}$ | 0.00 | 0.02 | 0.00 | 0.00 | 0.00 | 0.00 |
| Mn | 0.00 | 0.00 | 0.01 | 0.00 | 0.00 | 0.00 |
| Mg | 0.01 | 1.02 | 0.02 | 0.01 | 0.01 | 0.00 |
| Cr | 0.00 | 0.00 | 0.00 | 0.00 | 0.00 | 0.00 |
| Ni | 0.00 | 0.00 | 0.00 | 0.00 | 0.00 | 0.00 |
| $C(CO_3^{2-})$ | 1.00 | 0.98 | 0.99 | 0.99 | 1.00 | |

Table 4 The EMP analysis results for the magnesium silicate cement in the Feragen tillite. Values are present as oxide weight percent. The magnesium silicate cement is normalized on 8 oxygens

| Sample No. | Fer9-12 | | Fer8-12 | | | | | |
|---|---|---|---|---|---|---|---|---|
| Analysis No. | F1 | F2 | F3 | F4 | F5 | F6 | F7 | F8 |
| SiO2 | 54.75 | 57.66 | 42.96 | 42.09 | 42.30 | 42.58 | 37.24 | 43.39 |
| Na2O | 0.20 | 0.00 | 0.00 | 0.01 | 0.00 | 0.00 | 0.02 | 0.06 |
| Al2O3 | 3.16 | 0.75 | 0.18 | 0.15 | 0.77 | 0.36 | 0.03 | 1.27 |
| K2O | 0.72 | 0.03 | 0.03 | 0.04 | 0.13 | 0.02 | 0.01 | 0.29 |
| CaO | 0.28 | 0.06 | 0.07 | 0.07 | 0.02 | 0.01 | 0.05 | 0.06 |
| TiO2 | 0.05 | 0.01 | 0.00 | 0.00 | 0.01 | 0.01 | 0.00 | 0.01 |
| FeO | 0.43 | 0.12 | 0.15 | 0.07 | 0.10 | 0.13 | 0.16 | 0.60 |
| MnO | 0.00 | 0.00 | 0.05 | 0.01 | 0.02 | 0.02 | 0.00 | 0.00 |
| MgO | 27.38 | 26.76 | 38.95 | 37.45 | 37.98 | 38.81 | 35.59 | 37.75 |
| Cr2O3 | 0.00 | 0.00 | 0.00 | 0.00 | 0.00 | 0.04 | 0.00 | 0.02 |
| NiO | 0.01 | 0.01 | 0.07 | 0.05 | 0.00 | 0.06 | 0.02 | 0.03 |
| Total | 86.97 | 85.36 | 82.41 | 79.89 | 81.31 | 82.03 | 73.03 | 83.47 |
| Si | 2.18 | 2.24 | 1.69 | 1.62 | 1.65 | 2.12 | 1.37 | 1.70 |
| Na | 0.00 | 0.00 | 0.00 | 0.00 | 0.00 | 0.00 | 0.00 | 0.00 |
| Al | 0.15 | 0.03 | 0.01 | 0.00 | 0.04 | 0.02 | 0.00 | 0.06 |
| K | 0.04 | 0.00 | 0.00 | 0.00 | 0.00 | 0.00 | 0.00 | 0.01 |
| Ca | 0.01 | 0.00 | 0.00 | 0.00 | 0.00 | 0.00 | 0.00 | 0.00 |
| Ti | 0.00 | 0.00 | 0.00 | 0.00 | 0.00 | 0.00 | 0.00 | 0.00 |
| $Fe^{2+}$ | 0.01 | 0.01 | 0.01 | 0.00 | 0.00 | 0.01 | 0.00 | 0.02 |
| Mn | 0.00 | 0.00 | 0.00 | 0.00 | 0.00 | 0.00 | 0.00 | 0.00 |
| Mg | 1.64 | 1.56 | 2.30 | 2.16 | 2.22 | 2.89 | 1.96 | 2.27 |
| Cr | 0.00 | 0.00 | 0.00 | 0.00 | 0.00 | 0.00 | 0.00 | 0.00 |
| Ni | 0.00 | 0.00 | 0.00 | 0.00 | 0.00 | 0.00 | 0.00 | 0.00 |
| H(H2O) | 3.46 | 3.80 | 4.60 | 5.16 | 4.86 | 5.96 | 6.60 | 4.42 |

Table 4 Continued

| Sample No. | Fer8-12 | | | Fer7-12 | | | | |
|---|---|---|---|---|---|---|---|---|
| Analysis No. | F9 | F10 | F11 | F12 | F13 | F14 | | |
| SiO2 | 45.49 | 44.55 | 43.23 | 48.07 | 49.61 | 47.67 | | |
| Na2O | 0.02 | 0.07 | 0.01 | 0.01 | 0.06 | 0.08 | | |
| Al2O3 | 0.01 | 0.13 | 0.00 | 0.39 | 1.55 | 0.06 | | |
| K2O | 0.02 | 0.08 | 0.01 | 0.09 | 0.40 | 0.02 | | |
| CaO | 0.10 | 0.06 | 0.05 | 0.23 | 0.11 | 0.41 | | |
| TiO2 | 0.00 | 0.00 | 0.00 | 0.00 | 0.00 | 0.01 | | |
| FeO | 0.06 | 0.16 | 0.05 | 0.29 | 0.38 | 0.88 | | |
| MnO | 0.00 | 0.01 | 0.03 | 0.09 | 0.09 | 0.07 | | |
| MgO | 38.37 | 36.63 | 39.77 | 32.19 | 32.12 | 35.11 | | |
| Cr2O3 | 0.00 | 0.00 | 0.00 | 0.05 | 0.00 | 0.02 | | |
| NiO | 0.00 | 0.00 | 0.03 | 0.08 | 0.00 | 0.05 | | |
| Total | 84.05 | 81.63 | 83.17 | 81.48 | 84.25 | 84.37 | | |
| Si | 1.80 | 1.73 | 1.71 | 1.85 | 1.95 | 1.89 | | |
| Na | 0.00 | 0.00 | 0.00 | 0.00 | 0.00 | 0.00 | | |
| Al | 0.00 | 0.00 | 0.00 | 0.02 | 0.07 | 0.00 | | |
| K | 0.00 | 0.00 | 0.00 | 0.00 | 0.02 | 0.00 | | |
| Ca | 0.01 | 0.00 | 0.00 | 0.01 | 0.01 | 0.02 | | |
| Ti | 0.00 | 0.00 | 0.00 | 0.00 | 0.00 | 0.00 | | |
| $Fe^{2+}$ | 0.00 | 0.01 | 0.00 | 0.01 | 0.01 | 0.03 | | |
| Mn | 0.00 | 0.00 | 0.00 | 0.00 | 0.00 | 0.00 | | |
| Mg | 2.28 | 2.14 | 2.36 | 1.86 | 1.90 | 2.09 | | |
| Cr | 0.00 | 0.00 | 0.00 | 0.00 | 0.00 | 0.00 | | |
| Ni | 0.00 | 0.00 | 0.00 | 0.00 | 0.00 | 0.00 | | |
| H(H2O) | 4.22 | 4.76 | 4.44 | 4.76 | 4.14 | 4.14 | | |

Table 5 The EMP analysis results for some minerals found in the Feragen tillite. Values are present in oxide weight percent. Brucite is normalized on 1 cation totally, quartz normalized on 1 cation, serpentine and K-feldspar normalized on 5 cations and olivine normalized on 3 cations. All analysis data about the mentioned minerals are from the previous report (Li et al., 2013)

| Mineral | Fresh Brucite | | Weathered Brucite | | | | | Quartz |
|---|---|---|---|---|---|---|---|---|
| Formula | $Mg(OH)_2$ | | $(Mg,Fe)(OH)_2$ | | | | | SiO2 |
| SiO2 | 0.30 | 0.09 | 0.87 | 0.78 | 6.50 | 4.93 | 5.37 | 100.34 |
| TiO2 | 0.00 | 0.00 | 0.01 | 0.03 | 0.00 | 0.00 | 0.00 | 0.01 |
| Al2O3 | 0.01 | 0.01 | 0.00 | 0.02 | 0.02 | 0.00 | 0.00 | 0.00 |
| FeO | 10.81 | 9.71 | 16.77 | 16.39 | 18.30 | 17.22 | 17.13 | 0.05 |
| MnO | 0.34 | 0.42 | 0.49 | 0.54 | 1.03 | 1.48 | 1.19 | 0.02 |
| MgO | 67.92 | 68.09 | 34.97 | 31.75 | 42.77 | 39.27 | 36.09 | 0.22 |
| CaO | 0.02 | 0.00 | 0.00 | 0.04 | 0.05 | 0.09 | 0.04 | 0.00 |
| Na2O | 0.01 | 0.00 | 0.01 | 0.00 | 0.01 | 0.04 | 0.03 | 0.01 |
| K2O | 0.01 | 0.00 | 0.00 | 0.00 | 0.01 | 0.01 | 0.00 | 0.01 |
| Cr2O3 | 0.04 | 0.01 | 0.00 | 0.01 | 0.00 | 0.00 | 0.00 | 0.00 |
| NiO | 0.09 | 0.24 | 3.66 | 3.88 | 0.95 | 0.96 | 1.37 | 0.00 |
| Total | 79.51 | 78.48 | 56.72 | 53.43 | 69.60 | 63.93 | 61.22 | 100.56 |
| Si | 0.00 | 0.00 | 0.01 | 0.01 | 0.07 | 0.06 | 0.07 | 1.00 |
| Ti | 0.00 | 0.00 | 0.00 | 0.00 | 0.00 | 0.00 | 0.00 | 0.00 |
| Al | 0.00 | 0.00 | 0.00 | 0.00 | 0.00 | 0.00 | 0.00 | 0.00 |
| $Fe^{2+}$ | 0.08 | 0.07 | 0.20 | 0.21 | 0.18 | 0.18 | 0.19 | 0.00 |
| Mn | 0.00 | 0.00 | 0.01 | 0.01 | 0.01 | 0.02 | 0.01 | 0.00 |
| Mg | 0.91 | 0.92 | 0.74 | 0.72 | 0.73 | 0.73 | 0.71 | 0.00 |
| $Ca^{+}$ | 0.00 | 0.00 | 0.00 | 0.00 | 0.00 | 0.00 | 0.00 | 0.00 |
| Na | 0.00 | 0.00 | 0.00 | 0.00 | 0.00 | 0.00 | 0.00 | 0.00 |
| K | 0.00 | 0.00 | 0.00 | 0.00 | 0.00 | 0.00 | 0.00 | 0.00 |
| Cr | 0.00 | 0.00 | 0.00 | 0.00 | 0.00 | 0.00 | 0.00 | 0.00 |
| Ni | 0.00 | 0.00 | 0.04 | 0.05 | 0.01 | 0.01 | 0.02 | 0.00 |
| Total cation | 1 | 1 | 1 | 1 | 1 | 1 | 1 | 1 |

Table 5 Continued. (Li et al., 2013)

| Mineral | Quartz | K-feldspar | Serpentine | | | Olivine | | |
|---|---|---|---|---|---|---|---|---|
| Formula | $SiO_2$ | $KAlSi_3O_8$ | $(Mg, Fe)_3Si_2O_5(OH)_4$ | | | $(Mg,Fe)_2SiO_8$ | | |
| SiO2 | 87.51 | 64.45 | 42.46 | 51.25 | 43.04 | 41.14 | 40.87 | 36.64 |
| TiO2 | 0.04 | 0.00 | 0.02 | 0.00 | 0.00 | 0.02 | 0.00 | 0.00 |
| Al2O3 | 0.06 | 17.94 | 0.01 | 0.77 | 0.00 | 0.01 | 0.00 | 0.02 |
| FeO | 0.03 | 0.02 | 1.84 | 0.11 | 1.79 | 6.78 | 7.18 | 4.50 |
| MnO | 0.00 | 0.00 | 0.05 | 0.02 | 0.06 | 0.09 | 0.13 | 0.10 |
| MgO | 1.87 | 1.07 | 39.38 | 21.09 | 41.50 | 51.85 | 51.73 | 40.00 |
| CaO | 0.02 | 0.00 | 0.02 | 0.03 | 0.07 | 0.05 | 0.00 | 0.04 |
| Na2O | 0.00 | 0.41 | 0.00 | 0.13 | 0.02 | 0.00 | 0.00 | 0.01 |
| K2O | 0.00 | 15.47 | 0.00 | 0.03 | 0.01 | 0.01 | 0.01 | 0.01 |
| Cr2O3 | 0.00 | 0.00 | 0.07 | 0.01 | 0.03 | 0.00 | 0.04 | 0.00 |
| NiO | 0.00 | 0.00 | 0.07 | 0.05 | 0.32 | 0.41 | 0.40 | 0.42 |
| Total | 89.53 | 99.20 | 83.92 | 73.49 | 86.82 | 100.32 | 100.33 | 81.69 |
| Si | 0.97 | 3.00 | 2.06 | 3.05 | 2.01 | 0.99 | 0.99 | 1.09 |
| Ti | 0.00 | 0.00 | 0.00 | 0.00 | 0.00 | 0.00 | 0.00 | 0.00 |
| Al | 0.00 | 0.98 | 0.00 | 0.05 | 0.00 | 0.00 | 0.00 | 0.00 |
| $Fe^{2+}$ | 0.00 | 0.00 | 0.08 | 0.01 | 0.07 | 0.14 | 0.15 | 0.11 |
| Mn | 0.00 | 0.00 | 0.00 | 0.00 | 0.00 | 0.00 | 0.00 | 0.00 |
| Mg | 0.03 | 0.07 | 2.85 | 1.87 | 2.90 | 1.86 | 1.86 | 1.78 |
| $Ca^{+}$ | 0.00 | 0.00 | 0.00 | 0.00 | 0.00 | 0.00 | 0.00 | 0.00 |
| Na | 0.00 | 0.04 | 0.00 | 0.02 | 0.00 | 0.00 | 0.00 | 0.00 |
| K | 0.00 | 0.92 | 0.00 | 0.00 | 0.00 | 0.00 | 0.00 | 0.00 |
| Cr | 0.00 | 0.00 | 0.00 | 0.00 | 0.00 | 0.00 | 0.00 | 0.00 |
| Ni | 0.00 | 0.00 | 0.00 | 0.00 | 0.01 | 0.01 | 0.01 | 0.01 |
| Total cation | 1 | 5 | 5 | 5 | 5 | 3 | 3 | 3 |

# B The collection for the WDS analysis positions in the thin-sections for the Leka tillite

The analysis number is marked with blue round on the corresponding position.

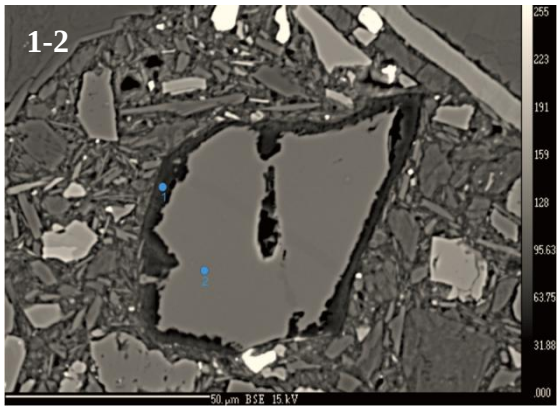


(I)

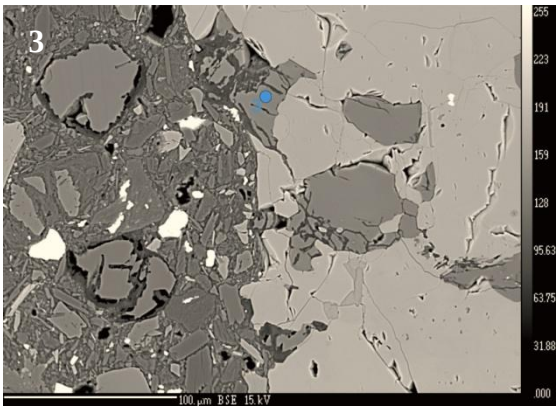


(II)

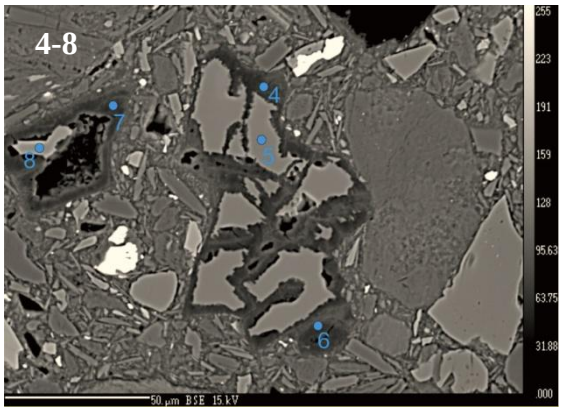


(III)

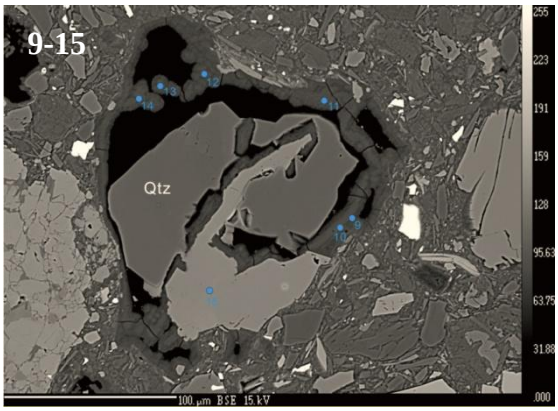


(IV)

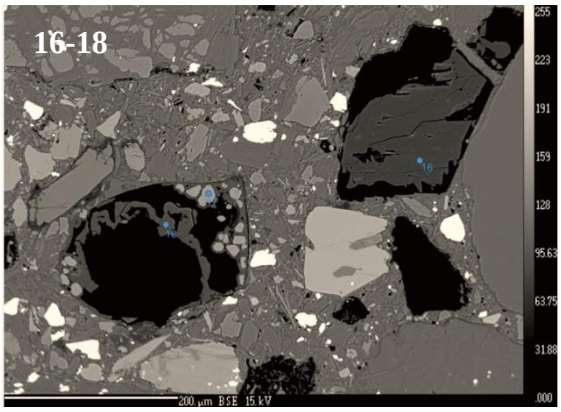


(V)

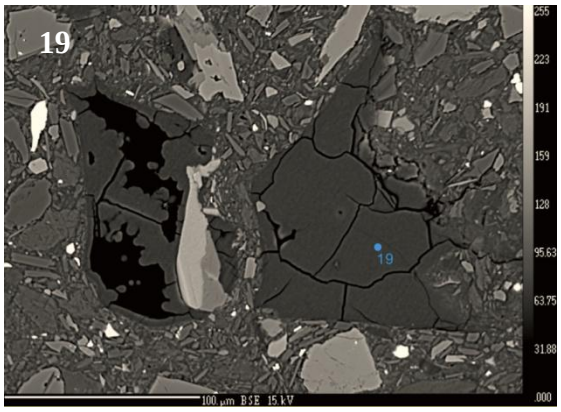


(VI)

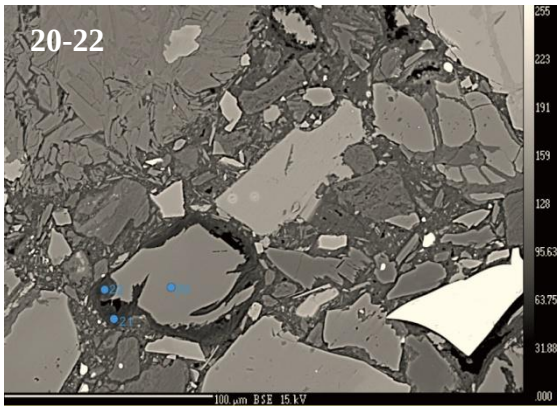


(VII)

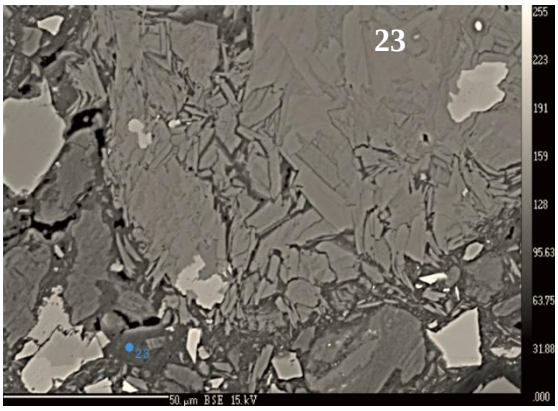


(VIII)

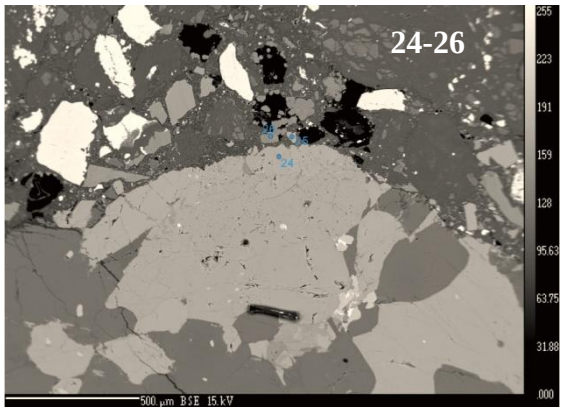


(IX)

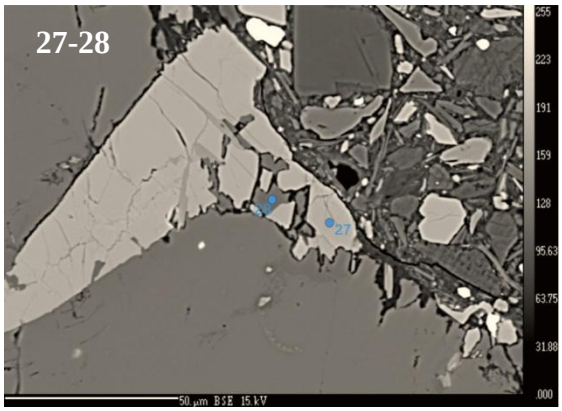


(X)

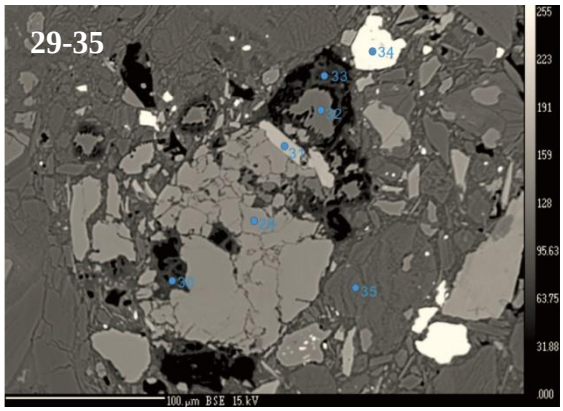


(XI)

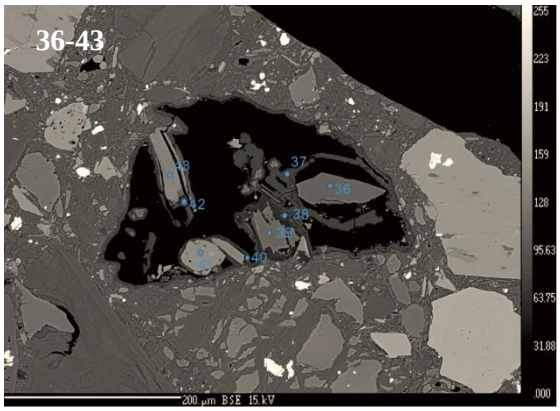


(XII)

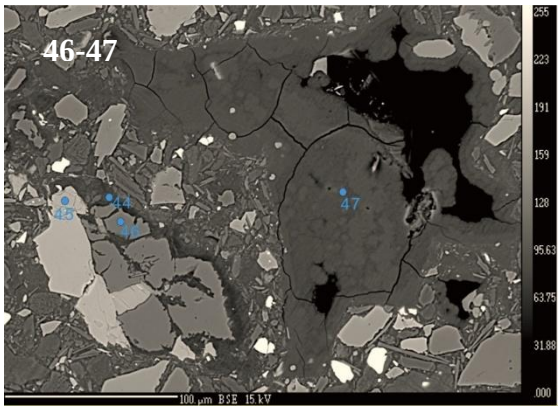


(XIII)

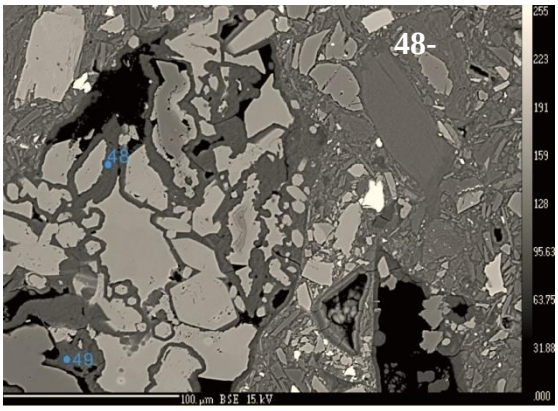


(XIV)

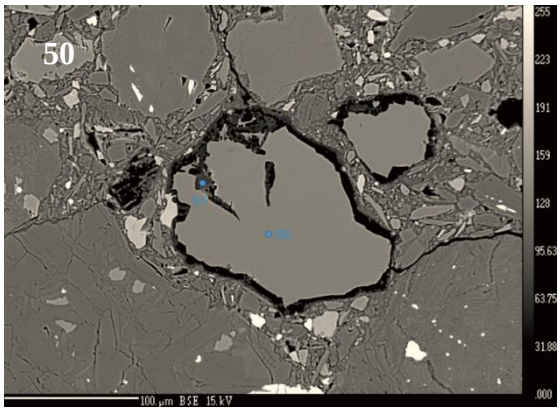


(XV)

# C Simulation code in Phreeqc

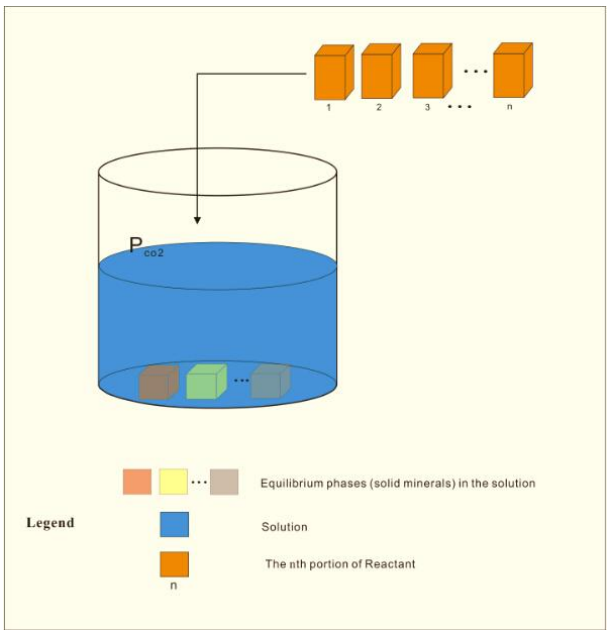


**Fig C. 1 The demonstrating diagram for the PHREEQC simulation**

General description for the amount of brucite in the simulation(Li et al., 2013).

The porosity of rock is assumed as 30%, thus the total volume in the simulation is 3.33L as the solution volume is 1L. So the volume of rock is 2.33L

And volume content for brucite in the rock is assumed as 20%, so the

$$V_{brucite} = 2.33 \times 20\% \approx 0.47L$$

And brucite density is 2.44kg/L and its mole mass is 58.3 g/mol

So the amount of brucite in the simulation=$0.47 \times 2.44 \times \frac{1000}{58.3}$mol=19.53 mol

The schematic diagram for the PHREEQC simulation is displayed in Fig C.1

## 1. Simulation a

```
PHASES
Pyroaurite
    Mg6Fe2(CO3)(OH)16(H2O)4 + 16H+ = CO3-2 + 2Fe+3 + 20H2O + 6Mg+2
    log_k     41.5

SOLUTION 1
    temp      0.1
    pH        7 charge
    pe        4
    redox     pe
    units     mol/kgw
    density   1
    -water    1 # kg

INCREMENTAL_REACTIONS True
REACTION 1
    Antigorite 0.01
    Forsterite 0.0093
    Fayalite   0.0007
    Mg         0.9
    Fe         0.1
    OH         2
    19.53 moles in 20 steps

EQUILIBRIUM_PHASES 1
    Albite_high 0 10
    CO2(g)    -3.4 10
    Hydromagnesite 0 0
    K-feldspar 0 10
    Nesquehonite 0 0
    Pyroaurite 0 0
    Quartz    0 10
    Talc      0 0
    artinite  0 0
    lansfordite 0 0
    Magnesite 0 0
```

## 2. Simulation b

```
PHASES
Pyroaurite
    Mg6Fe2(CO3)(OH)16(H2O)4 + 16H+ = CO3-2 + 2Fe+3 + 20H2O + 6Mg+2
    log_k     41.5

SOLUTION 1
    temp      0.1
    pH        7 charge
    pe        4
    redox     pe
    units     mol/kgw
    density   1
    -water    1 # kg

INCREMENTAL_REACTIONS True
REACTION 1
    Antigorite 0.01
    Forsterite 0.0093
    Fayalite   0.0007
    Mg         0.5
    Fe         0.5
    OH         2
    19.53 moles in 20 steps

EQUILIBRIUM_PHASES 1
    Albite_high 0 10
    CO2(g)    -3.4 10
    Hydromagnesite 0 0
    K-feldspar 0 10
    Nesquehonite 0 0
    Pyroaurite 0 0
    Quartz    0 10
    Talc      0 0
    artinite  0 0
    lansfordite 0 0
    Magnesite 0 0
```

## 3. Simulation c

```
PHASES
Pyroaurite
    Mg6Fe2(CO3)(OH)16(H2O)4 + 16H+ = CO3-2 + 2Fe+3 + 20H2O + 6Mg+2
    log_k     41.5

SOLUTION 1
    temp      273
    pH        7 charge
    pe        4
    redox     pe
    units     mol/kgw
    density   1
    -water    1 # kg

INCREMENTAL_REACTIONS True
REACTION 1
```

```
    Antigorite 0.01
    Forsterite 0.0093
    Fayalite   0.0007
    Mg         0.5
    Fe         0.5
    OH         2
    19.53 moles in 20 steps

EQUILIBRIUM_PHASES 1
    Albite_high 0 10
    CO2(g)    -3.4 10
    Hydromagnesite 0 0
    K-feldspar 0 10
    Nesquehonite 0 0
    Pyroaurite 0 0
    Quartz    0 10
    Talc      0 0
    artinite  0 0
    lansfordite 0 0
    Magnesite 0 0
```

## 4. Simulation d

```
PHASES
Pyroaurite
    Mg6Fe2(CO3)(OH)16(H2O)4 + 16H+ = CO3-2 + 2Fe+3 + 20H2O + 6Mg+2
    log_k     41.5

SOLUTION 1
    temp      273
    pH        7 charge
    pe        4
    redox     pe
    units     mol/kgw
    density   1
    -water    1 # kg

INCREMENTAL_REACTIONS True
REACTION 1
    Antigorite 0.01
    Forsterite 0.0093
    Fayalite   0.0007
    Mg         0.5
    Fe         0.5
    OH         2
    19.53 moles in 20 steps

EQUILIBRIUM_PHASES 1
    Albite_high 0 10
    CO2(g)    -5 10
    Hydromagnesite 0 0
    K-feldspar 0 10
    Nesquehonite 0 0
    Pyroaurite 0 0
    Quartz    0 10
    Talc      0 0
    artinite  0 0
    lansfordite 0 0
    Magnesite 0 0
```

## 5. Simulation e

```
PHASES
Pyroaurite
    Mg6Fe2(CO3)(OH)16(H2O)4 + 16H+ = CO3-2 + 2Fe+3 + 20H2O + 6Mg+2
    log_k     41.5

SOLUTION 1
    temp      0.1
    pH        7 charge
    pe        4
    redox     pe
    units     mol/kgw
    density   1
    -water    1 # kg

INCREMENTAL_REACTIONS True
REACTION 1
    Antigorite 0.01
    Forsterite 0.0093
    Fayalite   0.0007
    Mg         0.9
    Fe         0.1
    OH         2
    19.53 moles in 20 steps

EQUILIBRIUM_PHASES 1
    Albite_high 0 10
    Anorthite 0 10
    CO2(g)    -3.4 10
    Hydromagnesite 0 0
    K-feldspar 0 10
    Nesquehonite 0 0
    Pyroaurite 0 0
    Quartz    0 10
    Talc      0 0
    artinite  0 0
    dolomite  0 0
    lansfordite 0 0
    Magnesite 0 0
```

## 6. Simulation for the quartz experiment(pH=13 and T=20℃)

```
RATES
    quartz
-start
10 logK=PARM(1)
30 rate=10^((LOG10(1.35*M)+PARM(1)-0.5*LA("H+")+LOG10(1-SR("Quartz"))))
40 moles=rate*TIME
60 M_DISSOLVED=moles*60
80 save moles
-end

KINETICS 1
quartz
    -formula  SiO2  1
    -m        1
    -m0       1
```

```
    -parms    -16.29
    -tol      1e-08
-steps       2592000 in 30 steps # seconds
-step_divide 1
-runge_kutta 3
-bad_step_max 500

INCREMENTAL_REACTIONS True

SOLUTION 1
    temp      20
    pH        13
    pe        4
    redox     pe
    units     mol/kgw
    density   1
    Cl(-1)    1 charge
    Na        2
    -water    1 # kg
```

# D Image processing procedure in matlab

1. **I=imread('BSE image storage path');**
   % read in original BSE image and named as **I**.

2. **I_bw=im2bw(I);**
   % Convert I to binary image **I_bw** because of original image is a grey-scale image

3. **I_bw_labelled=bwlabel(I_bw);**
   % labeled all connected objectives in binary image **I_bw**

4. **R=(I_bw_labelled=the number of the interested part)**
   % Find out the interested part in image( weathered mineral grain)

5. **Figure(1)=imagesc(I) [x y]=getpts(1)**%Display original images I in figure(1) in matlab and pick out the coordinates of the two end points on scale bar in I using function 'getpts' and store the coordinates in the array **[x y]**. 'figure()' here is a function in matlab not figure in the thesis.

6. **Scale_length=sqrt{[x(1)-x(2)]$^2$+[y(1)-y(2)]$^2$}** % Calculate out the scale length in pixel.

7. **Pixel_length=(actual scale bar length)/(Scale_length);**
   % Calculate out each pixel's actual length (um) and store it in the variable **Pixel_length**.

8. **A_1=bwarea(R);** % Calculate out the area for the interested part in pixel number.

9. **A=[sqrt(A_1)*Pixel_length]$^2$;** %Convert the area in pixel number to area A in um$^2$